GRAPHENE AND SEMICONDUCTOR OR METALLIC NANOPARTICLES FOR ENERGY CONVERSION

Presentata da: Raffaello Mazzaro

                                                              Relatore
Coordinatore Dottorato   Prof.ssa Paola Ceroni
Prof. Aldo Roda   Co-relatore
                                                      Dott. Vittorio Morandi

Thesis advisor: Professor Paola Ceroni
Thesis co-advisor: Dr. Vittorio Morandi

Raffaello Mazzaro

Graphene and semiconductor or metallic nanoparticles for energy conversion

Abstract

The purpose of the present PhD thesis is to investigate the properties of innovative nanomaterials with respect to the conversion of renewable energies to electrical and chemical energy. The materials have been synthesized and characterized by means of a wide spectrum of morphological, compositional and photophysical techniques, in order to get an insight into the correlation between the properties of each material and the activity towards different energy conversion applications. The activity comes within a worthwhile collaboration between the photochemistry lab of the "G.Ciamician" department of the university of Bologna and the CNR-IMM Bologna.

Two main topics are addressed: in the first part of the thesis the light harvesting in pyrene functionalized silicon nanocrystals has been discussed, suggesting an original approach to successfully increase the absorption properties of these nanocrystals. The interaction of these nanocrystals was then studied, in order to give a deeper insight on the charge and energy extraction, preparing the way to implement SiNCs as active material in optoelectronic devices and photovoltaic cells. In addition to this, the luminescence of SiNCs has been exploited to increase the efficiency of conventional photovoltaic cells by means of two innovative architectures. Specifically, SiNCs has been used as luminescent downshifting layer in dye sensitized solar cells, and they were shown to be very promising light emitters in luminescent solar concentrators.

The second part of the thesis was concerned on the production of hydrogen by platinum nanoparticles coupled to either electro-active or photo-active materials. Within this context, the electrocatalytic activity of platinum nanoparticles supported on exfoliated graphene has been studied, preparing an high-efficiency catalyst and disclosing the role of the exfoliation technique towards the catalytic activity. Furthermore, platinum nanoparticles have been synthesized within photoactive dendrimers, providing the first proof of concept of a dendrimer-based photocatalytic system for the hydrogen production where both sensitizer and catalyst are anchored to a single scaffold.

Contents

To the people finding me when I get lost.

Acknowledgments

I WANT TO THANK first of all Paola and Vittorio for giving me the opportunity to experience the fascinating world of research and for supporting me along this path with their knowledge and kindness.

I want to thank all the people that shared with me some of the best and the worst moments in the lab activity; from the Ciamician guys, the new and the old ones, to the CNR ones: it's mainly because of you if didn't get crazy during the long days in the lab.

I want to thank the guys in Montréal that didn't give me the time to feel homesick during my short stay in the wonderful Québec.

Then I want to thank my parents for giving me more than I deserve every day of my life, my little (no more) sister for being always my little funny sister, my friends for walking beside me since longer before the PhD, and the brave girl with whom I hope to build my future, brick by brick.

Finally I want to thank the lab for teaching me how not to give up despite his regular sabotage attempts.

0
Introduction

Since the industrial revolution, the search for efficient and widely available energy sources has driven most of the mankind activities, leading to a dramatic change in our society's energy use. Up to the oil crisis of the late 70^s, the development of new technology was essentially aimed to the increasing of the society wellness, considering the energy sources as virtually unlimited. The last 40 years have turned this concept over thanks to the increasing awareness about how limited and fragile Earth is. Therefore, in order to (at least) hold the actual standard of living, part of the industrial and scientific world has turned its attention to the exploitation of renewable energy sources, that are now providing more than 19% of the global energy consumption[1] and are expected to more than double before 2035.[2]

Among the renewable energy sources, sunlight is the most easily available and widespread. The quantity of energy that continuously arrives from the Sun on a clear day, around 1kW m^{-2}, is far exceeding all human needs in one year. Compared to the conventional energy sources based on fossil fuels, the conversion of the renewable ones to a suitable shape, such as electricity or heat, is not trivial. For this reason, a wide activity is taking place in the research

of new approaches to increase the efficiency in the conversion of the energy provided by wind or sunlight. The solar energy conversion is typically carried out in two steps: the collection of solar light by a molecule or a material inducing the formation of a highly energetic excited state, and the extraction of this energy as electrical power, light emission in a desired spectrum interval, or as an electrochemically induced reaction.

In this framework, this PhD thesis has been devoted to the investigation of the properties of innovative nano-materials in the energy conversion. The research project was carried out through a collaboration between the Chemistry Department "G.Ciamician" of the University of Bologna, where the synthesis and optical characterization of the nano-materials was performed, and the electron microscopy group in the CNR-IMM in Bologna.

The thesis is mainly divided in two parts focusing on different aspects of the energy conversion performed by nano-materials.

The subject of the first part of the thesis will be the conversion of solar energy to electrical energy by means of a particular class of nanocrystals.

In the first chapter we deal with the first step of the solar energy conversion; indeed the investigation of the light harvesting of UV-Visible light in semiconductor quantum dots functionalized with photoactive ligands is reported. In particular, the synthesis of luminescent silicon nanocrystals (SiNCs) functionalized with different pyrene ligands is illustrated and the photophysical processes between the ligands and the silicon core is investigated.

In the second chapter we discuss the extraction of the energy accumulated in silicon nanocrystals by means of different photophysical processes. In the first section, a deep investigation of the intermolecular interaction of SiNCs with carbon allotropes is reported, studying the occurrence of energy and electron transfer processes both by spectroscopic and microscopy experiments. In addition to this, this chapter illustrates the work I carried out in Prof. Rosei's laboratory (INRS-EMT, Varennes, QC, Canada), where I spent several months as a visiting student investigating the feasibility of SiNCs as luminescent specie in un-conventional photovoltaics.

The second part of the thesis is focused on the conversion of energy directly or indirectly provided by sunlight into chemical energy, by storing it into highly energetic compounds that can be freely used as combustible, as commonly happens with carbon fuels.

The third chapter we describes the preparation of an highly efficient electro-catalyst for the production of hydrogen based on exfoliated graphene and platinum nanoparticles. The performance of the hybrid material is optimized by exploring different exfoliation techniques to produce graphene dispersions and the electrochemical activity is carefully evaluated in water environment.

Finally, in the last chapter of the thesis, we illustrate the design a photocatalytic system for the production of hydrogen based on platinum nanoparticles embedded in photoactive dendrimers. The synthesis of the nanoparticles is followed through an accurate observation of the system photophysics and morphology, and the efficiency of the catalytic system is tested with respect to the hydrogen evolution reaction.

*Science cannot solve the ultimate mystery of nature. And that
is because, in the last analysis, we ourselves are part of nature
and therefore part of the mystery that we are trying to solve.*

Max Karl Ernst Ludwig Planck

1

Silicon nanocrystals functionalized with photoactive molecules

THIS CHAPTER is devoted to the investigation of a light harvesting system based on Silicon nanocrystals co-functionalized with Pyrene derivatives. We report the synthesis of these particular nanocrystals and the complete morphological, structural and optical characterization. We also report the effect of the distance between the chromophore (pyrene) and the Si nanocrystal core on the energy transfer efficiency, in order to get a full insight of the light harvesting mechanism.

1.1 Silicon nanocrystals: from the beginning

SILICON is the 14th element of the periodic table, but the very 1st one that comes to our mind when talking about the semiconductor industry. Thanks to the wide availability (only oxygen

is more abundant on earth) and the peculiar electronic properties, silicon has become ubiq-
uitous in many applications from microelectronics, to solar cells and optoelectronics. The
reasons for the popularity of silicon are mainly due to the electronic structure that leads to the
peculiar optical and electrical properties.

Consistent to all the other semiconductors, silicon is also subject to a strong variation of
these properties with size as long as the material dimension is reduced to the nano-scale. First,
surface is playing a key role in such small structures due to the very high surface/volume ratio,
which can affect both physical and chemical properties. This effect is important both in metals,
as we will see in Chapter 3 and 4, and in semiconductors, where the presence of surface trap
states induce the need to embed clusters in a passivating medium.[3]

The second size-dependent effect is mostly related to the core size and it is called quantum
confinement effect, which typical size treshold is relatively large for semiconductors, compared
to metals, insulators, or molecular crystals. This can be explained by considering the schematic
diagram of energy-density of states (DOS) shown in Figure 1.1.[4] Usually, for any material, the
states (or bands when having a continuum of states) are centered about atomic energy levels
and the width of the states distribution is affected by the nearest-neighbour interactions. If
these interactions are small, as in the case of insulators or Van der Walls crystals, the bands
in the solids are narrow and the size variation is not appreciable even at very tiny size. In the
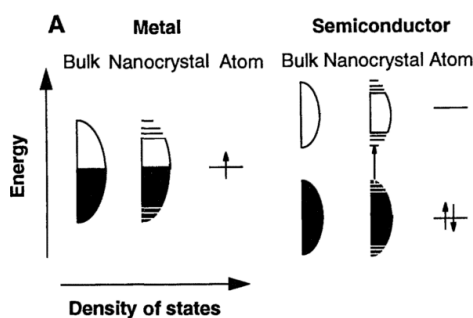
Figure 1.1: Schematic illustration of the density of states in metal and semiconductor clusters.
Reprinted with permission from[4]

other materials, when reducing the size of the material, the overall density of states is decreasing
leading to the quantization of the lowest DOS energies. Metals are characterized by a superpo-

sition of the valence and the conduction band producing a single band. In absence of external potential the Fermi energy lies at the centre of the band and the lowest DOS energies correspond to the edge of the band. Therefore, despite the strong neighbour interaction, the core properties are not influenced until clusters of few atoms. On the opposite, in semiconductors the Fermi energy level lies between valence and conduction band and the optical and electrical transitions are dominated by band edges. Therefore, small variation of the DOS in this region are leading to a wide variety of size-dependent properties, with different behaviours observed for different semiconductors.

Being size-dependent, the quantum confinement effect is also related to the shape of the produced structure. As the size of a material is shrinked on one or more dimensions to the nano-scale, the 3D structure can be reduced to 2D nanosheets, which are now having a rebirth after the discovery of graphene and graphene-like 2D materials[5],[6] 1D nanorods[7] or even 0D nanoparticles called Quantum Dots (QDs) in the case of semiconductors. [4]

The first paper looking for an explanation of the size dependent properties of what at that time was called small semiconductor crystallites has been published in 1983 by Louis Brus.[8] Since then, quantum dots have been protagonist of an astonishing number of patents and papers (more than 140000 until 2015, Thomson Reuters ISI Web of Knowledge). Their applications range is spacing from solar cells[9][10] to light emission[11][12] and luminescent biosensors[13].[14]

Since their discovery, QDs of almost every semiconductor have been prepared and their properties investigated; for instance II-VI group (e.g. CdX, X=Se, S, Te),III-V group (e.g. InP, InAs, GaAs), and IV-VI group (e.g. PbX, X = Se, S)[15] are the most studied binary alloys due to the interesting optical and electrical properties.

Despite the effort to implement these materials in everyday applications, those alloys are based on heavy and relatively rare elements. Moreover, in the case of lead or cadmium based QDs, the biocompatibility and the disposal of the exhausted material seems to be issues impossible to overcome.[16] For this reason, the interest in less toxic and more widely available elements as silicon and germanium has enormously increased in the QDs community, after the discovery of the luminescence of porous Silicon.[17] Notably, Silicon nanocrystals (SiNCs) are now outstanding thanks to the possibility to tune the surface functionality with covalent ligands, exploiting the well-known silicon chemistry,[18] and the unique optical properties,[19] introduced in the next section.

Optical properties

THE SIZE-DEPENDENT photophysics of Si nanostructures, and in particular SiNCs, is still under debate. The role of the surface chemistry is often superimposing to the quantum confinement effect in these nanocrystals due to the high sensitivity to oxydation or species dissolved in solution. As we will discuss in the next section, there are several synthetic approaches to produce SiNCs, and the optical properties are often incongrous. Nevertheless, the best results in terms of size-dependent photophysics are emerging for the SiNCs synthesized by high temperature processes, [19] which is also the technique employed by us in this dissertation. Therefore. the properties of this particular kind of SiNCs will be discussed in this section.
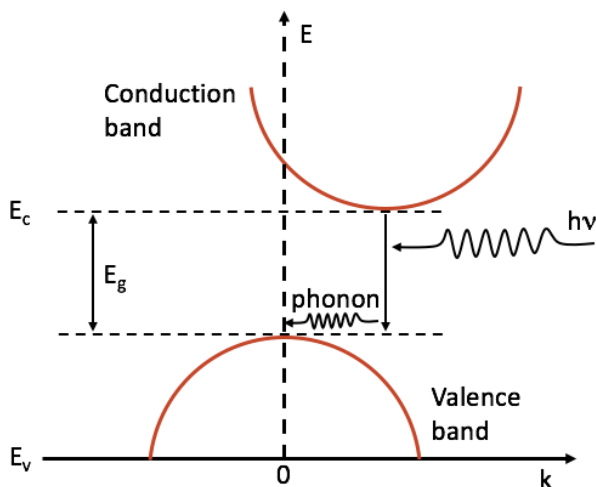

Figure 1.2: Silicon band structure scheme representing the typical phonon assisted transition from the conduction to the valence band.

The optical properties of a semiconductor are often explained by referring to the band structure diagram, where the energy of electronic levels is plotted as a function of the crystal wavevector k. Figure 1.2 shows the typical band structure of Si, that is characterized by a maximum of the valence band at $k=0$, and a minimum of conduction band located at $k \neq 0$ with an energy difference E_t about 1.1 eV, This is the typical band structure of an indirect band gap semiconductor, where any electronic transition is spontaneously followed by a phonon

relaxation.

The band gap of intrinsic Si can be tuned by decreasing the size from the bulk material to nanostructures with a typical size lower than 12 nm due to the quantum confinement effect. Both the absorption (Fig. 1.3 a) and the photoluminescence band (Fig. 1.3 b) can be shifted by tuning the size of the material, following the effective mass approximation.[20]
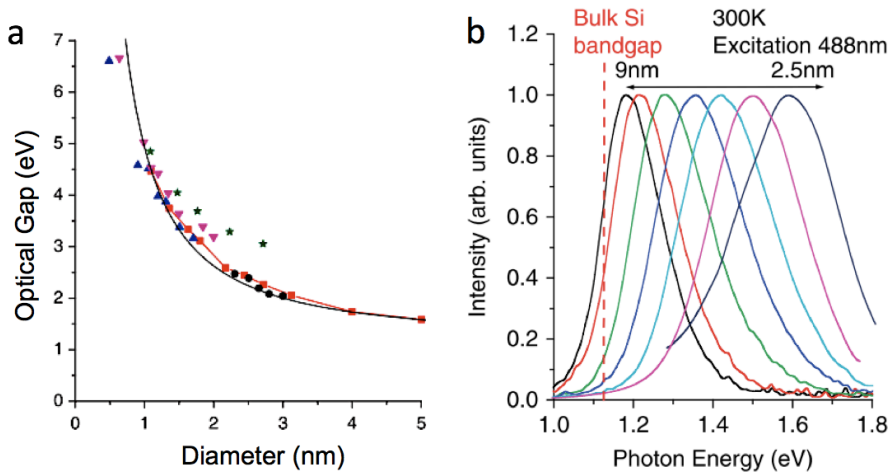
Figure 1.3: SiNCs band gap dependence on the size of the nanocrystals measured by a) absorption and b) emission spectra. Reprinted with permission from.[21]

Not only the energy of the states involved in the optical transition is affected by the quantum confinement effect, but also the relative efficiency of the excited state decay paths is size-related. The radiative and non-radiative constants can be extracted from two main optical properties of the nanomaterial, the photoluminescence lifetime and the quantum efficiency, which formula in absence of photoinduced chemical reaction is described in eqn. 1.1 .

$$\tau = \frac{1}{k_{nr} + k_r} \qquad \eta_{IQE} = \frac{k_r}{k_r + k_{nr}} \tag{1.1}$$

Typically, the experimentally observed SiNCs lifetimes are ranging from few μs to several ms, increasing with the size of the nanocrystal,[22] but those values are giving no information about the ratio between relative radiative and non-radiative constants. Anyway, the radiative

constant (or better its inverse, called the radiative lifetime τ_r) has been simulated to be dependent on the size of the nanocrystal with both ab initio and linear combination of bulk bands for silicon nanocrystals.[21] This trend can be explained by considering the relation proposed by Califano et al.[3] for semiconductor quantum dots, consistent to what happens to electronic transition in molecules. The τ_r for the transition from the excitonic state Ψ_i to the ground state is obtained by a standard time-dependent perturbation theory as described by equation 1.2:

$$\frac{1}{\tau_{r,i}} = \frac{4nF^2\alpha\omega_i^3}{3c^2}\left|M_2\right|^2 \tag{1.2}$$

Where α is the fine structure constant, n is the refractive index of the surrounding medium, F is the screening factor, ω_i is the frequency of the emitted photon, c is the speed of light, and M_i is the transition dipole moment. By considering Boltzmann occupation of higher-energy excitonic levels, it is possible to calculate a thermally averaged radiative lifetime $\langle\tau_r\rangle$ as follows.

$$\frac{1}{\langle\tau_r\rangle} = \frac{\sum_i \quad 1/\tau_i^r \, \exp{-\beta(\Delta E_i)}}{\exp{-\beta(\Delta E_i)}} \tag{1.3}$$

It should be noted that the radiative lifetime is reduced exponentially as the energy of the transition ΔE_i, in this case corresponding to the band gap E_g, is increased; therefore by decreasing the nanocrystal size the excitonic radiative constant is expected to increase, turning the indirect bandgap bulk material into efficient light emitter. This analysis is not taking into account the effect of the non-radiative constant on the luminescence lifetime, therefore this value cannot be directly compared to the experimentally measured photoluminescence lifetime, even though the trend observed is similar, as shown by figure 1.4 b). Further information about the ratio between k_{nr} and k_r can be obtained by evaluating the internal quantum efficiency (η_{IQE}). Unfortunately this value cannot be experimentally measured, but only derived from the photoluminescence quantum yield (QY or ϕ), defined as the ratio of emitted to absorbed photons. For alkyl passivated SiNCs, the QY has been observed to be increasing from less than 5%, as observed for 1.0nm SiNCs, to more than 45% for bigger nanocrystals, as shown in figure 1.4 a). Two explanations have been proposed for this behaviour: Mastronardi et al.[22] assume that the QY value are the internal quantum efficiency are directly correlated, and so to the k_r and k_{nr} value can be extracted from the QY value with no further treatment. They explain the variation of QY with the strong influence of the non-radiative rate k_{nr} for the smaller nanocrystals, prevailing on the radiative component and reducing both lifetime and quantum yield.
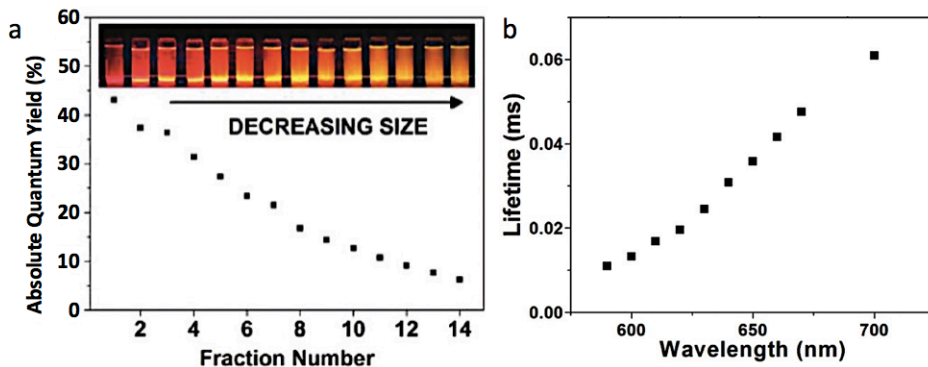
Figure 1.4: Size-dependent photoluminescence properties of size-selected Allylbenzene passivated SiNCs. A) Absolute quantum yield plotted against fraction number, corresponding to decreasing size of SiNCs and b) Photoluminescence lifetime vs emission wavelength, correlated to the increasing size of the nanocrystals, as evident from picture 1.3. Reprinted with permission from. [22]

On the contrary, a second hypothesis by Sangghaleh[23] is taking into account that the real world produced SiNCs are always an ensemble of nanocrystals with different size and optical properties and, as a consequence, the QY is averaging all the behaviours in the SiNCs assembly, following this relation:

$$\phi = \frac{\Sigma_1^{N_{bright}} \, \delta_i \, IQE_i}{N_{bright} + N_{dark}} \qquad (1.4)$$

Where δ is the so-called blinking duty cycle (fraction of time in ON-state), N_{bright} and N_{dark} are the number of bright and dark NCs, respectively. To understand this, we first have to consider which are the mechanism responsible for the non radiative channels; these mechanism can be classified:

- fast non-radiative transitions, like Auger process with a decay time of few nanoseconds[24] due to dangling bonds, defects, etc., which make nanocrystals dark;

- nonradiative channels with the decay rate similar to the radiative one which consequently affects IQE;

- slow nonradiative transitions (e.g., blinking with characteriztic times of seconds or even minutes).

Equation 1.4 is taking into account all of these mechanism. While the long blinking effect are taken into account by the blinking duty cycle, the presence of fast decays as Auger recombination or carrier multiplication[25] are completely quenching the luminescence of the NCs, resulting in a distribution of ON and OFF nanocrystals as described by the equation denominator. The remaining non-radiative decays are the one affecting not only the QY, but also the η_{IQE}, because the decay rate is similar to the radiative recombination one. Following this hypothesis, the alkyl passivated SiNCs have been demonstrated to exhibit 100% η_{IQE} in a full emission energy range, without showing any μs non-radiative decay and, therefore, being characterized by superior intrinsic photoluminescence properties. As a consequence the contribution of the k_{nr} to both the photoluminescence lifetime and the quantum yield has to be neglected. This hypothesis is also consistent to what was both calculated and experimentally observed for oxide embedded SiNCs, proving the η_{IQE} relation with surface chemistry. For these nanocrystals the quantum efficiency is almost unitary for NCs with a diameter bigger than 4-5 nm and a luminescence maximum wavelength higher than 900 nm, but it starts decreasing upon decreasing the size of the nanocrystals due to the rising of μs non-radiative decays.[26]

Finally, the whole treatment of quantum efficiency and lifetimes has been demonstrated to be greatly influenced by the presence of heteroatoms on the surface of SiNCs, as for example nitrogen impurities[27] or diols,[28] turning the red/near IR luminescent SiNCs with μs range charachteristic lifetimes into blue emitting SiNCs with fast luminescence lifetimes of few nanoseconds.

This should prove once again the complexity of the photophysics of this system and the utmost importance of the material's synthesis, in order to better understand and optimize the application of this material into optoelectronic devices.

1.1.2 Silicon nanocrystals syntesis

MANY SYNTHETIC PATHS were developed to produce Si nanocrystals. The most important ones are gathered together in the scheme displayed by Fig. 1.5, where two main steps are evident: the nanocrystals nucleation and the preparation of the final material in solid or liquid phase. The first step can be approached in both a bottom-up and a top-down approach, producing nanocrystals with different quality, synthetic efficiency and processability.
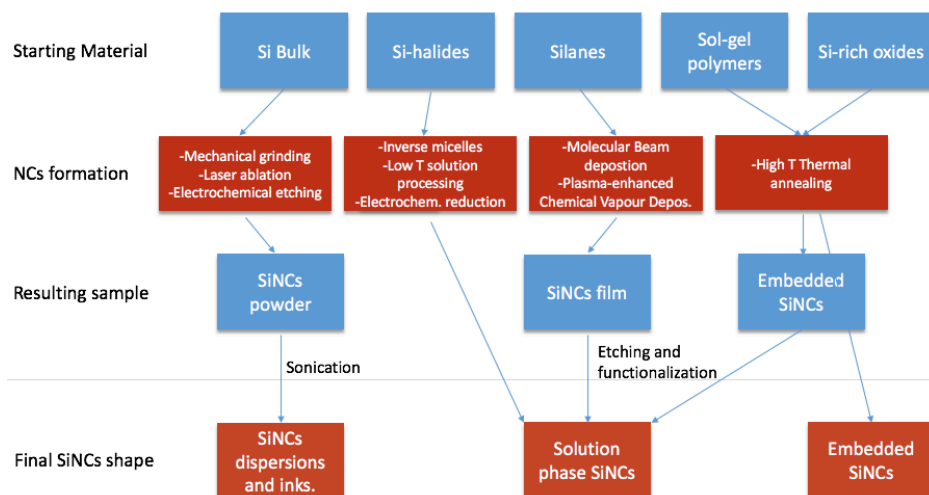
Figure 1.5: Scheme describing the synthetic paths, adapted from Donhalova et al.[29]

The first methods to be developed were based on the SiNCs growth in solid matrices, directly arising from the silicon industry. Superior quality samples with good control over the size and density, and with high quality of the passivating thermal oxide can be prepared by ion implantation of silica, plasma enhanced chemical vapour deposition[30] (PE-CVD) and molecular beam deposition (MBE). The most used technique involves the thermal annealing of sub stoichiometric Silicon oxide (SiO_x, x<2) producing high quality SiNCs but in a very small amount. All these techniques suffer from the constraint of the silica matrix, which limits the already weak size tunability of emission and the charge extraction, fundamental to electronics and photovoltaic application.

The preparation of a colloidal dispersion of nanocrystals is required for many application, thanks to the ease of handling and higher flexiblity compared to the solid matrix. The first and very straightforward approaches to produce liquid phase dispersions of SiNCs were based on the mechanical crushing,[31] laser ablation or electrochemical etching[32] of a Si wafer, followed by the HF etching of the native oxide matrix to produce a liquid based suspension of H-terminated Si nanocrystals. This method suffers from a very poor control of size and properties of the material produced, but it can be a viable alternative to produce high amounts of low cost (and quality) SINCs. A much higher control can be reached with some bottom-up

techniques as laser pyrolysis,[33] but also plasma synthesis is able to produce extremely high quality material with a very promising scalability, despite a slightly complex experimental setup.[30]

Several solution phase synthesis were also developed, among which the most interesting ones are nowadays based on either using the inverse micelle technique (the so-called Tilley's method),[34] the preparation from supercritical fluids,[35] thermal processing of organosilicon compounds[36] or electrochemical reduction of $SiCl_4$.[37] Most of these techniques lead to SiNCs with bright emission in the blue-green region of the visible spectrum with short fluorescence lifetimes in the range of ns, arising from the different amount of surface defects compared to the material produced by the "physical" methods. Moreover, the control over the size and the luminescence properties achieved with those methods is still not sufficient compared to the one obtained for the direct band-gap semiconductors QDs prepared with similar techniques.

An hybrid method based on the high temperature annealing (1000-1400°C) of a solid silicon rich/silicon oxide precursor and subsequent HF etching of the Silicon oxide matrix has also been developed, in order to join the high size control given by the thermal process with the flexibility of the free-standing nanocrystal. The silicon precursor can be either commercialy available, as in the case of the hydrogen-silsesquioxane[38] (HSQ or FOX-16 Dow-Corning®), or prepared by the sol-gel polymerisation of an alkoxy or halide Silicon precursor.[39]

1.1.3   SiNCs functionalization

The synthetic methods discussed in the previous section are often producing hydride terminated SiNCs dispersions, whose properties are far away from the ones discussed in the introduction. Indeed, despite the highest surface coverage and the negligible influence of the H atoms on the Si core properties, these nanocrystals show extremely poor colloidal stability and the Si-H bond is strongly unstable against oxidation.[40] The Si-O bond, in its turn, is stable and can be further functionalized to provide solubility to the nanocrystals, but this is resulting in a poor size-dependent spectral tunability[41] and a decreasing of the radiative decay rate.[42]

Si-H bonds are also very reactive to carbon derivatives, forming Si-C bonds that are very stable against photo-oxidation. A wide database of carbon coupling reaction on Silicon surface has been inherited from bulk Silicon and Porous silicon chemistry experience.

The addition of Carbon based molecule to a Si-H bond can occur by the hydrosilylation reaction, usually taking place in presence of an unsaturated carbon derivative by providing an external energy input to the reaction mixture. The very simplest way to initiate the reaction is by thermally activating the Si-H bond, homolitically cleaving away the hydrogen group and providing a very reactive surface silyl radical that is able to efficiently react with terminal alkenes or alkynes. This reaction is often carried out in pure ligand solution under inert atmosphere or in gas phase, achieving a surface coverage degree as high as 58% in case of Acetylene/Phenylacetylene subsequent exposures, close to the teoretically predicted maximum of 60% for Si (1,1,1).[43]

Taking into account the radical nature of the hydrosilylation mechanism, it is not surprising that the unsaturated ligand undergoes oligomerization at the typical reaction temperatures,[44] leading to a thick insulating carbonaceous layer that is both responsible for the optimal photophysical and stability properties, but also presents a challenge for any application in optoelectronic devices. In addition to the low control on the shell thickness, thermal hydrosilylation has also some further limitations, such as the need for high temperature stable ligands and passivating agents, usually long terminal alkenes as 1-dodecene or 1-dodecyne, and high boiling point solvents.

A very interesting alternative to thermal activation can be the photochemically induced hydrosilylation, enabling room temperature reaction upon irradiating the sample with near-UV[45] or far UV light.[46] Also this reaction suffers from intolerance to several chemical functionality, in particular in case of light absorbing ligands.

Room temperature hydrosilylation was also achieved via borane catalyzed passivation of the SiNCs with different legth alkylic chains.[47] Therefore, a pure chemical approach can also be promising, by using either a coupling catalyst such as a Platinum complex,[48] or a radical initiator. While transition metal complex are known to influence the photophysics of the SiNCs due to the difficult removal from the reaction batch, radical initiators are usually organic molecules that can be more easily separated. The first attempt has been reported by Hölein et al. in 2014 by using diazonium salts as initiator.[49] This synthesis has been shown to be adaptable to various functional groups as alkenes, alkynes, methyl methacrylate or even a chlorodimethyl-(vinyl)silane suitable to post-functionalization reaction.[50]

Mixed ligands monolayers can be produced by exploiting the ability of organolithium

species to react with Si-Si bond,[51] producing a partial coverage of the SiNC surface that can be followed by a radical initiated hydrosilylation. The hydride terminated SiNCs
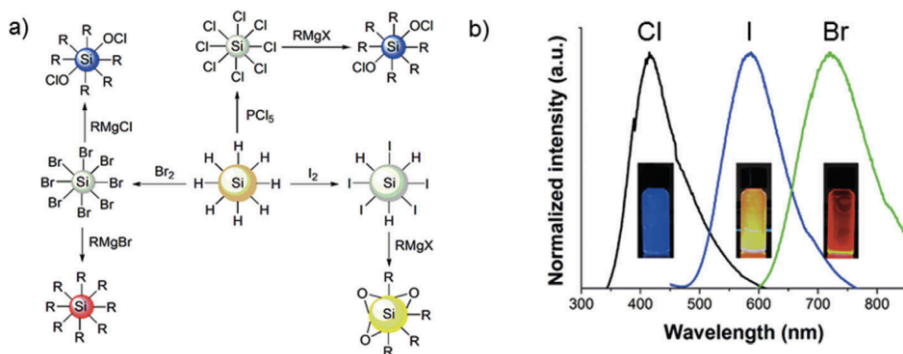
Figure 1.6: a) Scheme describing typical routes for halogenation and alkylation of hydride terminated SiNCs. b) Photoluminescence spectra of alkyl passivated SiNCs derived from (A) chloride, (B) iodide, and (C) bromide surface. Reprinted with permission from.[52]

also spontaneously undergo several halogenation reactions using different approaches to get either chlorinated,[53] brominated[54] or iodined terminated nanocrystals (figure 1.6). Despite the strong interest in the activation of the Si-H bond through alkylation, the photoluminescence properties and the morphology are dramatically affected by the presence of these electron-donating groups,[52] therefore the direct hydrosilylation reaction is still representing the only route to tune the surface of the nanocrystals preserving the peculiar optical properties of the Si core.

In addition to the synthetic path exploited for the functionalization of the SiNC, another extremely relevant factor to the properties of the nanocrystal lies in the nature of the ligand functionality. The coating molecule in the first place represents the surface of the nanocrystal, therefore all the surface properties as solubility, aggregation and chemical interaction are basically depending on the functional groups exposed by the ligands. Several attempts were made for instance to functionalize the surface of SiNCs with carboxylic group[55],[56] amine[57][58] or diol-terminated[28] alkylic chains, in order to increase the solubility in highly polar solvents as alcohols or water. Further effort was made to add more complex functionalities as PEG chains[59][60] or DNA strands[61] to increase the stability in biological environment and address the interaction with specific cells for bioimaging purposes.

Few more complex ligands were studied for SiNCs, mainly due to the intrinsic limitations given by the experimental conditions of the hydrosilylation reaction and already described in this section. Anyway, the implementation of organic-inorganic hybrid interface with functional capping molecules can be crucial for the application of these kind of nanocrystals in optoelectronic devices [62] or solar cells. [63] For instance, several conjugated organic groups as phenylacetylene [64] or 4-ethynyl-N,N-bis(4-methoxyphenyl)aniline [65] were coupled to SiNCs surface to tune the bandgap without affecting the core structure and increase the charge transport from the core to the surface.

1.2 SiNCs synthesis and passivation: experimental techniques

Despite the wide range of techniques for SiNCs synthesis and passivation, their performances are strongly affected by the experimental setup devised in each individual laboratory. Here we report few experimental procedures we developed and adapted from the techniques already described in the previous section.

1.2.1 SiNCs nucleation in non-stoichiometric oxide

Recently, among all the approaches described in the previous section, the thermal annealing of silicon-rich oxide precursor is becoming the most used technique to prepare SiNCs because of the high reproducibility, the narrow size distribution and the relatively simple procedure.[38] The first step of this synthesis is producing freestanding SiNCs with hydride terminated surface that can be functionalized with carbon-based molecules by conventional organic chemistry reactions, described in the next sections. In our laboratory the hydride terminated SiNCs are prepared thermal disproportionation of commercially available Hydrogen Silsesquioxane (HSQ). In a typical synthesis 40 mL of Dow-Corning FOX-16® HSQ dissolved in a methyl-isobutyl-ketone/toluene mixture are dried under vacuum for 24 h until a glassy white powder is obtained. The powder is collected and transferred onto a quartz boat. The sample is then put in a tube furnace and heated under forming gas ($93\%N_2/7\%H_2$) following the temperature ramps shown in Fig. 1.7. It should be noted that two annealing temperature ramps are performed, with 1100°C and 1200°C maximum T, producing SiNCs with respectively ~3 and ~5 nm of nominal diameter (deeper morphological characterization will follow in the next chapter). Once cooled down, the brownish powder is manually grinded on a mortar, then it is transferred in a glass vial and 20-30 glass beads are added to the powder. Later the powder is milled in a homemade homogenizer for 8-12 h in order to obtain fine and homogenous grain size. This powder is basically a SiO_2 matrix inside which the SiNCs are already embedded. The $SiNC/SiO_2$ composite is etched with 48% HF and 37.5% HCl (10:1 v/v) in the dark for 4-6 hours and then centrifuged at 8000 rpm for 5 min. The clear surnatant is removed and the precipitate is rinsed with ~ 15ml of deionised water, then the centrifugation step is repeated and the precipitate washed twice with ethanol (15 ml in polypropilene centrifuge tube then
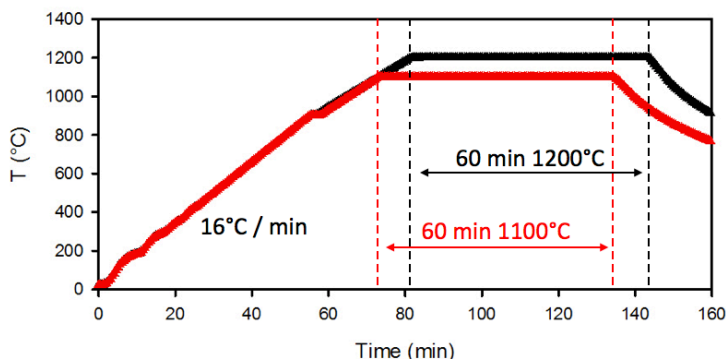
Figure 1.7: Thermal annealing ramp at 1100°C (red) and 1200°C (black). The whole annealing is performed under N_2/H_2 atmosphere with $93\%/7\%$ ratio and an overall flux equal to 3 standard liter per minute.

transferred in glass centrifuge tube with 8 ml of ethanol), then twice with 8 ml of chloroform in order to quench the residual HF. After removing the chloroform surnatant as much as possible, taking care not to lose the nanocrystals precipitate, the hydride terminated nanocrystals can be functionalized with one of the techniques described henceforward.

1.2.2 SiNCs passivation

Thermal Passivation

THE THERMAL PASSIVATION technique of silicon surface has been directly inherited by the conventional silicon chemistry. The kinetically metastable Si-H bond can be homolitically cleaved by providing external energy, producing an highly reactive silyl radical. Unsaturated alkenes or alkynes are known to react with this radical with a small activation barrier to produce a β-silyl radical with a covalent Si-C bond. [66] The reaction is propagated until an hydrogen is abstracted from some other species in solution, as explained in figure 1.8.

Experimentally, after the etching the silicon oxide matrix, 3-4 mL of 1-dodecene (or different ligands if needed) are added to the brownish precipitate of hydride terminated SiNCs; then the turbid dispersion is transferred in a three-neck flask and put through three freeze-pump-thaw
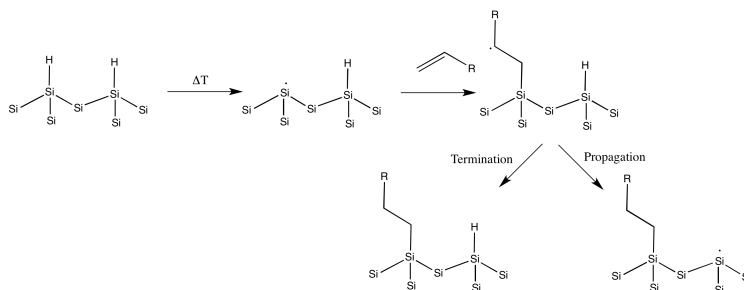
Figure 1.8: Schematic representation of the homolytic cleavage of Si-H bond and consequent radical activated hydrosilylation process.

cycles. Finally the dispersion is heated to 170°C under N_2 flow for 12 hours, by controlling the solution temperature with a thermocouple. Over time, the dispersion becomes optically clear, indicating that passivation of Si nanocrystals occurred. To purify the nanocrystals, the solution is transferred to glass vial and an anti-solvent is added, usually 30-40 ml of acetone or ethanol, until the solution becomes again turbid. The nanocrystals can be therefore separated by the excess ligand (dodecene for the simple passivation) by using centrifugation or filtration of the dispersion, depending on the solubility of the ligand. In the case of filtration, the SiNCs dispersion is simply passed through a 0.20μm PTFE syringe filter with large radius, then 10 ml of anti-solvent are passed through the filter to remove the ligand residuals and finally the same procedure is repeated with 1-2 mL of Toluene to redisperse the topping layer of nanocrystals stuck in the PTFE filter. The centrifugation technique is also based on the precipitation of the un-soluble nanocrystals: the solvent/antisolvent mixture is transferred in a glass centrifuge tube and spinned at 8000 rpm for 6 min, the surnatant is carefully removed and the same amount of anti-solvent is added. The process is repeated until no hint of residual ligand is observed by absorption or fluorescence spectra. Finally, the anti-solvent residuals are removed by vacuum pumping and redispersing the nanocrystals in spectroscopic toluene.

With the thermal passivation methodology, SiNCs are produced in a good amount and the PL quantum yield is usually around 15% for the 3 nm sized SiNCs and 45% for the 5 nm ones. The principal ligand should be 1-dodecene or analogue liquid and high boiling point alkene to ensure the complete passivation of SiNCs surface.

Light induced passivation

As PREVIOUSLY DISCUSSED, the hydrosilylation reaction can also be initiated by deep or near-UV irradiation in inert atmosphere. Despite the first example of UV-initiated hydrosilylation of a silicon surface (bulk silicon) is dating back to 2000,[67] the reaction mechanism is still strongly under discussion, especially when dealing with porous silicon or nanocrystals. A plurality of mechanism has been proposed,[68] such as photoinduced homolytic cleavage of the Si-H bond (analogue to the thermal reaction), exciton-driven hydrosilylation or photoemission induced coupling. The energy of the radiation is also influencing the mechanism of the reaction and the kinetics, for instance wavelengths below 380 nm has been found to induce hydrosilylation of Si(III)-H surface within few minutes through a radical mechanism, whereas higher wavelengths require up to 24h to obtain similar results because the hydrosilylation mechanism has been attributed to the exciton-mediated addition of the alkene.[69] The same behaviour was observed for SiNCs[45], [46] even if the kinetics are different due to the different optical properties, as discussed in the previous section.

The UV induced functionalization is a valid alternative to thermal functionalization wherever the ligand or some ligand functionalities are not stable at high temperature. For instance, bifunctional alkenes or alkynes are not trivial to couple to Si surface because of the competition between the reactivity of the unsaturated bond and the second functional group with respect to Si-H, which is often hard to predict at high temperatures. In order to mantain the second functionality intact, UV hydrosilylation could be used to selectively activate the Si-H bond without addressing any other group in the reaction environment.[70] UV hydrosilylation has also revealed to be useful for the functionalization of SiNCs with styrene or phenylacetylene, which is often impossible with the thermal method due to the proneness of these molecules to spontaneously polymerize and precipitate from solution.[45]

Our procedure for the UV initiated functionalization of SiNCs with, for instance, dodecene, was developed as follows:

A large excess of ligand (e.g. 2-3 mL of dodecene) is added to the brownish precipitate of hydride terminated SiNCs. The dispersion is rapidly sonicated and transferred in a modified quartz cuvette provided with vacuum manifold compatible stopcock and a PTFE valve. The
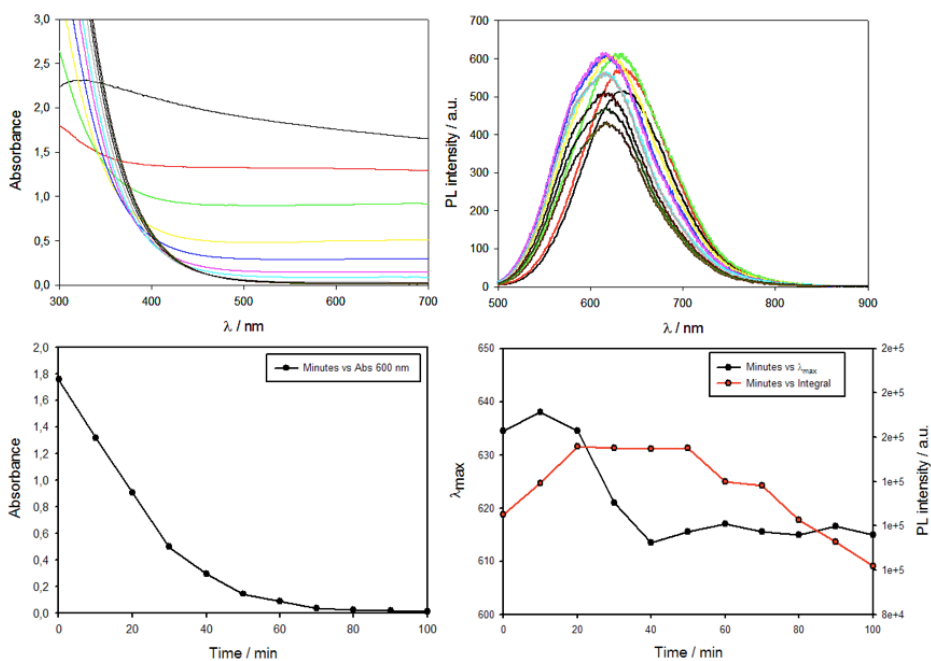
Figure 1.9: a) Absorption and b) photoluminescence spectra of SiNCs during UV-initiated hydrosilylation with 1-dodecene. c) trend observed for the absorbance at λ=600 nm; d) trend observed for the maximum of the SiNCs photoluminescence band (λ_{max}, black line)and the integral of the same band (red line).

solution is then irradiated under agitation with a UV source, in this case a 15W low pressure Hg lamp characterized by a sharp peak at $\lambda_{em} = 254nm$. Due to the particular setup, the trend of the synthesis can be followed by absorption and fluorescence specra. Figure 1.9 a) shows the absorption spectra of the dispersion registered after every 10 minutes of irradiation up to 100 min. At the beginning of the irradiation the spectrum (black) is characterized by a flat band slightly increasing in the UV region and an high value of absorbance in the whole spectrum, related to the bad dispersion of the H terminated SiNCs. Upon irradiatiion, a new band was observed to rise in the UV region, related to the band-gap of SiNCs, while the baseline slowly decrease to values close to 0, as showed in figure 1.9 c) by plotting the Absorbance value at 600 nm vs time of irradiation. It should be noted that the absorbance stabilizes after $\sim$60 minutes, highlighting the complete solubility of SiNCs after this amount of time. Fluorescence spectra cannot be directly used as a fingerprint of the variation of the brightness of the nanocrystals, because the scattering of the initial solution prevents any quantitative analysis, but they can still give some information about the rate of functionalization. Figure 1.9 b) displays the luminescence spectra of SiNCs during the UV irradiation ($\lambda_{50\%} = 400nm$); even if the photophysics of SiNCs will be thoroughly discussed in the next section so for the moment the band shape and nature is not of interest, but we still can exctract some values to understand how the reaction is proceeding. Indeed, by plotting the maximum photoluminescence intensity (λ_{max}) and the integral of the photoluminescence band against time, we can obtain a graph like the one reported in figure 1.9 d). It might be noted that both λ_{max} and the PL integral reach a plateau after $\sim$30-40 minutes, but the PL intensity starts to decrease after 60 minutes to lower values. By comparing the results obtained by the absorption spectra, we can asses that the functionalization is complete after $\sim$60 min. but after that time the luminescence starts decreasing probably due to the photobleaching of SiNCs.

With this technique it is possible to prepare SiNCs with PL quantum yield values equivalent to the ones observed for the thermal passivation. In addition, ligands as styrene can be effectively coupled to SiNCs minimizing the spontaneous polymerization of the otherwise thermally reactive monomer. To do so, the irradiation is carried out with a spectrofluorimeter equipped with an high power Xe lamp (Jobin-Ivon Horiba Fluoromax), setting the excitation monochromator wavelength to 350 nm (slits = 10 nm). In this case, the typical reaction time with the styrene ligand is about 16h. The PL QY for this sample stands at the same values observed for the dodecene functionalized SiNCs.

Diazonium salt activation

The chemical activation of the Si-H bond by a radical initiator has been recently demonstrated to be a viable alternative to prepare functionalized SiNCs at room temperature. Among the proposed techniques, the diazonium salt activation revealed to be the most reliable methodology and the low temperature and relatively fast reaction allowed to prepare SiNCs with several functional groups on the surface.[50] In particular, by coupling a chlorodimethyl(vinyl)silane on the surface of SiNCs it is possible to post-functionalize the nanocrystal through the hydrolysis of the chloride with a silanol, following this technique:

Figure 1.10: Schematic representation of the synthetic path to post-functionalize chlorodimethyl(vinyl)silane passivated SiNCs produced by 4-decyl diazonium salt initiated hydrosilylation.

The brownish precipitate of hydride terminated SiNCs is collected after the centrifugation and brought into a Glovebox. 1.2 mL of previously deoxygenated toluene are added and the solution is stirred to disperse the nanocrystals. To the turbid solution, 0.2 mL of chlorodimethyl(vinyl)silane and 1 mg of 4-decyl diazonium salt are added and left stirring overnight. After few minutes the solution is already turned to transparent. The vial containing the solution is then removed from the glovebox and the solution is dried under vacuum to remove the excess chlorodimethyl(vinyl)silane. 1 mL of fresh toluene is then added to redisperse the nanocrystals, then 122 mg of dodecyldimethylsilanol and 2 mg are added. The solution is left under agitation for 24 h in inert atmosphere, then the SiNCs are cleaned by conventional centrifugation or filtration procedure.

The ligand for the post-functionalization, in this case dodecyldimethylsilanol, can be virtually replaced with any silanol, opening the way to a wide variety of different ligands with functional groups sensible to the thermal or photochemical technique.

1.3 Light harvesting effect in pyrene functionalized SiNCs

One of the main disadvantage of SiNCs, compared to direct band gap QDs or organic fluorophores, is the low molar absorption coefficient, limiting the application in optoelectronic devices. On the other hand, SiNCs are showing very promising characteriztics, such as highly size-dependent tunable luminescence, long emission lifetimes and photoluminescence quantum yield as high as 45%. All of these properties, as already discussed in the previous section, are depending on the quantum confinement effect related to the silicon core; therefore the only way to tune the optical and electrical properties without harming the core properties is to focus on the organic ligand.

In particular, in this section we report the light harvesting in SiNCs covalently functionalized with photoactive molecules absorbing in the near UV region, i.e. pyrene derivatives. We also investigated the role of the linking alkylic chain on the energy transfer efficiency and the effect of the silicon core size on the light harvesting.

1.3.1 Synthesis of the pyrene-based ligands

Two pyrene derivatives were prepared by coupling a pyrene moiety with an unsaturated alkylic chain. The two pyrene derivatives are only differing by the length of the alikylic chain acting as a bridge between the pyrene moiety and the terminal vinyl bond needed for the hydrosilylation reaction. In particular a short chain ligand, the 1-(allyloxymethyl)pyrene ($(C_3)Py$), and a long chain one, 1-((undec-10-enyloxy)methyl)pyrene ($(C_{11})Py$), were synthesized as follows.

1-(allyloxymethyl)pyrene and 1-((undec-10-enyloxy)methyl)pyrene synthesis. Sodium hydride (0.124 g, 5.16 mmol, 1.2 eq) was added to a mixture of 1-pyrenemethanol (1.00 g, 4.30 mmol, 1eq), propargyl bromide (0.645 g, 5.33 mmol, 1.24 eq) in CH_3CN (25 mL) at 70°C to synthesise 1-(allyloxymethyl)pyrene. For the preparation of 1-((undec-10-enyloxy)methyl)pyrene the propargyl bromide has been replaced with 11-bromide-1-undecene (1.504 g, 6.45 mmol, 1.5 eq). The reaction mixture was stirred vigorously for 48 h at 80°C. After the completion of the reaction, three drops of H_2O were added to the reaction mixture to quench the reaction.

The mixture was extracted into chloroform(3 x 5 mL). The chloroform layer was dried over MgSO$_4$ and the solvent was removed under reduced pressure to give the crude product. The resulting residue was purified by silica column chromatography (Hexane/ EtOAc 8:2), to give the product as a yellow solid ((C$_3$)Py yield = 66 %, (C$_{11}$)Py yield = 80%).

Detailed NMR characterization has been reported in Appendix C.

1.3.2 SiNCs synthesis

THE SILICON NANOCRYSTALS were synthesized following the thermal passivation described in the previous section. Namely, the etched nanocrystals were dispersed in 5 mL of a previously freeze-pumped dispersion of the desired ligand mixture in a molar ratio with dodecene ranging between 0.028 (1:12) and 0.083 (1:36). After the thermal step the solutions were thoroughly purified with several centrifugation cycles, removing the surnatant containing the free ligand and washing the precipitate with acetone until no trace of free ligand was observed. For each SiNCs size ($\sim$ 3 nm or 5 nm) we prepared a pyrene functionalized batch of SiNCs, henceforward called SiNC(C$_3$)Py for the 1-(allyloxymethyl)pyrene functionalised SiNCs, and SiNC(C$_{11}$)Py for the 1-((undec-10-enyloxy)methyl)pyrene functionalised ones. In parallel a control sample was prepared by passivating the nanocrystals only with 1-dodecene (SiNC), in order to carefully compare the properties of the functionalized SiNCs with the ones of the silicon core with no photoactive ligand in our experimental conditions.

The final SiNC, SiNC(C$_3$)Py, SiNC(C$_{11}$)Py samples were dispersed in toluene at a concentration of 3-5 mg/mL until further characterization. The overall synthetic path is summarized in Figure 1.11.

1.3.3 Structural, morphological and optical characterization

AS ALREADY MENTIONED, the photophysical properties of SiNCs are depending on mainly three features:

- Size of the silicon core.

- Crystal structure.
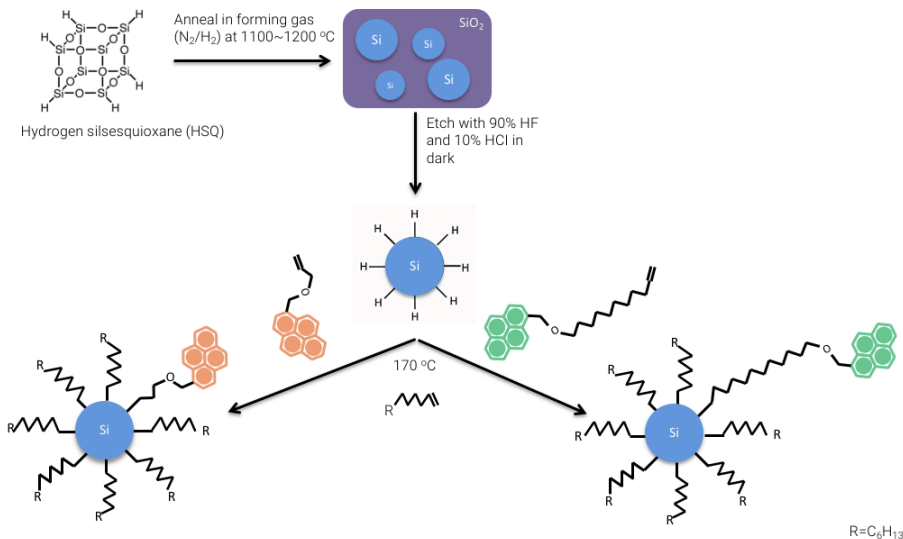
Figure 1.11: Schematic representaition of the synthesis of SiNC(C$_3$)Py and SiNC(C$_{11}$)Py

- Surface chemistry.

The size ditribution of the nanocrystals has been extracted from the HR-TEM and STEM characterization of the nanocrystals solutions. Details on the electron microscopy characterization are shown in Appendix B.

Figure 1.12 a) and b) show the typical TEM micrographs of SiNC(C$_3$)Py batches prepared respectively at 1100°C and 1200°C. The size distribution obtained from these images is displayed in Figure 1.12 c) and d) and the average diameter was calculated to be respectively equal to 2.6 nm and 5.0 nm.

No significant variation of the size distribution was observed for the SiNC(C$_3$)Py sample, where the average size assessed at 2.9 ± 0.7 nm for the 1100°C SiNCs and 5.3 ± 2.0 nm for the 1200°C ones. The STEM micrographs shown in Figure 1.13 are also proving the quasi-spherical shape of the nanocrystals resulting from the lack of a preferential growth of the Si lattice on a given axis. Due to the negligible variation in size between the prepared samples, henceforward we will refer refer to these nanocrystal batches as 3 and 5 nm SiNCs.
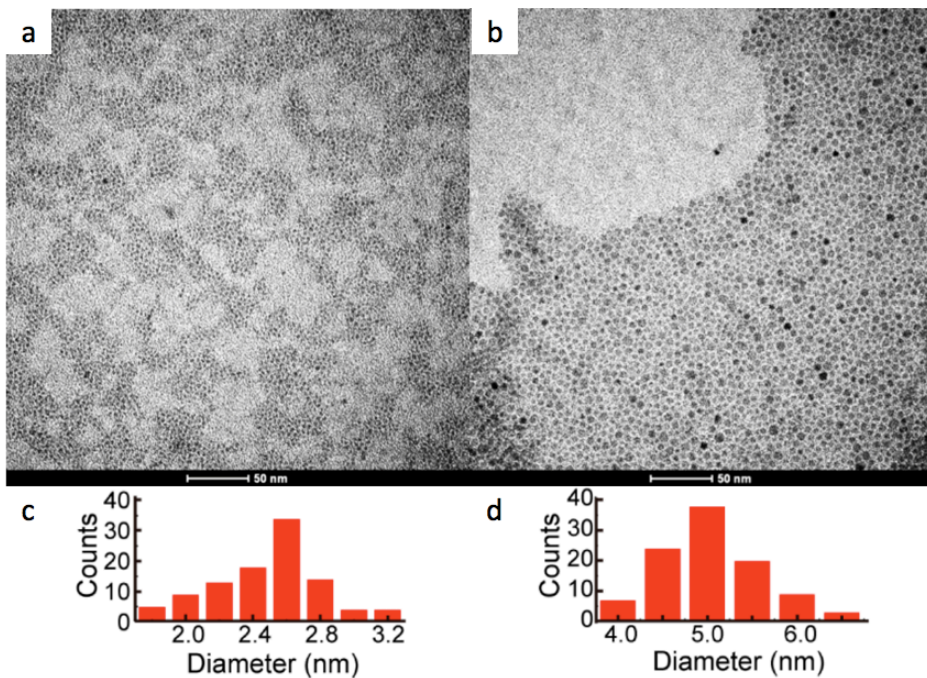
Figure 1.12: *a and b)* TEM micrographs of SiNC(C$_3$)Py prepared at 1100° and 1200° and *c and d)* relative size distribution histograms.
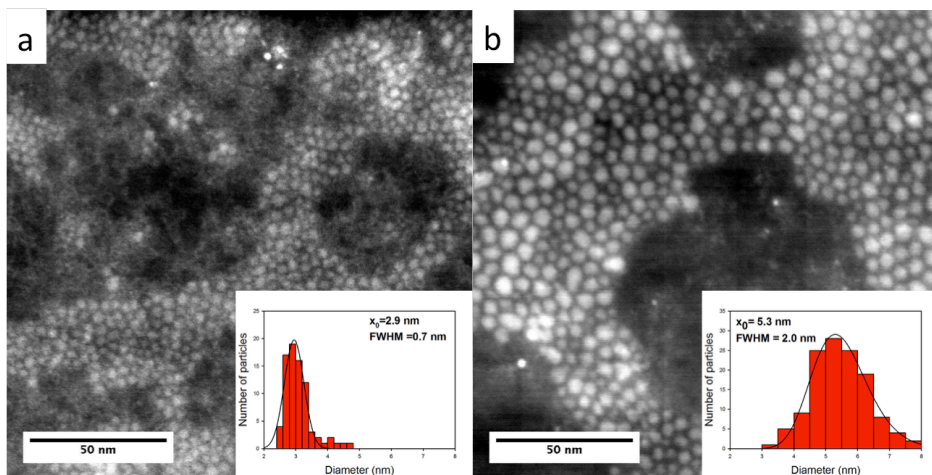
Figure 1.13: *a and b)* STEM micrographs of SiNC(C$_{II}$)Py prepared at 1100° and 1200° and relative size distribution histograms in the inset.

Chapter 1   Silicon nanocrystals functionalized with photoactive molecules

X-ray diffraction of these nanocrystals is characteriztic of diamond cubic Si ($PDF027 -$ 1402, $a = b = c = 5.43088$ Å[71]); as evident in Fig. 1.14 a) the broadening of the diffraction peak is proportional to the size of the crystal domain, here corresponding to the size of the nanocrystal itself. Also the SAED pattern shown in Figure 1.14 b), taken on the SiNC(C_{11})Py 5 nm sample, shows broadened diffraction rings representing the same crystal lattice described by the XRD analysis.
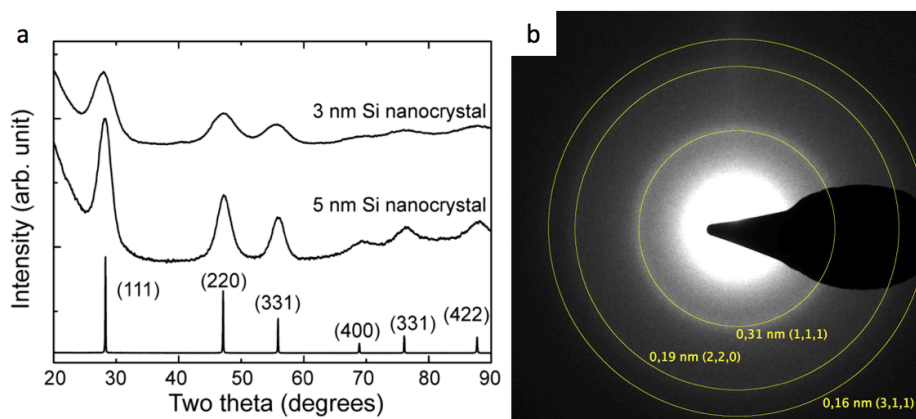

Figure 1.14: *a)* XRD spectra (λ=0.154 nm) of 3 and 5 nm diameter SiNC(C_{11})Py; *b)* SAED pattern observed on a 5 nm SiNC(C_{11})Py assembly.

Finally, as regards the surface chemistry, this had been studied by FT-IR and X-ray Photoelectron Spectroscopy. The FT-IR spectrum of SiNC (Figure 1.15 a) shows the typical features of $\nu_{(C-H)}$ stretching at 3000-2850 cm^{-1} and $\delta_{(C-H)}$ bending at 1500-1350 cm^{-1}; while a certain degree of oxidation is highlighted by the strong $\nu_{(Si-O)}$ stretching at 1024 cm^{-1}. For SiNC(C_{11})Py, the covalent attachment of the ligand to the surface is confirmed by the presence of aromatic $\nu_{(C-H)}$ stretching at 3100-2890 cm^{-1}, the $\nu_{(C=C)}$ stretching at 1640 cm^{-1}, and the $\delta_{(C-H)}$ bending at 1480 and 940-800 cm^{-1}. There is no evidence of $\nu_{(Si-H)}$ (ca. 2100 cm^{-1}), consistent with effective functionalization.

The XPS spectra in figure 1.15 b), performed both on 3 nm and 5 nm SiNC(C_{11})Py shows the presence of the typical $Si^{\circ}_{3/2}$ and $Si^{\circ}_{1/2}$ at 99.6 and 99.8 eV, corresponding to the bulk Si core of the nanocrystal, together with a broad peak at 101.9 eV corresponding to the superficial Si-C bond. Small evidence of Si-O peak at 103.7 eV is visible for both sizes of nanocrystals,

but it seems to be negligible compared to the Si-C and Si-Si ones. The different intensity ratio between these peaks in 3 and 5 nm $SiNC(C_{II})Py$ is related to the different surface/volume ratio for the two batches.
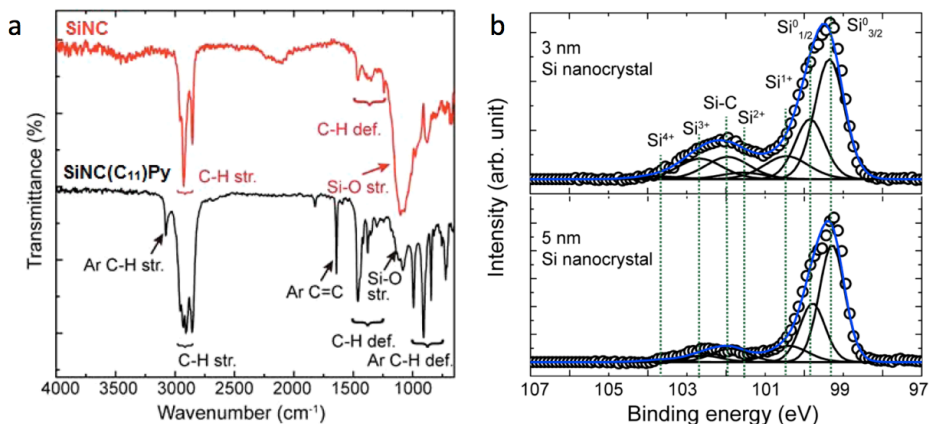
Figure 1.15: *a)* Comparison betweeen FT-IR spectrum of of 3 nm diameter $SiNC(C_{II})Py$ and SiNC; *b)* XPS spectra of Si° signal registered for 3 nm and 5 nm $SiNC(C_{II})Py$ samples.

Finally, the photophysics of the prepared samples was evaluated in toluene solution. The first samples to be analysed were the reference 3 nm and 5 nm SiNCs. Figure 1.16 is shownig the absorption spectra of 3 nm and 5 nm samples as a continuous line. It can be noticed that no peak is observed, but an unstructured band is increasing in the UV region with a scattering like behaviour, proving the indirect band gap nature of the nanocrystals. The y-axis is representing the molar absorption coefficient ε, that was obtained by dividing the absorbance value at each λ with the concentration of the SiNCs solution, following the Lambert-beer equation $A = \varepsilon\, b\, [SiNCs]$ with an optical path equal to 1 cm. The concentration of the sample has been calculated by dividing the Absorbance at $\lambda_{abs} = 400 nm$ with the corresponding molar absorption coefficient previously reported by Hessel at al.,[20] equal to $\varepsilon_{400} = 5\, x\, 10^4 M^{-1} cm^{-1}$ for the 3 nm sample and $\varepsilon_{400} = 5.3\, x\, 10^5 M^{-1} cm^{-1}$ for the 5 nm one.

The dashed lines in the same graph represents the emission spectrum taken on the same two samples. The emission band is unstructured and it is characterized by a Gaussian-like shape with a maximum of intensity at about $\lambda_{em} = 660$ nm for the 3 nm SiNCs and $\lambda_{em} =$
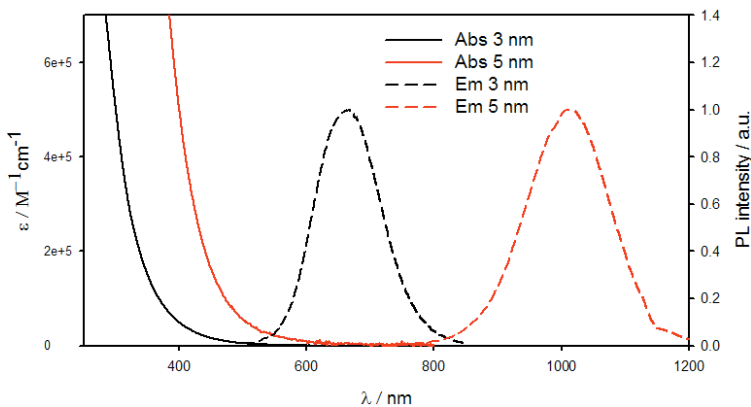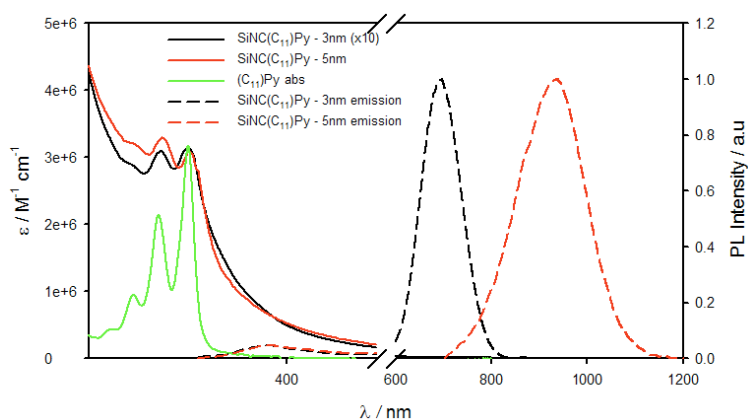
Figure 1.16: Molar absorption coefficient (continuous line) and normalised emission spectra (dashed line, $\lambda_{exc} = 420\,nm$) of 3 and 5 nm SiNCs toluene solutions at RT.

1000 nm for the 5 nm SiNCs. The photoluminescence quantum yield was measured with a relative method described in Appendix A, giving a quite different value for the two samples; 3 nm SiNCs are indeed characterized by a $\phi_{PL} = 0.16$ whereas the 5 nm are showing a much higher $\phi_{PL} = 0.45$. As described in the first section of this chapter, the size-dependent ϕ_{PL} is a commonly observed property for alkyl-passivated SiNCs and it is mainly attributed to the higher concentration of surface defects in small Si clusters. Due to time constraints, the ϕ_{PL} for the 3 nm values were obtained with no correction for the detector response, so the absolute value is not completely reliable, even if it is still useful for a comparative purpose between samples. A more correct and complete evaluation of the ϕ_{PL} with the absolute method will be discussed in the last section of Chapter 2.

The luminescence lifetimes are also following the behaviour already described in section 1.1 for the radiative lifetime dependence on the size of silicon nanocrystals, which value was simulated to be decreasing upon increasing the size of the nanocrystal due to an increasing radiative recombination rate. The luminescence lifetimes observed for SiNCs samples were observed to be strongly depending on the choice of λ_{em} chosen for the acquisition and on the precise size distribution of the sample, therefore a quantitative comparison is not straightforward between different batches of nanocrystals. Nevertheless, by choosing fixed emission slits and centering the acquisition on the maximum of the Gaussian-like emission band the lifetime observed for the 3 nm SiNCs was equal to 70 μs while for the 5 nm SiNCs a bigger

$\tau_{PL} = 150\,\mu s$ was registered. The absence of short-lived fluorescent states confirmed the good degree of functionalization and the absence of luminescent surface defects.[72]

Moving to the pyrene functionalized SiNCs, we performed the same photophysical characterization to understand the new features of the hybrid material and if the typical properties of the silicon core were preserved after the functionalization. Figure 1.17 is showing the typical absorption and emission spectra of 3 nm and 5 nm sized $SiNC(C_{11})Py$. The addition of the pyrene moiety has given rise to a new structured band with two peak maxima at $\lambda_{abs} = 330nm$ and 345 nm, related to the pyrene unity. Please notice that, for comparison purposes, the molar absorption coefficient of 3 nm has been multiplied by a 10x factor, in order to better appreciate the shape of the aforementioned band. From the comparison with the absorption spectrum of the free pyrene ligand (green continuous line), it is clear that, once coupled to the SiNC surface, the pyrene absorption band is broadened, therefore an interaction between the pyrene moiety and the silicon core is occurring.

Figure 1.17: Molar absorption coefficient (black and red continuous line) and normalised emission spectra (black and red dashed line, $\lambda_{exc} = 420nm$) of 3 and 5 nm $SiNC(C_{11})Py$ toluene solutions at RT. 1-((undec-10-enyloxy)methyl)pyrene absorption was added for comparison (green continuous line).

The emission spectra, registered in the same conditions used for the SiNCs samples, show similar gaussian-like emission bands, with a maximum intensity centered at about 690 nm for the 3 nm $SiNC(C_{11})Py$ and about 1000 nm for the 5 nm $SiNC(C_{11})Py$. It must be noted that, if exciting the sample at $\lambda_{abs} = 345$ nm, where the pyrene ligand absorbs, a slight band cen-

tered at $\lambda_{em} = 400$ nm arises, corresponding to pyrene fluorescence. The photoluminescence quantum yield, taking into account the Si core emission, is not significantly affected by the functionalization, respectively $\phi_{3nmPL} = 0.13$ for 3 nm SiNC(C_{11})Py and $\phi_{3nmPL} = 0.42$ for 5 nm SiNC(C_{11})Py.

Also the luminescence lifetimes for the SiNC(C_{11})Py samples is not strongly differing from the one observed for the control SiNCs.

As we will see in the next section, this is not true for the emission of the pyrene moiety, which is strongly affected by the energy transfer processes (ET) towards the silicon core. The first evidence for the ET occurring occurred during the evaluation of the fluorescence lifetime of the pyrene moiety once coupled to the silicon surface. Indeed, as shown by figure 1.18, the fluorescence lifetime of the pyrene unity ($\lambda_{exc} = 345$ nm, $\lambda_{em} = 400$ nm) moved from a monoexponential value equal to $\tau_{PL} = 18$ ns to a multiexponential decay, the fitting of which is not possible with a sufficient degree of accuracy. Nevertheless, the best fitting was obtained by considering a bi-exponential function with characteriztic lifetimes $\tau_{1PL} = 2.0$ ns and $\tau_{2PL} = 11.0$ ns. These values are differing from the free pyrene lifetime, consistent to an efficient quenching of the pyrene emission. Nevertheless, the multiple lifetime might be a clue that the pyrene moieties are experiencing different conditions, probably due to the vibrational and rotational movements of the alkylic chain or a different degree of functionalization influencing the intermolecular interactions.
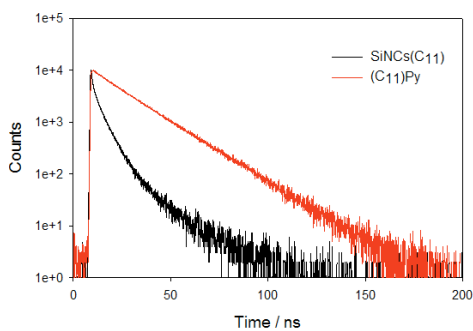
Figure 1.18: Photoluminescence lifetime of SiNC(C_{11})Py compared to the free ligand (C_{11})Py in toluene solution at RT ($\lambda_{exc} = 345$ nm, $\lambda_{em} = 400$ nm).

Similar behaviour was observed for SiNC(C_3)Py samples, but in order not to be redundant,

Table 1.1: Optical properties of SiNC, SiNC(C$_{11}$)Py and SiNC(C$_3$)Py.

Sample	Diameter (nm)	λ_{exc} (nm)	λ_{PL} (nm)	ϕ_{PL}	τ_{PL} (ns)
PYRENE LIGAND					
$C_{11}Py$		345	400	0.06	18
C_3Py		345	400	0.06	18
SINCS 3 NM					
$SiNC$	3	420	635	0.16	70 x 10^3
$SiNC(C_{11})Py$	3	345	400	0.006	2.0, 11
	3	420	700	0.13	90 x 10^3
$SiNC(C_3)Py$	3	345	400	0.005	0.2, 5
	3	420	690	0.11	95 x 10^3
SINCS 5 NM					
$SiNC$	5	420	970	0.45	150 x 10^3
$SiNC(C_{11})Py$	5	345	400	0.006	3.2, 12
	5	420	940	0.42	160 x 10^3
$SiNC(C_3)Py$	5	345	400	0.005	0.2, 5
	5	420	970	0.40	190 x 10^3

these datas can be found in Table 1.1, where all the previously discussed datas are collected.

1.3.4 Energy transfer efficiency evaluation

As JUST SUGGESTED in the previous section, the first evidence of ET was observed by comparing the fluorescence lifetimes of the pyrene moiety with the one of a free pyrene ligand. Both SiNC(C$_{11}$)Py and SiNC(C$_3$)Py show a decrease of the fluorescence lifetime of the photoactive molecule due to the introduction of a new non-radiative decay path while the ligands are coupled to the surface of the nanocrystal. The magnitude of the quenching efficiency is hard to extract from the lifetimes variation because there are two distinct lifetimes observed in both SiNC(C$_{11}$)Py and SiNC(C$_3$)Py (Table 1.1), which probably correspond to different degrees of interaction with the silicon core. In any case, the absence of a τ_{PL} = 18.0 ns in the functionalised samples proves the absence of free pyrene solution after the samples purification procedure.

The evaluation of the energy transfer efficiency was therefore carried out preparing two

solutions of SiNC(C$_{II}$)Py and SiNC, optically matching at λ_{abs} = 400 nm, respectively red and blue spectra in Fig 1.19 a) (3 nm samples) and Fig 1.19 c) (5 nm samples). The concentration of nanocrystals was calculated by dividing the absorbance value for the already described molar absorption coefficient. A certain amount of free ligand $(C_{II})Py$ was added to SiNCs until the solutions were characterized by the same absorbance at 345 nm, in order to precisely compare the photophysics of the functionalized system and the untied one in the same exact condition of solvent, concentration and amount of light absorbed by each component.

This comparison is also useful to understand how many units of photoactive ligands are effectively conjugated to the SiNCs. Indeed, the molar absorption coefficient of the pyrene derivative is ε_{345nm} = 4.4 x 10^4 M^{-1} cm^{-1}, so by subtracting to the overall absorption of the mixed SiNC + $(C_{II})Py$ (called henceforward SiNC mix) the contribution of SiNC, and dividing the absorbance at λ_{abs} = 345 nm for the $(C_{II})Py$ ε_{345nm}, we are also able to get the concentration of the pyrene ligand. The ratio between the ligand concentration and the SiNC concentration in the mixed solution can be considered as consistent to the number of ligands for nanocrystal in SiNC(C$_{II}$)Py samples, because no variation on the molar absorption of both the nanocrystals and the ligand are expected after the covalent functionalisation.

Therefore, the number of $(C_{II})Py$ units for nanocrystals in SiNC(C$_{II}$)Py was estimated to be 3.5 for the 3 nm sample and about 50 for the 5 nm one. This is consistent with the difference of surface are between the smaller and the bigger nanocrystals, which should allow a more efficient funcionalization reaction.

The energy transfer efficiency can be evaluated by considering either the efficiency of the photoluminescence quenching of the donor specie η_q, in our case the pyrene moiety, or the increment of the acceptor photoluminescence, i.e. the Si core, defined as the sensitization efficiency η_s. If these two values are equivalent, the only intermolecular non-radiative process occurring is an energy transfer, because the energy subtracted to the photoluminescence of the donor, corresponding to η_q, is completely transferred to the excited state of the acceptor, with no further decay path other than the radiative one.

In our system, the quenching efficiency is calculated by comparing the integral of the emission intensity of SiNC(C$_{II}$)Py sample (red line fig. 1.19 b and d) exciting at λ_{abs} = 345 nm, with the one obtained for the SiNC mix sample (green line fig. 1.19 b and d) in the same wavelength
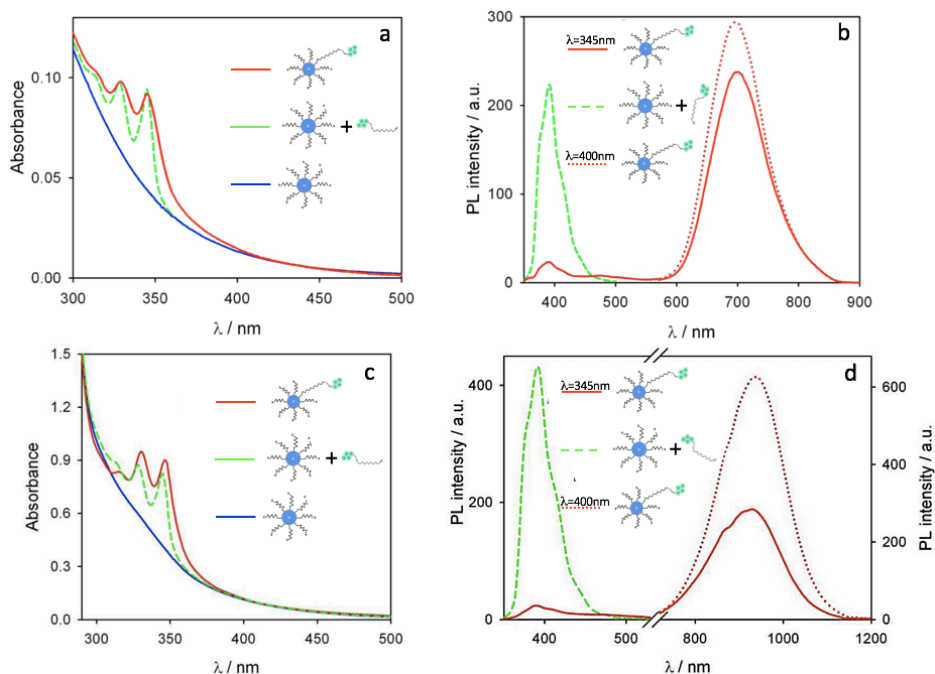
Figure 1.19: Absorption of 3 nm diameter a) and c) 5 nm diameter SiNCs (blue line), SiNC(C_{II})Py (solid red line) and a mixture of SiNCs and (C_{II})Py (green dashed line) in the proper ratio to obtained and optically matched solutions at $\lambda_{exc} = 345$ nm with respect to SiNC(C_{II})Py samples. Photoluminescence spectra of b) 3 and (d) 5 nm diameter SiNC(C_{II})Py (solid red line, $\lambda_{exc} = 345$ nm; dashed red line, $\lambda_{exc} = 400$ nm) and the optically matched solutions of free (C_{II})Py mixed with SiNCs in the appropriate ratio (green dashed lines, $\lambda_{exc} = 345$ nm) in air-equilibrated toluene. To obtain the PL spectra in b) and d), the two samples of SiNC(C_{II})Py photoexcited at 345 and 400 nm are optically matched at the excitation wavelength to enable direct comparison of the emission intensity of the SiNCs when light absorption is dominated by the pyrene moieties or the nanocrystals. In d), the y-axis on the left corresponds to the pyrene-related emission, and the y-axis on the right corresponds to the SiNC-related emission.

Table 1.2: Number of ligands per SiNC and Energy transfer efficiency for SiNC(C$_{11}$)Py and SiNC(C$_3$)Py.

Sample	Size (nm)	Number of Py unit per SiNC	η_q	η_s
		SiNCs 3 NM		
$SiNC(C_{11})Py$	3	3.5	90	70
$SiNC(C_3)Py$	3	6	>95%	>95%
		SiNCs 5 NM		
$SiNC(C_{11})Py$	5	50	90	30
$SiNC(C_3)Py$	5	60	>90%	65

interval. The quenching efficiency is defined as follows:

$$\eta_q = 1 - \frac{I_{SiNC(C_{11})Py}}{I_{SiNCmix}} \tag{1.5}$$

The sensitization efficiency, conversely, is calculated by comparing the Si core luminescence in SiNC(C$_{11}$)Py sample with the one of SiNC mix sample always exciting at $\lambda_{abs} = 345$ nm, corresponding to the 0% of sensitization (I$_0$). This value has to be normalised on the 100% of theoretical efficiency, that is measured by preparing a third solution of concentrated SiNC(C$_{11}$)Py, which absorbance value at $\lambda_{abs} = 400$ nm (where only SiNCs absorb) matches the one of the diluted SiNC(C$_{11}$)Py sample at $\lambda_{abs} = 345$ nm. The luminescence of this solution exciting at $\lambda_{exc} = 400$ nm is called I$_{100}$ (dashed red line fig. 1.19 b and d) and it is put in relation with the sensitization efficiency with this equation:

$$\eta_s = \frac{I_{SiNC(C_{11})Py} - I_{100}}{I_{100} - I_0} \tag{1.6}$$

The same analysis was performed on SiNC(C$_3$)Py samples, obtaining the set of spectra displayed in Figure 1.20.

The results about the calculated number of pyrene units, the quenching efficiency and the sensitization efficiency for both SiNC(C$_{11}$)Py and SiNC(C$_3$)Py samples are summarized in table 1.2:

What is immediately apparent from this table, is the difference in sensitization efficiency be-
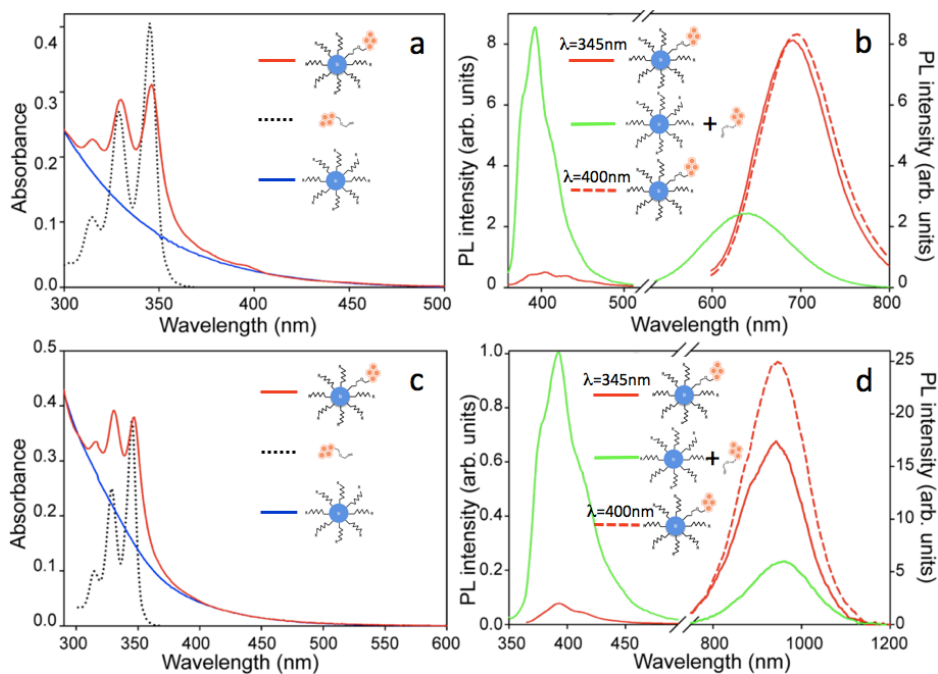
Figure 1.20: Absorbance spectra of a) 3 nm and c) 5 nm diameter SiNCs (blue), SiNC(C$_3$)Py (red line), and (C$_3$)Py (black dotted line) in air-equilibrated toluene at RT. Photoluminescence spectra of b) 3 and (d) 5 nm diameter SiNC(C$_3$)Py (solid red line, $\lambda_{exc} = 345$ nm; dashed red line, $\lambda_{exc} = 378$ nm) and optically matched solutions of free Py mixed with SiNCs in the appropriate ratio (green lines, $\lambda_{exc} = 345$ nm) in air-equilibrated toluene. To obtain the PL spectra in b) and d), the two samples of SiNC-Py photoexcited at 345 and 378 nm are optically matched at the excitation wavelength to enable direct comparison of the emission intensity of the SiNCs when light absorption is dominated by the pyrene moieties or the nanocrystals. In b) and d), the y-axis on the left corresponds to the pyrene-related emission, and the y-axis on the right corresponds to the SiNC-related emission.

tween $SiNC(C_{11})Py$ and $SiNC(C_3)Py$ samples. Indeed, the η_s is decreasing from the overn 95% value for the $SiNC(C_3)Py$ 3 nm to the 70% of the $SiNC(C_{11})Py$ 3 nm. The same behaviour is observed for the 5 nm samples, where the η_s is already lower for the $SiNC(C_3)Py$ 5 nm with respect to the 3 nm sample shifting from 95% to 65%, but this value is further decreasing when compared with the $SiNC(C_{11})Py$ 5 nm, which η_s is about 30%. On the opposite, the η_q value is almost unitary for almost every pyrene functionalized sample, independently neither from the length of the alkylic tether, nor from the size of the nanocrystal. While for the 3 nm $SiNC(C_3)Py$ samples this value is consistent with the η_s, meaning that the only quenching process occurring is the energy transfer to the Si core, the 3 nm $SiNC(C_{11})Py$ is showing a strong difference between η_q and η_s, revealing that a further non-radiative process must take place. This process has found to be related to the formation of pyrene excimers, which are prevented in the case of the shorter bridge since the pyrene chromophores are embedded in the dodecyl chains. The formation of pyrene excimer deactivates the fluorescent excited state of pyrene, yielding a competitive pathway with respect to energy transfer to the silicon core. The formation of pyrene excimers is proved by the rising of the typical[73] broad and unstructured band centered at 480 nm, as shown in figure 1.21. Tethers that are long enough for the pyrene
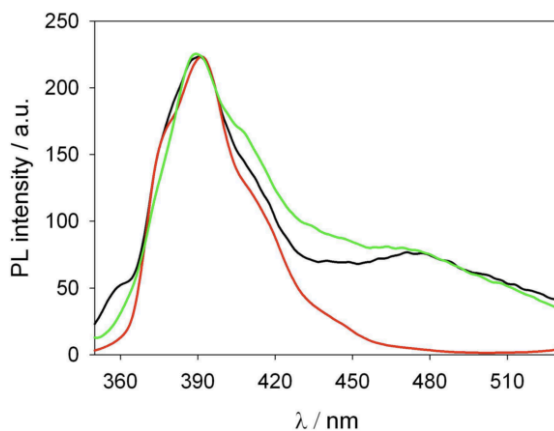
Figure 1.21: Normalized emission spectra of of the pyrene ligand in $SiNC(C_3)Py$ sample (red line, emission slits = 3 nm) and $SiNC(C_{11})Py$ sample (emission slits = 3 nm, black line; emission slits = 5 nm, green line) in toluene solution at room temperature. $\lambda_{exc} = 345nm$.

to extend beyond the capping ligand layer into the surrounding solution enable association with molecules and substrates in the surroundings. This is a major issue if we are interested in

the behaviour of these nanocrystals in presence of interacting species in solution, which will be part of the subject of the next chapter.

1.3.5   Conclusions

From this analysis two conclusions are outstanding: First, the sensitization efficiency is affected by the size of the nanocrystal, with an average decrease of 35% by increasing the size of the silicon core from 3 nm to 5 nm. This could be induced by several factors, which we cannot distinguish in this study, such as the different surface morphology, the presence of defects or a different surface coverage degree that is allowing more or less freedom to ligand motion. It must be noted, anyway, that the lower energy transfer efficiency for the 5nm SiNCs is compensated by the higher number of pyrene unity per nanocrystal, resulting in higher overall amount of energy absorbed and transferred to the SiNC. This is also meaning an increasing of the brightness of the nanocrystals, defined in this case as the product between the molar absorption coefficient, the photoluminescence quantum yield and the sensitization efficiency.

The second inference we can draw is related to the length of the alkylic chain acting as a spacer between the Si core and the pyrene moiety. The decreasing η_s upon increasing the length of an alkylic chain has been assessed both for the 3 nm and the 5 nm nanocrystals, proving that the pyrene moiety is effectively coupled to the nanocrystal and it is possible to tune the interaction altering the distance between donor and acceptor.

"When someone seeks," said Siddhartha, "then it easily happens that his eyes see only the thing that he seeks, and he is able to find nothing, to take in nothing because he always thinks only about the thing he is seeking, because he has one goal, because he is obsessed with his goal. Seeking means: having a goal. But finding means: being free, being open, having no goal."

Herman Hesse, Siddhartha

2

Energy and electron extraction from silicon nanocrystals: towards the application in solar cells

UP TO NOW, the most efficient way to convert the energy provided by sunlight to electrical power is to exploit the photovoltaic effect in semiconductors. This effect involves the absorption of a photon by a semiconductor with a proper band gap, the subsequent formation of an electron-hole couple called exciton, and the splitting of the charges in opposite directions thanks to an electric field. Also in this field, silicon is the main character, due to the relatively low band gap and the high electron mobility, especially when doped with n-type or p-type impurities. The single crystal silicon based photovoltaics is still almost monopolizing the photovoltaics market, but alternative technologies are emerging due to higher efficiency, lower price and higher tunability. From a less technical point of view, the birth of cheap and less fragile photovoltaic cells is of the utmost importance to meet the always increasing need of

clean energy, in particular in emerging countries or the least developed ones.[74]

As proved in the first chapter, nanomaterials as quantum dots and nanocrystals have emerged as efficient light harvesting materials, in particular because of the stability of these system and the possibility to tailor the optical properties by controlling the morphology. In addition, the conversion efficiency of quantum dots based solar cells can overcome the traditional limit of 32% calculated by Shockley and Queisser for p-n junction Si solar cells.[75] The QD-based solar cells are summarized by Kamat[10] in three canonical architectures: metal-semiconductor or Schottky junction photovoltaic cell, (ii) polymer/semiconductor nanostructured solar cell, and (iii) quantum dots sensitized solar cell. The extraction of the photo-generated electron-hole pair in QDs and nanocrystals is the key step in all these devices, therefore a deep investigation of the intermolecular processes towards electron acceptors or donors is mandatory to optimize the performance of QD-based solar cells.

In this framework this chapter will be devoted to exploring different ways to exploit the energy collected by SiNCs through light harvesting.

In a first part of the chapter we report a series of studies we carried out on the intermolecular interaction of SiNCs with a particularly interesting class of materials such as carbon allotropes. The competition between electron transfer and energy transfer processes in the photophysical interaction will deeply investigated both by solution phase spectroscopy and different microscopy techniques.

By contrast, the second section of the chapter is focused on the exploitation of SiNCs luminescence in new generation photovoltaic devices. Indeed, the feasibility of two different photovoltaics architectures based on SiNCs will be discussed and the role of the nanocrystals will be investigated, showing extremely promising preliminary results.

2.1   Interaction with carbon allotropes

THE CHARGE EXTRACTION is probably the main bottleneck of most the quantum dots based solar cells. From Silicon technology, it is well known[76] that the presence of crystal domains edges is strongly limiting the efficiency of the cell because the electron mobility at the interface between domains is not high enough to overcome the charge recombination rate within the

single crystal domain. This issue becomes certainly greater when dealing with quantum dots, whose typical grain size is just a few nanometers. The capture of charge carriers at the surface of each quantum dot becomes then the key step in the enhancement of the solar cell efficiency. An interesting strategy to ensure a good transport of the photogenerated carriers consists in coupling quantum dots with carbon allotropes. This particular class of materials provides a wide library of optical, electronic and electrical properties, ranging from the electron acceptor characteristics of C_{60} fullerene, to the semiconductor nature of some single wall carbon nanotubes, or to the metal like behaviour of multi-wall carbon nanotube and graphene.

The capture of quantum dots photogenerated carriers by electron acceptors or donors should result in the quenching of the luminescence of the quantum dots and the decreasing of the photoluminescence lifetime. The ratio between the photoluminescence lifetime in presence/absence of the electron acceptor is therefore exploited to extract the rate of the electron transfer process from the sensitizing QD to the TiO_2 layer in QD sensitized solar cells, following this equation:

$$k_{et} = 1/\tau_{QD/TiO_2} - 1/\tau_{QD} \qquad (2.1)$$

This equation is not true when dealing with species able to quench the luminescence by means of different photophysical processes. For instance, the quenching of QD luminescence with fullerene derivatives, which is widely exploited in organic solar cells, cannot be directly related to the electron transfer kinetics because fullerene is characterized by a low energy triplet state that can interact with the sensitizer and induce an energy transfer process. Therefore it is mandatory to carefully study the photophysical interaction between each materials pair step by step, in order to obtain a deeper insight into the interaction mechanism.

In this section we report the investigation of the photophysical interaction between carbon allotropes and silicon nanocrystals, which has never been investigated before. The investigation has been performed on pyrene functionalized SiNCs, in particular SiNC(C_{11})Py. The choice of this batch of nanocrystals is due to possibility to enhance the interaction with carbon allotropes thanks to the pyrene moiety. Indeed, it is well-known that pyrene interacts strongly with carbon allotropes like carbon nanotubes and graphene by $\pi - \pi$ stacking[77].[78] The observation of the pyrene excimer formation described in Chapter 1 for the long-tether SiNC(C_{11})Py units indicates that the Py is exposed significantly to the surroundings. This means that the

tether is long enough to allow the Py units to extend away from the dodecene passivation layer into the solution, providing the possibility for Py interactions with other molecules and surfaces in the surrounding environment. This is not the case when the Py units are buried in the ligand passivation layer, as it happens for SiNC(C$_3$)Py samples, where no sign of excimer formation was observed.

Therefore, in order to study this photophysical interaction, we carried out a series of experiments exposing 3 nm SiNC(C$_{11}$)Py to C60, carbon nanotubes, and graphene.

2.1.1   C$_{60}$ Fullerene

Buckminster Fullerene (C_{60}) was added to a dispersion of 3 nm SiNC(C$_{11}$)Py in air-equilibrated toluene. The absorption spectra in figure 2.1 are the mere superposition of the spectra of SiNC(C$_{11}$)Py and of C_{60}, showing no evidence of ground-state interaction, otherwise resulting in the variation of the pyrene band or the formation of a new band.[79]
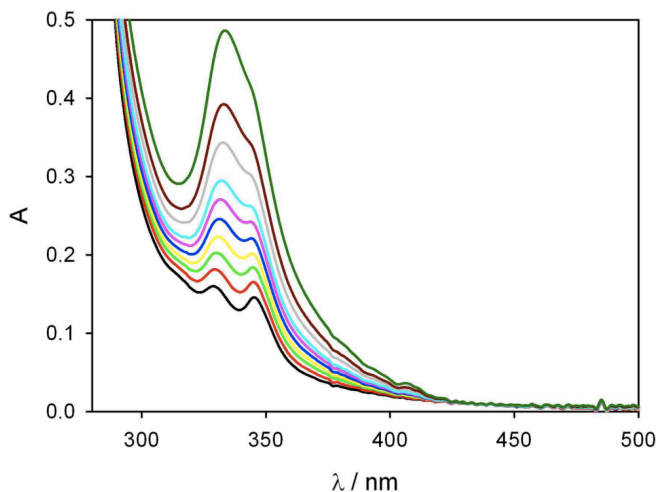
Figure 2.1: Spectrophotometric titration of 3 nm diameter SiNC(C$_{11}$)Py dispersed in air-equilibrated toluene (solid black line) with C_{60} (up to $7 \cdot 10^{-6}$ M)

Figure 2.2 a) shows the emission spectrum of SiNC(C$_{11}$)Py in presence of an increasing concentration of C_{60}. Photoexcitation at 345 nm induces predominantly pyrene light absorption,

but due to energy transfer, the PL spectrum is dominated by the Si nanocrystals band at 700 nm. The addition of C_{60} to $SiNC(C_{11})Py$ is inducing a quenching of the luminescence of both the pyrene fluorescence, centered at 400 nm, and the Si core luminescence.
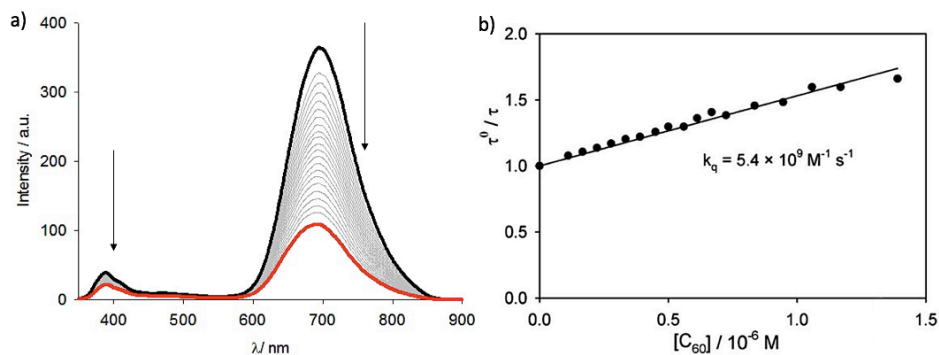
Figure 2.2: a) PL spectra of 3 nm $SiNC(C_{11})Py$ (λ_{ex} = 345 nm) upon addition of an increasing amount of a 2x10^{-3} M solution of C_{60} in dichloromethane. b) Stern-Volmer plot reporting the lifetimes of the Si core emission at 700 nm of $SiNC(C_{11})Py$ upon increasing the concentration of C_{60} (λ_{ex} = 345 nm).

Not only the PL intensity of the Si core was found to be decreasing upon increasing the concentration of C_{60}, but also the PL lifetime. Figure 2.2 b) shows the dependence of the PL lifetime of $SiNC(C_{11})Py$ on C_{60} (λ_{ex} = 345 nm, λ_{ex} = 700 nm). The PL lifetime value τ has been divided for the lifetime of $SiNC(C_{11})Py$ before the addition of C_{60} τ_0. The inverse of this ration has been plotted in order to fit the linear trend with the Stern-Volmer equation defined as follows:

$$\tau_0/\tau = 1 + k_q \tau_0 \left[C_{60} \right] \qquad (2.2)$$

This linear trend follows the one observed for the photoluminescence intensity for the Si core, therefore suggesting a dynamic quenching process resulting from the diffusive encounter of $SiNC(C_{11})Py$ and C_{60}, with no interaction in the ground state, in agreement with the spectrophotometric titration.

From the Stern-Volmer equation (eqn. 2.2), the quenching constant k_q can be evaluated: k_q = 5.4 x 10^9 M^{-1}s^{-1}, as reported in the inset of figure 2.2 b). This value is very high and close to the diffusion limit, therefore the quenching process is characterized by high efficiency.

In order to understand the mechanism behind this quenching, we tried to evaluate the occurrence of a photoinduced electron transfer between $SiNC(C_{II})Py$ and C_{60}. The C_{60}^- [80] is characterized by a fingerprint absorption band in the NIR region, centered at 1080 nm. The transient absorption spectra in the NIR region have been registered with the experimental setup described in Appendix A, in order to observe the rising of this band, but no signal for C_{60}^- was detected. It is worth noticing that the silicon nanocrystals have a transient absorption spectrum extending to the NIR, so we cannot completely exclude the formation of a small amount of C_{60}^- under our experimental conditions.

We then investigated the occurrence of an Energy Transfer process, which is theoretically possible due to the presence of a low energy triplet state of C_{60} partially overlapping with the emission band of $SiNC(C_{II})Py$. The sensitization of this C_{60} triplet excited state ($^3C_{60}$) has been studied by registering its transient absorption spectrum exciting the silicon nanocrystals. Unfortunately, the transient absorption spectrum of $^3C_{60}$ is characterized by a maximum at 730 nm [81], [82] which was found to be superimposed to the transient spectrum derived from the silicon nanocrystals, as evident by figure 2.3 a).
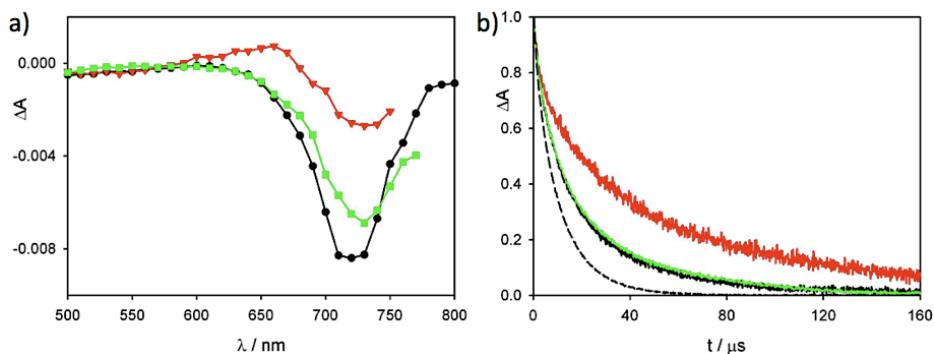
Figure 2.3: a) Transient absorption spectra of 3 nm $SiNC(C_{II})Py$ in degassed toluene in the absence (red line) and in the presence of C_{60} 1.5 x 10^{-5} M (black solid line) compared to a degassed toluene solution of C_{60} (again 1.5 x 10^{-5} M, green line) upon excitation at 532 nm. b) Normalized transient absorption decays at 735 nm of $SiNC(C_{II})Py$ in the absence (red line) and in the presence of C_{60} (black line) compared to C_{60} alone (green line). The emission intensity decay at 645 nm of $SiNC(C_{II})Py$ in the presence of C_{60} (black dashed line) is displayed for comparison purposes.

In order to circumvent the experimental limitation, we decided to probe the population of

sensitized $^3C_{60}$ by using an indirect method based on the evaluation of the sensitized emission from the lowest-energy singlet excited state of dioxigen $^1O_2$, naturally dissolved in solution. Indeed, it is known that $^3C_{60}$ sensitizes with unitary efficiency the population of $^1O_2$,[83] which, in its turn, radiatively deactivates with a PL maximum at 1270 nm. To do so, first of all we registered the spectrum in the NIR interval between 1220 and 1320 nm of the SiNC(C_{II})Py sample in air-equilibrated toluene, observing no evidence of the typical $^1O_2$ emission band. This means that SiNC(C_{II})Py, as well as SiNC, does not sensitize $^1O_2$ emission, in agreement with the lack of sensitivity to dioxygen of the emission quantum yields of the silicon nanocrystals that we observed during our experiments. Then we measured the PL signal in the same spectral interval generated by SiNC(C_{II})Py in presence of C_{60} (1.5 x 10^{-5} M) exciting at 420 nm, where light is selectively absorbed by the nanocrystals. This spectrum has been compared with the one registered for a C_{60} solution in toluene upon excitation at 330 nm for an optically matched solution at the excitation wavelength. The spectra have been normalized for the different emission intensity of the light source at different wavelength and the tail of the PL spectra of silicon nanocrystals has been subtracted in the sample containining SiNC(C_{II})Py. The resulting spectra, reported in figure 2.4, allowed us to calculate a sensitization efficiency for the energy transfer process from SiNC(C_{II})Py to $^3C_{60}$ equal to 40%. This value has to be compared with the quenching efficiency observed for the same solutions, which was calculated to be around 85%. This difference between quenching efficiency and sensitization efficiency is telling us that the energy transfer process is co-exhisting with a further bimolecular process, most probably an electron transfer.

2.1.2   Single Wall Carbon Nanotubes

THE QUENCHING EXPERIMENTS were performed also with single-walled carbon nanotubes (SWCNTs). In order to increase the solubility of the SWCNTs in apolar solvents we used a batch of SWCNTs functionalized with trimethyl(phenylethynyl)silane group, provided to us by Prof. Davide Bonifazi (Cardiff University), which should not interfere with the intermolecular interactions due to the poor reactivity and photochemistry. Upon addition of SWCNTs to a sample of 3 nm SiNC(C_{II})Py in air-equilibrated toluene, both the emission intensity of the silicon core at 700 nm and the one of the pyrene ligand at 400 nm decrease, as shown by figure 2.5 a). Please notice that the spectra have been corrected for the light absorbed and scattered
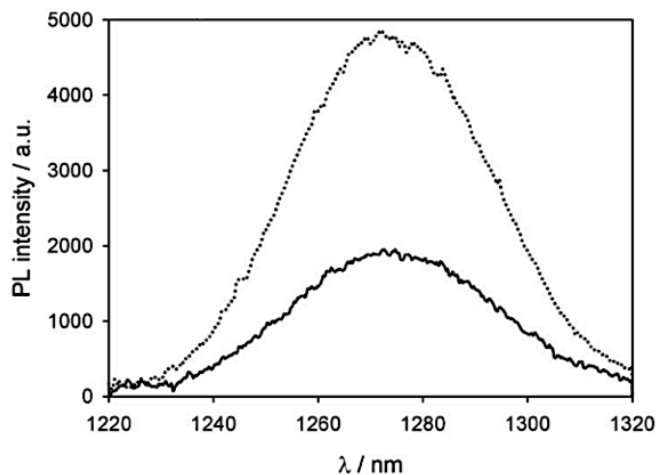
Figure 2.4: c) PL spectra of $^1O_2$ registered upon excitation at 420 nm of SiNC(C_{11})Py upon addition of C_{60} (1.5 x 10^{-5} M, solid line), compared to that of C_{60} (1.5 x 10^{-5} M, dotted line) in toluene upon excitation at 330 nm for optically matched solutions at the excitation wavelength. For comparison purposes, the tail of the PL spectra of silicon nanocrystals has been subtracted. ☐

by the SWCNT at the excitation wavelength, in order to obtain comparable spectra. As it was done with the quenching experiment with C_{60}, the relative variation of the PL intensity has been plotted against the concentration of SWCNT in the SiNC(C_{11})Py solution. Figure 2.5 b) shows the PL intensities variation of the pyrene ligand (390 nm), the pyrene excimer (470 nm) and the silicon core (700 nm), together with PL lifetime related to the Si core emission, which is not changing during the titration. This result is in line with a static quenching,[73] resulting from the ground state association of SiNC(C_{11})Py and SWCNTs thanks to $\pi - \pi$ stacking, as previously reported for pyrene and CNTs.[84]

In addition to this, it is worth noticing that the addition of SWCNTs causes quenching also of the pyrene emission, but the slope of the linear trend is differing from the one of the PL intensity related to the Si core, as well as from the one related to the variation of the pyrene excimer fluorescence. This result is indicative of an interaction of the pyrene unit with the carbon nanotube, creating a competitive path to the excimer formation. In particular, the excimer emission band at 470 nm is quenched with the same slope as the silicon nanocrystal emission, while the pyrene monomer emission band at 390 nm is quenched to a lower degree.
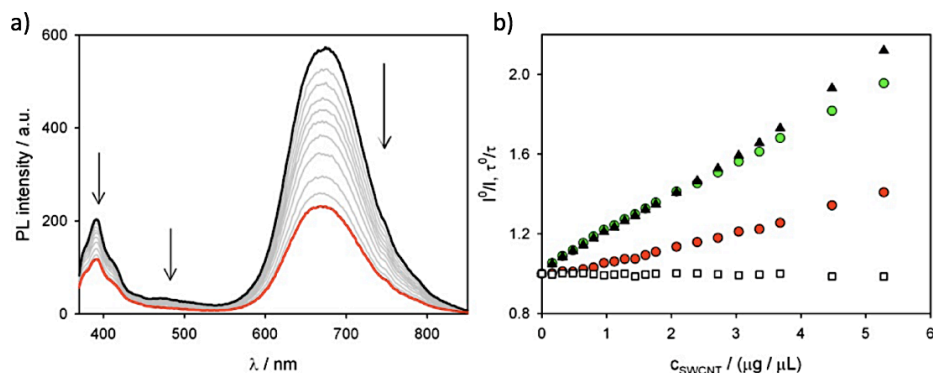
Figure 2.5: a) PL spectra of SiNC(C$_{II}$)Py (λ_{ex} = 345 nm) upon addition of an increasing amount of a 40 μg/mL solution of SWCNT in dichloromethane. b) Ratio of PL intensities at 390 nm (red circles), 470 nm (green circles), and 700 nm (black triangles), as well as silicon nanocrystals lifetimes (empty squares) in the absence (I_o, τ_o) and presence (I, τ) of increasing amounts of SWCNTs.

This experimental finding is consistent with the fact that two opposite mechanisms are active: the pyrene emission is quenched by an interaction with the carbon nanotube, but it is revived by the suppression of the excimer formation. Further confirmation of the ground-state interaction is provided by TEM analysis of the adduct formed by SWCNTs and SiNC(C$_{II}$)Py. Few drops of the sample containing SWCNTs and SiNC(C$_{II}$)Py after the quenching titration has been deposited on a Quantifoil R 2/1 carbon-film coated copper grid. The corresponding TEM and STEM-HAADF micrographs (appendix B for the instrumental details) shown in figure 2.6 highlight that the nanocrystals are preferentially located on the SWCNTs rather than on the supporting carbon film, proving the good interaction between the two components.

2.1.3 Graphene

THE INVESTIGATION of the photophysical interaction between SiNC(C$_{II}$)Py and graphene was not tested in solution phase, due to the lack of compatibility between the solubility of SiNC(C$_{II}$)Py and graphene. In particular, SiNC(C$_{II}$)Py have been shown to be soluble in highly apolar solvents, such as toluene, whereas the typical solvents used for the preparation of graphene dispersions are polar or slightly polar, as it will be described in Chapter 3. This resulted in the precipitation of either the nanocrystals or the dispersed graphene in any sol-
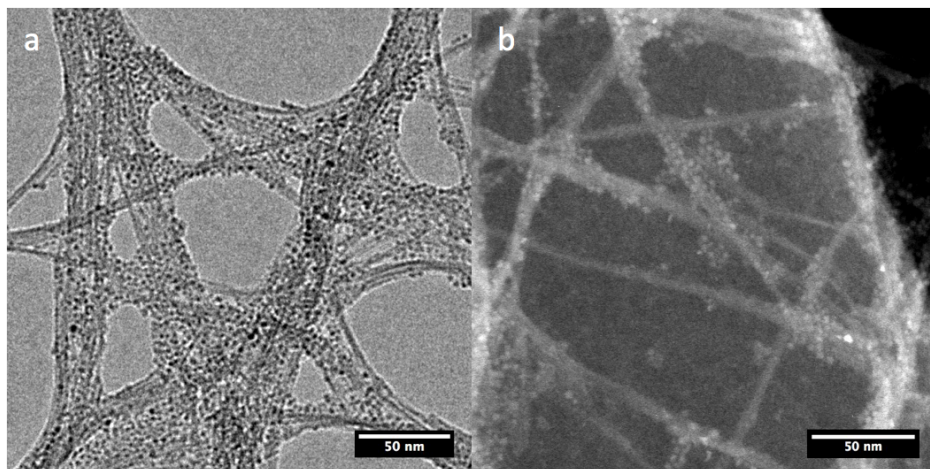
Figure 2.6: a) TEM micrograph and b) STEM-HAADF micrograph of SWCNTs coated by SiNC(C$_{II}$)Py.

vent mixture. Therefore, we studied the solid-state interaction with a graphene membrane prepared by chemical vapour deposition (CVD) with the following technique, adapted by Ortolani et al.:[85]

Graphene was growth on Copper foil (99.98% pure, 25 μm thick, Sigma-Aldrich) and CH$_4$ was used as feedstock in reducing atmosphere. After being cleaned with acetic acid, the foil was insterted in the CVD furnace and annealed under hydorgen flow at 1000°C, then the copper foil was exposed to a methane/hydrogen mixture for 1h, in order to completely cover the foil with the carbon film. Transfer onto other substrates was achieved by spin coating PMMA on graphene surface and mechanically removing the graphene membrane growth on the back of the copper foil. The copper layer was then etched by dipping it in a HNO$_3$ solution (33%wt in deionized water) and the resulting graphene/PMMA membrane was transferred onto the desired substrate after washing it several times with deionized water. PMMA was removed by dipping the sample in cold acetone, followed by hot acetone and isopropanol to complete remove any residual of PMMA. The thickness of the graphene produced was between 1-4 layers.

In order to study how the nanocrystals are arranging on the surface of graphene, we deposited a CVD graphene membrane on Quantifoil R2/1 carbon film coated copper grids. The
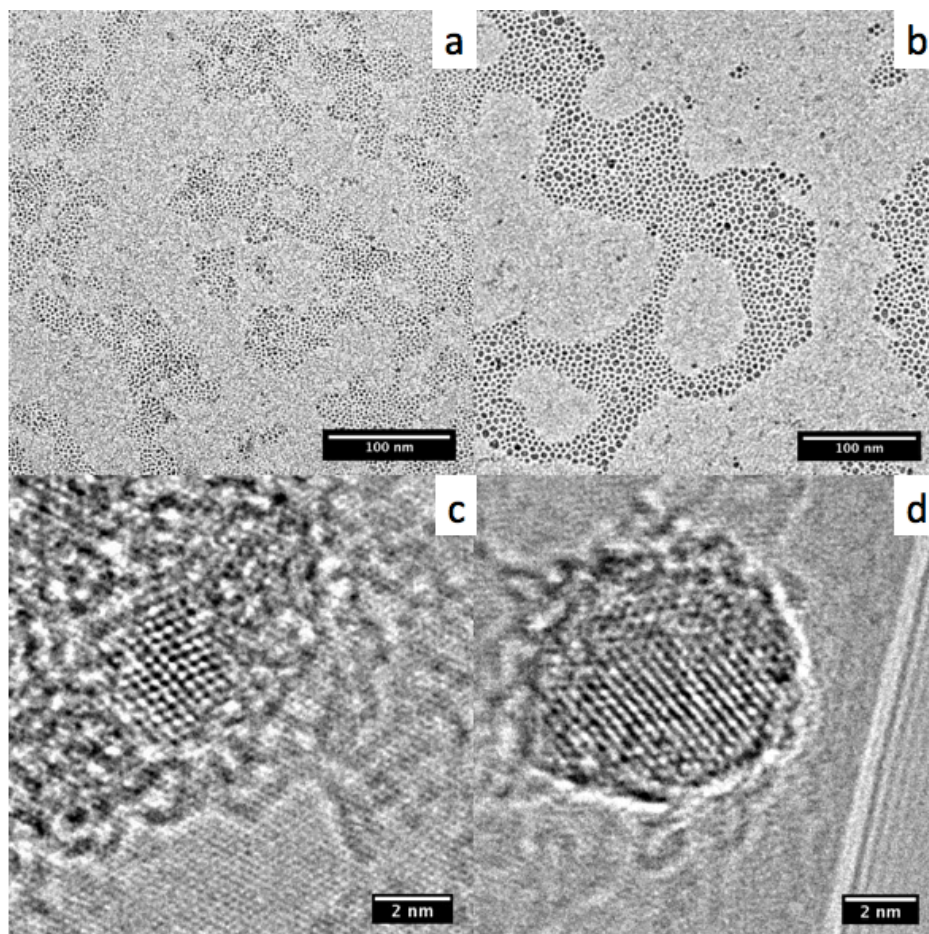
Figure 2.7: Low-magnification TEM micrographs of 3 nm a) and 5 nm b) SiNC(C$_{\text{II}}$)Py deposited on a CVD graphene coated TEM grid. c, d) High-magnification HR-TEM images of respectively 3 nm and 5 nm nanocrystals supported on graphene, showing the Si(1,1,1) lattice fringes at 0.31 nm.

grids have been dipped for 1h either in a 3 nm or 5 nm SiNC(C_{11})Py, then they have been washed with acetone to remove the solvent residuals and dried under vacuum. The nanocrystals (figure 2.7) form a uniformly dispersed monolayer of nanoparticles, without the formation of thick aggregates both for the 3 nm and the 5 nm sized nanocrystals. The very low thickness of the graphene film, between one and three layers, allowed us to obtain a deeper insight into the crystalline structure of the nanoparticles, by enhancing the contrast for a light element such as silicon, as previously reported by Panthani et al. [86]

To test the photophysical interaction, a 2 cm² CVD graphene membrane has been deposited on a 2x3 cm quartz slide, covering the central part of the slide. The slide has been dipped in a 3 nm SiNC(C_{11})Py solution and washed with acetone as described before for the TEM grid, then the nanocrystals were mechanically removed by the back of the slide. A control experiment depositing 5 nm SiNC(C_{11})Py on a Si/SiO$_2$ wafer with the same technique was performed, in order to check that the concentration of nanocrystals was comparable between the area covered by the graphene membrane and the residual SiO$_2$ substrate. The choice of the Si/SiO$_2$ substrate instead of a quartz one was induced by the need of a conductive substrate for the SEM characterization (figure 2.8, appendix B for the instrumental details), but we could assume that the deposition of the nanocrystals was comparable on the two SiO$_2$ surfaces.
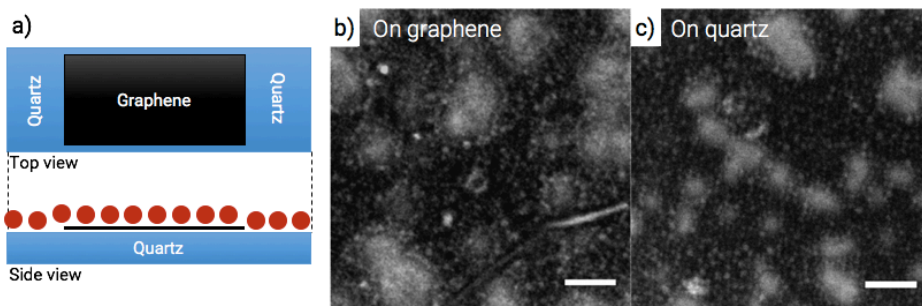
Figure 2.8: a) schematic representation of the graphene covered quartz slide and the deposited nanocrystals. SEM micrographs of the SiNCs deposited onto the graphene coated area of the Si/SiO2 wafer b), with a visible graphene wrinkle, and c) outside the graphene area, on the pristine SiO$_2$ layer. The nanocrystals are forming a continuous and equally distributed layer (darker areas). Scale bar equal to 50 nm.

The PL of the SiNCs deposited on the graphene coated quartz slide was measured on a con-

ventional spectrofluorimeter with a 45° setup, covering the edge of the quartz slide to remove the PL signal due to the waveguided luminescence. The comparison between the PL spectrum exciting the graphene covered area and the quartz area are reported in figure 2.9 a. The emission intensity on the graphene covered area is strongly lower than the one observed on the quartz surface. The luminescence lifetimes registered on quartz and graphene are similar, as expected for a static quenching.
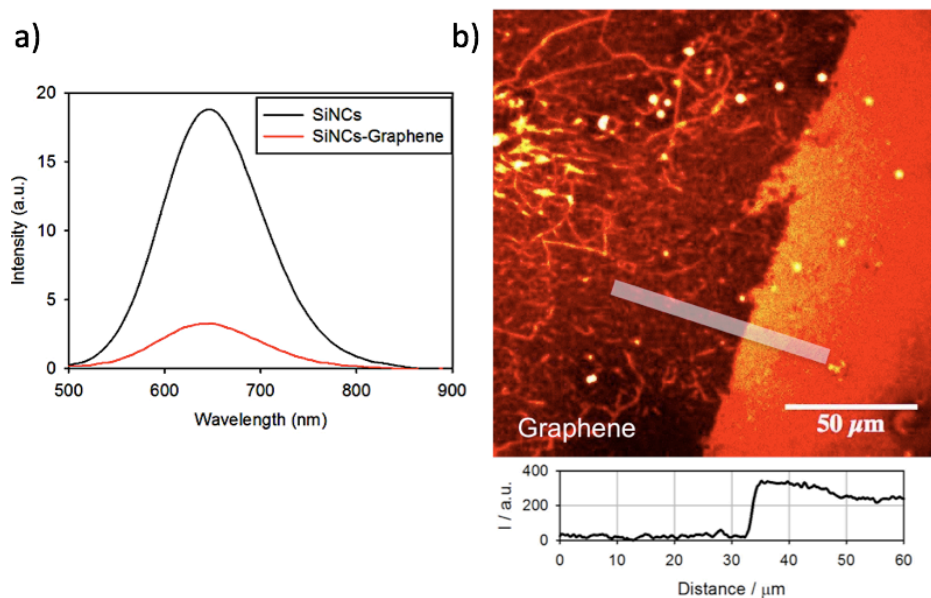
Figure 2.9: a) PL spectra of the 3 nm SiNC(C$_{11}$)Py deposited on the CVD graphene coated quartz slide exciting either on graphene surface or on the quartz area. b) Wide-field luminescence microscope image of SiNC(C$_{11}$)Py (3 nm diameter) deposited on quartz and graphene- coated quartz. The image shows the graphene film edge. In the low inset it is reported the emission intensity profile registered by wide-field luminescence microscopy along the white line in panel b).

We then measured the microscopic variation of the PL signal at the graphene film edge by observing the sample at the wide-field fluorescence microscope (details on the instrumental setup are reported in Appendix A). Figure 2.9 b) shows the wide-field fluorescence image of one of the graphene edges. Considering that (i) the concentration of SiNCs was observed to be comparable on the whole sample and (ii) the absorption of graphene is negligible (lower than 5% as observed by previous transmission measurements); the different emission intensity

registered on quartz and graphene has to be ascribed to a quenching mechanism. Please notice that the luminescent stripes on the graphene covered area are likely to be due to breaks in the graphene films, previously observed on transferred graphene samples.

The variation of the PL intensity is also more evident by plotting the emission intensity profile registered by wide-field luminescence microscopy along the white line, which is characterized by a sharp step corresponding to the graphene membrane edge.

2.1.4 Interaction with graphene: photoinduced charge transfer investigation by Kelvin Probe Microscopy

To ASSES IF a charge transfer is responsible for the quenching of SiNCs on CVD graphene surface, we performed Kelvin Probe Microscopy (KPM) experiments. KPM is a particular kind of a scanning probe technique based on the instrumental setup of a conventional Atomic Force Microscope (AFM) (further details reported in Appendix B). This technique is able to measure the Contact Potential Difference (CPD) between the AFM tip and a conductive sample, defined as follows:

$$V_{CPD} = \frac{\phi_{tip} - \phi_{sample}}{-e} \tag{2.3}$$

Where ϕ_{tip} and ϕ_{tip} are respectively the work function of the tip and the sample and e is the electronic charge. The KPM is a two-pass technique, meaning that the tip has to pass two times on the same point to acquire the CPD signal. The working mechanism of KPM is described by figure 2.10. Basically, when the tip is passing for the first time on the sample, an electric field is generated due to the difference in the Fermi energy levels. When the distance between tip and sample is short enough, the Fermi levels equilibrate and both of them become charged. The vacuum energy are no more aligned, and the the potential generated is indeed the V_{CPD}. With the second pass, an external potential called V_{DC} is applied to restore the system neutrality; this value is measured and corresponds to the V_{CPD} with opposite direction.

This technique is able to recognize any variation in the work function of a material, with nm scale resolution. This means that charge transfer processes can be studied with spatial resolution in complex nanomaterials, such as the graphene/SiNCs composite we investigated in this section. KPM has already been extensively used as a tool for the characterization of
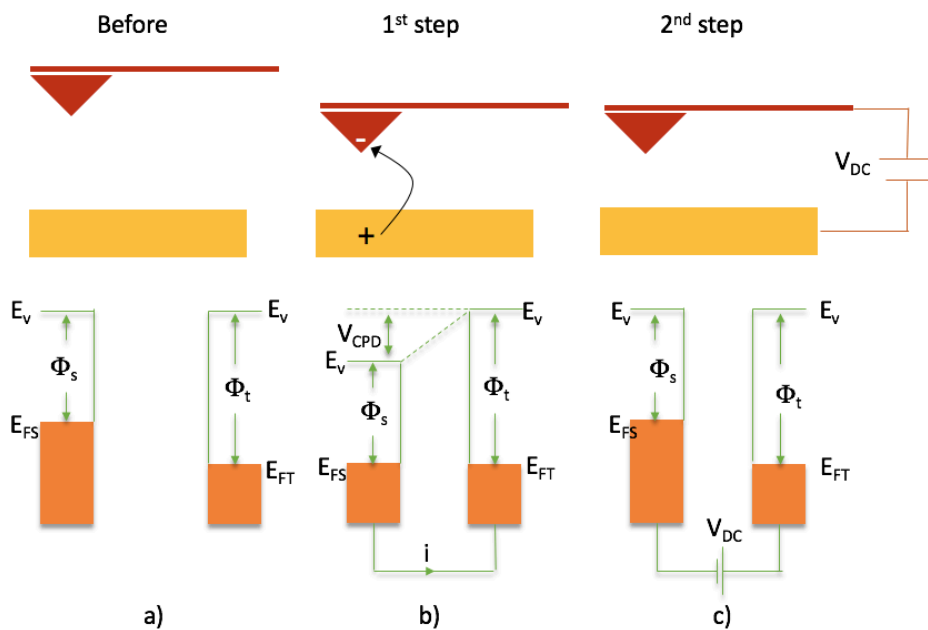
Figure 2.10: Schematic representation of the KPM working principle: a) tip and sample before electrical contact, with ϕ_S and ϕ_T corresponding to the work function of sample and tip; b) tip and sample with electrical contact and Fermi energy (E_{FS} for the sample E_{FT} for the tip); c) an external bias (V_{DC}) is applied to restore charge neutrality and bring bach the vacuum energy level (E_V)to the same value.

the electrical properties of p-n junctions and heterostructures, giving a deep insight on the the physics of photovoltaic cells. An interesting feature of KPM is the possibility to couple the instrument to a light source in order to study the photoinduced work function variation. However, very few examples of this application are reported, due to the intrinsic complexity of the technique. Indeed, due to the high sensibility of the technique, the extraction of the Fermi energy level is affected by many environmental factors, such as pressure, humidity, presence of adsorbates either on the sample or the tip. The degree of complexity is also increasing when characterizing nanomaterials, whose electrical properties and surface chemistry are often unknown. Nevertheless, the technique seems promising for a qualitative analysis of the photoinduced processes: for instance, the light induced charge transfer in a P3HT/CdSe-QDs blend has been studied with this setup,[87] observing a shift in the work function of the materials upon irradiating with an halogen white lamp. A similar approach was used to map the interface between a single nanorod heterojunction made of CdS-Cu_2ZnSnS_4,[88] exploiting the light excitation to recognize the different regions within a single nanorod.

In our system, we were interested in the the analysis of graphene/SiNCs interface, but, before that, we had to calibrate the instrumental setup to correlate work function and surface potential. First we measured the V_{CPD} between two different tips (Bruker SCM-PIT v2 Pt/Ir coating and MESP v2 Co/Cr coated tip) and freshly cleaved graphite, whose work function is known to be ϕ_{HOPG}=5.0 eV.[89] Applying equation 2.3 we obtained the work function of the two tips, respectively $\phi_{Pt/Ir}$=5.13 eV and $\phi_{Co/Cr}$=4.52eV; these values are differing of about 200mV from the ones tabulated for these tips, but the ratio between them is mantained, meaning that the difference in the measured work function is related to the conditions of the experiment (temperature, humidity, oxygen content). We then performed a control experiment depositing 5 nm SiNC(C_{11})Py on freshly cleaved HOPG graphite, which was used also as a reference for the CPD value. The resulting AFM and KPM images reported in figure 2.11 a) and b) are showing the formation of SiNCs islands on HOPG surface, with a similar pattern both for the topography and the CPD signal, as highlighted by shape of a profile traced on the same area of the AFM and KPM image (inset of figure 2.11 b). The average thickness of the SiNCs layer is equal to 5.7 nm, compatible with the size of the nanocrystals. The CPD measured on the HOPG area not covered by SiNCs was very close to the one observed for the reference HOPG sample with the same tip (Pt/Ir), equal to -130 mV, while the CPD measured on SiNCs islands was found to be about -80 mV; therefore the CPD difference between SiNCs

and the HOPG substrate is very small (only 50mV).
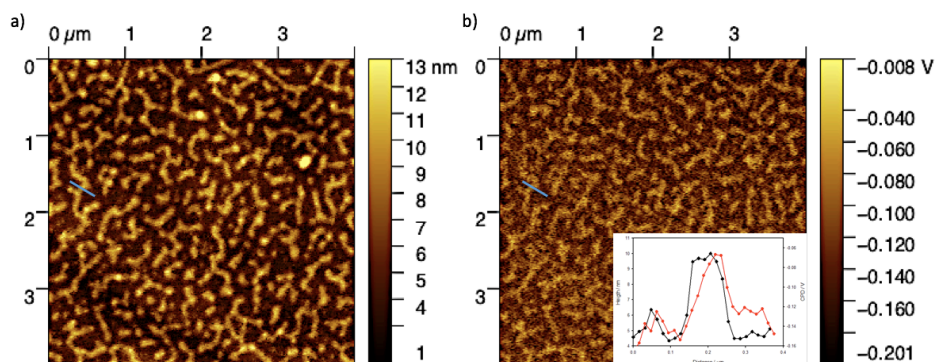
Figure 2.11: a) Topography and b) KPM image of the same area of a HOPG sample covered by 5 nm SiNcs showing the formation of SiNCs islands on the flat graphitic surface. In the inset the height and CPD profile on the same area of respectively image a) and b) showing a very similar trend.

We moved then to a CVD graphene sample, in order to obtain a reference value for the substrate work function, which we observed to be about 5.10 eV, slightly higher than the value previously observed for the HOPG (5.0 eV). By spin coating the 5 nm SiNC(C$_{11}$)Py sample on it, we observed the formation of SiNCs islands with the same thickness measured on HOPG but a slightly higher concentration (figure 2.12 a), probably due to the different roughness and wettability of the substrate. The KPM image (figure 2.12 b) is again characterized by the same pattern with respect to the topography, but this time a doping of the substrate was observed. Indeed, if comparing the V_{CPD} measured on the graphene areas (dark) in this sample with the one observed for pristine graphene, we could notice a shift from ∼70 mV to 20 mV. The reason of this shift, that was absent in the HOPG sample, can be attributed either to a charging of the graphene substrate due to a ground state charge transfer from SiNcs, or due to the lower concentration of SiNCs-free areas, averaging the graphene V_{CPD} with the one of SiNCs due to long-range electrostatic interaction forces between the cantilever, the tip, and the actual sample surface. Anyway, as observed for the HOPG sample, the V_{CPD} measured on SiNCs islands was higher than the one observed on graphene, around 65 mV, with a ΔV_{CPD} between graphene and SiNC equal to 40 mV, slightly lower than the 50 mV observed on the HOPG sample.

Finally we compared the behaviour of the sample in dark condition with the one under

Topography

Kelvin Probe

Dark

a)

16.3 nm
14.0
12.0
10.0
8.0
6.0
4.0
0.0

b)

0.146 V
0.120
0.100
0.080
0.060
0.040
0.020
0.000
−0.020
−0.061

Light

c)

9.1 nm
6.0
4.0
2.0
0.0
−2.0
−4.0
−6.0
−9.9

d)

0.125 V
0.100
0.080
0.060
0.040
0.020
0.000
−0.020
−0.040
−0.067
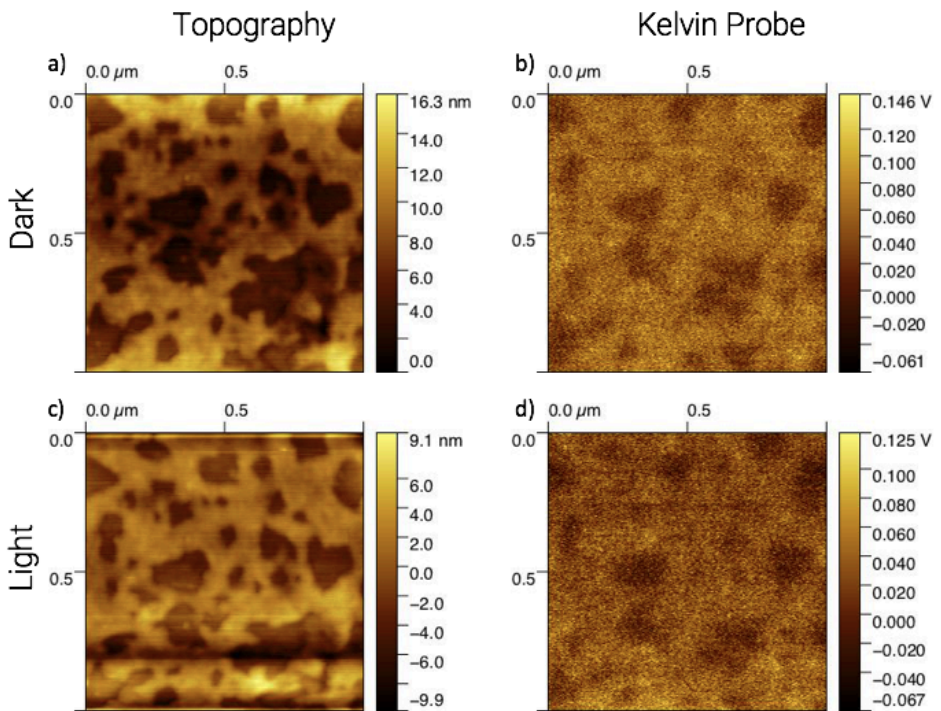
Figure 2.12: a) c) Topography and b) d) KPM image of the same area of a graphene coated quartz slide covered by 5 nm SiNcs either in dark or under illumination with a ($\lambda_{ex} = 400nm$).

illumination with a 400 nm LED (figure 2.12 c) and d). In order to perform the experiment we had to prepare a suitable stage for the sample able to shine the exciting light homogeneously on the sample. The scheme of the handmade stage is reported in figure 2.13 a).

A small drift in the topography image was observed upon illuminating the sample (figure 2.12 c), both in the y-axis and in the z-axis. The same behaviour was observed also for the KPM image (figure 2.12 d) and a more precise analysis can be made by observing the distribution of the V_{CPD} values in the sample before and during irradiation, reported in figure 2.13 b). The two hystograms are clearly characterized by a different maximum, due to an overall shift of the V_{CPD} both on graphene and on SiNCs surface. In contrast to this, no variation was observed on the FWHM of the two distributions ($\sim$40 mV for both of them), meaning that even if the average work function is changed upon irradiation the sample, the difference between the work function on graphene and on SiNCs is substantially the same. This might lead to the conclusion that no photoinduced charge transfer is producing any variation of the charge distribution on the sample. Unfortunately, due to the very small ΔV_{CPD}, we cannot completely exclude that any photoinduced charge transfer is taking place. Still, the photoinduced shift of the overall work function might be also interesting and it will be the subject of further investigation, in order to distinguish between the occurrence of a doping of the SiNCs/graphene hybrid, or a much less interesting thermal or light induced doping of the tip.
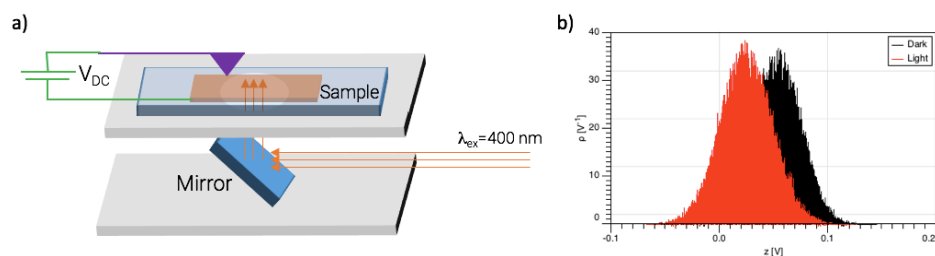
Figure 2.13: a) Schematic representation of the AFM stage for experiments under irradiation. Please notice that the sample must be transparent to ensure the correct excitation of the area of interest. b) V_{CPD} distribution for the sample shown in figure 2.12 in dark or light conditions.

2.2 Silicon nanocrystals in solar cells as luminescent species

IN THE SECOND SECTION of this chapter we will briefly resume the results we accomplished in the implementation of SiNCs in new generation photovoltaics. As highlighted in the previous section, the electron transfer processes in SiNCs are still far from being thoroughly understood, therefore the application as active materials will require further research work to be practicable.

Though these difficulties, SiNCs might represent an intriguing material for alternative photovoltaic devices thanks to their luminescence properties. Indeed, the high photoluminescence quantum yield and the absence of reabsorption due to the extremely high Stokes shift represent extremely interesting features for the two specific devices discussed in the next paragraphs, both based on the luminescence of a fluorophore to increase the power conversion efficiency of conventional solar cells.

2.2.1 Luminescent downshifting layer in DSSCs

DYE SENSITIZED SOLAR CELLS represented in the last 20 years one of the most groundbreaking technologic innovations in the solar energy conversion field. DSSCs architecture has been proposed by a seminal work of Grätzel et al. in 1991;[90] since then, more than 13000 paper has been published on the subject, reaching conversion efficiencies as high as 13%. Most of the efficient sensitizers for DSSCs that have been proposed up to now are organic dyes and metal complexes (e.g. Ru and Ir complexes) with high molar absorption coefficient in a broad region of the visible spectrum and good electron donating properties towards the mesoporous TiO_2 layer. These species often suffer from a low photo-stability in the near UV region, limiting the application in a real environment. In addition, they are often characterized by a low absorption coefficient in the near-UV region (350-400 nm) where the solar spectrum is still characterized by high intensity.

An interesting approach to addrees both these issues is to couple a luminescent downshifting layer (LDS) to conventional DSSCs. This layer must be able to absorb the UV light and emit in a region of the visible spectrum where the sensitizer is characterized by a strong molar absorption coefficient. Therefore, the LDS might be able to increase the power conversion

efficiency (PCE) of the cell by increasing the absorption in the near-UV region. Furthermore, if the LDS luminescent specie is a photostable specie with high molar absorption coefficient in the whole UV region, it should also act as a UV-filter, lowering the photo-degradation rate of the sensitizer. Different materials and configurations were proposed for this application, such as the deposition of an organic fluorescent polymeric coating,[91] the spin coating of $LaVO_4$[92] nanocrystals on the top of a transparent side of the cell, or the positioning of a reflective LDS layer based on Eu^{2+} phosphor on the back of the DSSC cell.[93] Also semiconductor QDs and nanocrystals are arousing interest for the application in LDS, thanks to the high stability and the tunable luminescence wavelength.[94]

Up to our knowledge, no attempt of using SiNCs as LDS has been made, despite the properties are matching most of the requirements of a nanocrystal based LDS.[95] For this reason, we performed some preliminary experiments to understand if the SiNCs are promising with respect to this specific application. In particular we prepared a set of conventional DSSCs adapting a procedure[96] developed in the lab where I spent several months of the PhD as a visiting student (INRS-EMT, Varennes (QC), Canada), under the supervision of Prof. Rosei:

The electrodes were prepared by cleaning some FTO coated glass slides under sonication in EtOH for 15 min (surface resistivity = $\sim 10\,\Omega/sq$), then 3 sides of each slide were covered with scotch tape. A layer of TiO_2 was deposited by Dr. Blade method on the free area. For a transparent layer a Dyesol® 18NR-T TiO_2 paste was used (7 μm), while for the scattering one a Dyesol® 18NR-AO paste with nanoparticles up to 450 nm was employed (8 μm). Where a second scattering layer was needed, the Dr. Blade was repeated after doubling the thickness of the scotch tape layer (16 μm). The samples were dried for 15 min at RT then they were heated at 150°C for 6 min. and stored. The TiO_2 layer was annealed at 500°C following a multi-step temperature ramp then it was slowly cooled to RT. The samples were then dipped in a N719 dye solution in EtOH for 24 h, then washed with EtOH and dried. The area of the electrode was finally reduced to a smaller active area (3-5 mm of side length). The DSSCs were fabricated by placing a 25 μm thick plastic spacer between the photoanode and the platinized FTO glass used as the counter-electrode (a 5 nm thin film of Pt on FTO by sputtering). Finally the I^-/I^- redox couple electrolyte was added and the PCE of the cell was evaluated with the instrumental setup described in appendix C.

In a first time, the LDS layer was deposited by spin coating on the back of the FTO trans-

parent electrode a 3 nm SiNC dispersion (1×10^{-5} M) in a solution of PMMA in CHCl$_3$ (10% w/w). The spin coating of the polymer resulted in a very thin layer (< 100 μm) and absolutely no effect was observed on the efficiency of the DSSC cells. The reason of this failure was attributed to the waveguide effect on the FTO-coated glass, that was bringing the light emitted by SiNCs away from the active area of the cell, towards the side of the transparent electrode. As we will discuss in the next section, this effect is very important to other applications (such as solar concentrators or optical fibers) but in this case it nullified the desired effect.

An alternative approach we developed consists in directly depositing the SiNCs dispersion by drop casting onto the mesoporous TiO$_2$ layer, before adsorbing the dye on its surface. No binding between SiNCs and TiO$_2$ is expected, due to the lack of carboxylic groups on SiNCs surface, therefore the evaporation of the solvent during the drop casting should result in a physical deposition of SiNCs within the mesoporous layer and on the top of it. A scheme of the architecture of the cell is reported in figure 2.14 a). As displayed in figure 2.14 b), there is a quite broad superposition between the absorption spectrum of the N719 dye (black line) and the emission spectrum of 3 nm SiNC prepared for this experiment (red dashed line). The ef-
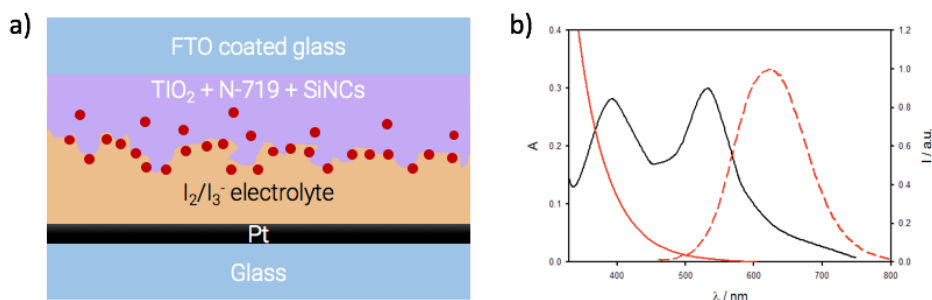
Figure 2.14: a) Schematic representation of the prepared DSSC with the 3 nm SiNC LDS layer. b) Absorption spectrum of the N719 dye (black continuous line) in comparison with the absorption (red continuous line) and the emission spectra (red dashed line) of 3 nm SiNC.

ficiency of the DSSCs prepared with the LDS layer was compared with the one of identically prepared cells with no addition of nanocrystals. The J-V curves measured for the set of samples we prepared is reported in figure 2.15 and the extracted parameters are summarized in table 2.1. The addition of the SiNCs layer produces similar results in all samples, differing only form the kind of titania layer deposited, as previously described in the experimental procedure. In

all cases, the short circuit current (J_{sc}) corresponding to the current density at bias = 0V, is increasing upon adding the LDS layer. At the same time, the open circuit voltage (V_{oc}) corresponding to maximum voltage the cell is able to reach, is increasing for the semi-transparent titania layer DSSC, while it is basically stable for the cells with one or more scattering layers. As a consequence, for all samples the PCE is increasing by adding the SiNCs layer. The relative
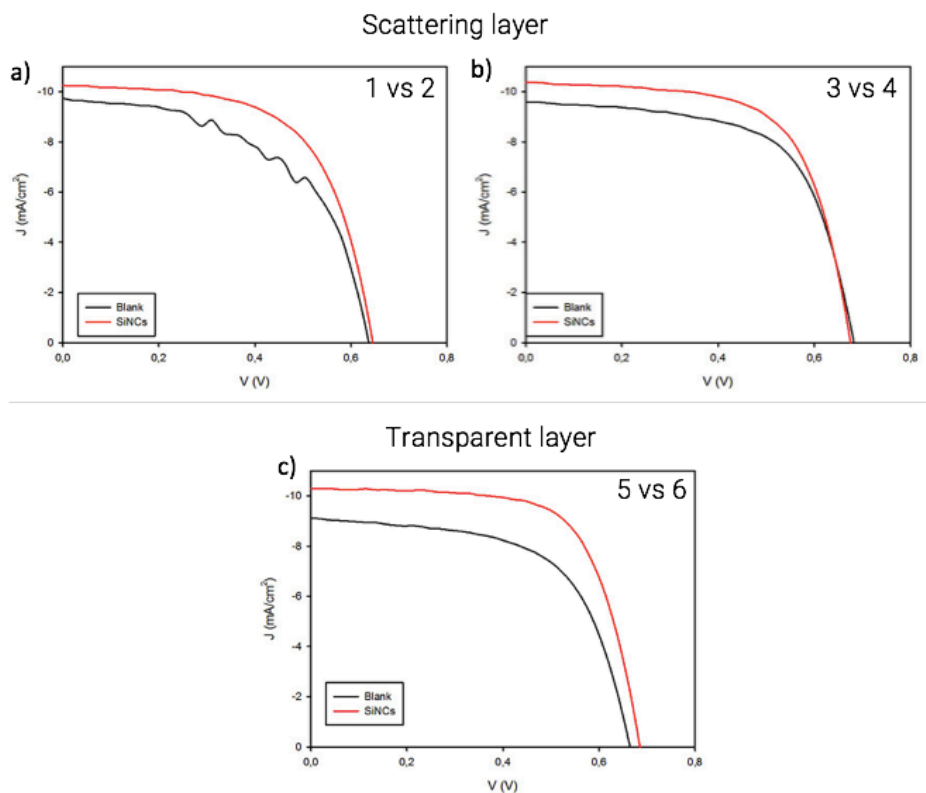
Figure 2.15: Comparison between the J-V curves of the DSSCs prepared in presence (red curves) and in absence (black curves) of a SiNCs LDS layer. The samples were prepared either with a a) single scattering titania layer, b) a double scattering titania layer, and c) a transparent. Please refer to table 2.1 for the sample number.

increment ranges from +10% for the DSSCs with a thick scattering layer, to a ∼+30% for the semi-transparent one. Even if the result is absolutely interesting, the reason of this dramatic increase has to be investigated. Indeed, It has been previously reported that the addition of

Table 2.1: Open circuit potential (V_{OC}), short circuit current (J_{SC}) and power conversion efficiency (PCE) of the DSSCs prepared in presence and in absence of a SiNCs LDS layer.

Sample	V_{OC} / V	J_{SC} / mA cm^{-2}	PCE	Δ_{PCE}
SCATTERING LAYER				
1 blank	0.637	9.74	3.32	
2 SiNCs	0.645	10.25	4.04	+22%
SCATTERING LAYER 2X				
3 blank	0.680	9.57	4.14	
4 SiNCs	0.675	10.37	4.55	+10%
TRANSPARENT LAYER				
5 blank	0.664	9.12	3.68	
6 SiNCs	0.685	10.29	4.77	+29%

scattering nanoparticles on the titania layer is able to positively affect the efficiency of the cell, increasing the probability of photon entrapment into the dye-doped titania layer, and therefore the probability of absorption.[97] This behaviour is consistent to the trend observed for our samples, being the highest increase in efficiency observed in the cell characterized by the less scattering TiO$_2$ layer. In contrast to this, the scattering contribution has been observed to be responsible of an increase of the J_{sc}, but no effect was observed on the V_{oc},[98] therefore we could hypothesize that there is a co-existence of a scattering effect and a down-shifting effect in our samples, in particular in the semi-transparent sample where a strong increase of the V_{oc} was observed.

In order to distinguish which effect is prevailing, we also evaluated the Incident Photon to Current efficiency, able to correlate the efficiency of the cell with the spectrum interval of the incident light. Unfortunately the measurement failed due to the low stability of the cells and the lack of reliability of the solar simulator in the near-UV region, which is fundamental to the understanding of the features of the LDS layer, therefore a new set of measurements is in progress to achieve a complete analysis of our system.

2.2.2   Polymer embedded Luminescent Solar Concentrator

AN ALTERNATIVE WAY to exploit the interesting photoluminescence properties of SiNCs consists in preparing luminescent solar concentrators (LSC) based on these interesting nanocrystals. LSCs have been first proposed in 1973 by Lerner et al. in a grant proposal[99] and they have attracted a wide interest in the first years due to the possibility of replacing the expensive Si-based large panels and increase the integration of photovoltaic cells in the urban environment. The decrease of the cost of Si, together with the drop in the oil prices in the early '80s froze the development of this architecture, but the opposite trend of the energetic market in the last years led to a re-discovering of this application. LSC architecture consists in a plastic plate embedded with luminescent species that extensively absorb sunlight and emit in a spectral window where conventional Si-cells or GaAs cells have high power conversion efficiency. The key feature of LSC is the shape factor of the polymer and, optimizing the design, it is possible to concentrate a substantial portion of the light emitted by the luminescent specie to the edge of the plate (up to $\sim$75% according to Snell's law[100]), trapping the light in the waveguide by total internal reflection (scheme represented in figure 2.16 a). The advantages provided by this simple setup are related mostly to the possibility of preparing large area polymer plates with relatively simple procedure and low cost, coupling it to small area, band-gap matched, high efficiency conventional PV cell. In addition to this, this architecture allows to prepare semi-transparent and colored polymer plates that can be used as large panels in windows and facades, as the one prepared in our lab and shown in figure 2.16 b). The optical efficiency of a LSC is defined by several factors, all included in the
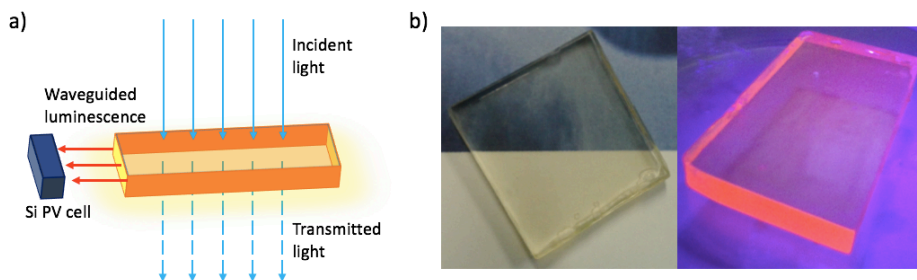

Figure 2.16: a) b) c)

following relation:

$$\eta_{opt} = (1 - R)P_{TIR}\eta_{abs}\eta_{PL}\eta_{Stokes}\eta_{wvg}\eta_{self} \tag{2.4}$$

Where R is the reflection of the incident light on the polymer surface, P_{TIR} is the total internal reflection effieciency defined by Snell's law, η_{abs} is the fraction of sunlight absorbed by the photoactive specie, η_{PL} is the photoluminescence quantum yield, η_{Stokes} is the energy lost due to heat generation, η_{wvg} is the efficiency of the waveguide light transport related to the shape factor and η_{self} is the the contribution to the efficiency given by the re-absorption of the emitted photons by another fluorophore. The two most important contributes, in terms of loss probability, are the surface losses and the re-absorption. While the first issue can be addressed by exploring different LSC configurations, the second one is mainly related to the luminophore photophysics. Moreover, a key point for the everyday application of LSC is related to the stability of the luminescent specie.

The record power conversion efficiency for an LSC-coupled PV cell is about 7.1% reported for a luminescent organic dye based LSC,[100] but in the last few years the interest has moved towards the nanowires and quantum dots based LSC. These luminophores are in fact characterized by higher photostability, simpler band-gap tunability[101] and higher Stokes shift, limiting the re-absorption losses. Several examples of QD-LSC are reported embedding Cd[102][103] and Pb[104] based quantum dots, obtaining relatively good efficiencies on non-optimized LSCs, but recently some concern about the use of toxic heavy metals in these applications is rising. As a consequence, some very recent papers such as the one published by Meinardi et al.[105] are now focused on the replacement of heavy metal based QDs with more environmental friendly species, such as $CuInS_xSe_{2-x}$ alloys QDs.

With respect to this application, SiNCs are certainly fascinating as non toxic, high Stokes-shift replacement for the most common quantum dots. Nevertheless, up to our knowledge, no attempt of embedding SiNCs for LSC application is present in literature, therefore we performed some preliminary investigation on its feasibility.

The polymer plates embedded with SiNCs were prepared adapting a procedure described by Bawendi et al.,[106] reducing the amount of photoinitiator in order to optimize the component of light absorbed by SiNCs:

300 μL of concentrated SiNCs solution in toluene($\sim 10^{-4}$-10^{-3}M depending on the

batch) were carefully dried under vacuum. In the meantime, a solution of the monomeric precursor (LMA, lauroyl methacrylate, Sigma-Aldrich), cross-linking agent (EGDM, ethylene glycol dimethacrylate, Sigma-Aldrich, 20%w/w with respect to LMA) and UV initiator (diphenyl(2,4,6-trimethylbenzoyl)phosphine oxide), Sigma-Aldrich, 0.1%) was prepared by sonication for 10 minutes. The SiNCs were then dissolved in 6 mL of the monomer and the solution was degassed by 3x freeze-pump-thaw cycles, in order to avoid the formation of bubbles during the polymerization. The solution was then placed in a homemade mold consisting in two glass slides separated by a silicone spacer and irradiated at λ_{ex}=365nm for 1h. The resulting polymer plate was left in dark for 24h, in order to allow the polymerization to complete, then the mold was removed and the polymer matrix was polished with sandpaper and diamond paste (1 μm).
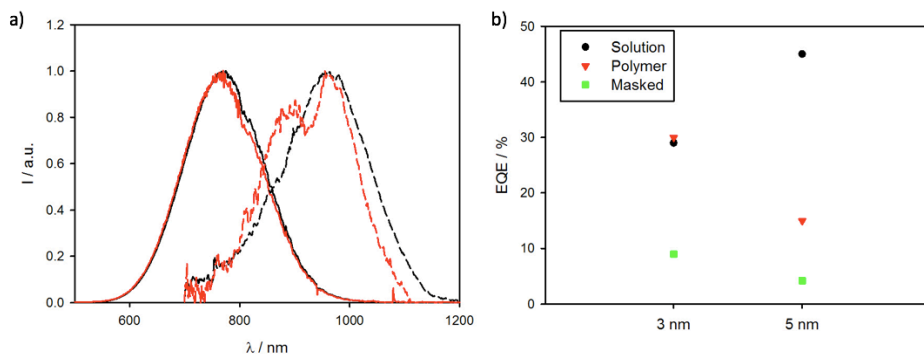
Figure 2.17: a) Normalized emission spectra of solution phase 3 nm (black continuous line) and 5 nm (black dashed line) SiNC compared with the emission spectra of the same batches of nanocrystals once embedded in the polymer matrix (respectively continuous and dashed red lines). b) External quantum efficiency of the same nanocrystals in solution (black dots) vs. polymer embedded (red triangles). The green squares represent the EQE of the polymer matrix after masking the edge of the polymer plate, in order to calculate the optical efficiency, as explained in the main text

First we compared the shape factor of the emission band of the 3 nm and 5 nm SiNC samples (please notice that no photoactive ligand was coupled to SiNCs in this section) once embedded in the polymer matrix with the one of the same nanocrystals in solution. As evident from figure 2.15 a), no particular variation of the band shape was observed for the 3 nm SiNC sample, while the embedded 5 nm SiNC sample is characterized by a dramatic change in the band shape due to the superposition of the emission band with the absorption bands of the LMA/EGDM

copolymer related to the typical vibrational overtones, as previously observed elesewhere.[105]

We then characterized the quantum yield or external quantum efficiency (EQE, in contrast to the IQE described in Chapter 1) of SiNCs once embedded in the LMA/EGDM copolymer and we compared the result with the one of the same nanocrystals dissolved in toluene. The quantum yield of a solid sample cannot be measured with the relative method used in chapter one for the samples in solution, therefore it is necessary to use an absolute method by means of an integrating sphere (further details on the method are described in Appendix A). The measurement was first made on the reference samples in solution, specifically a freshly prepared 3 nm SiNC and a 5 nm SiNC. The EQE value obtained for the 5 nm SiNC sample was consistent with the one measured for the same sample in Chapter 1, about 45%, while the 3 nm sample showed a much higher value of quantum yield equal to 28%, compared to the 16% previously observed with the relative method. The difference in these measurement is not due to a difference in the quality between these samples, but it is merely due to the difference in the measurement setup. The absolute measurement is taking into account the detector efficiency and therefore it must be considered as more reliable. Please notice that also the PL maximum wavelength is shifted due to the correction for the detector response (figure 2.17 a). We compared those efficiencies with the one of the same nanocrystals embedded in the polymer matrix (figure 2.17 b). In order to correctly perform the measurement, an homemade support for the 3x2cm plates was built and a reference plate was prepared with no addition of SiNCs for the blank measurement. While for the 3 nm SiNC sample the EQE was observed to be relatively similar to the one of the solution sample, about 30%, the 5 nm SiNC sample is affected by a dramatic decrease of EQE up to 15%, as a result of the re-absorption of the polymer matrix, already discussed with respect to the band shape observed in figure 2.17 a).

In order to get some information about the optical efficiency of the LSC, we measure the EQE of SiNCs embedded in the polymer plate and we compared it with the EQE of the same LSC masking the edges of the polymer plate, subtracting the contribute of the edges to the quantum efficiency, as previously suggested.[106] By masking the LSC made with the 3 nm SiNC sample, we observed a decreasing of the EQE from 30% to 9% (figure 2.17 b), pointing out that the 68% of the contribution to the overall emission intensity is coming from the edges of the polymer plate and revealing that very few losses are present due to re-absorption or surface reflection. The optical efficiency, calculated as the difference between the two calcu-

lated quantum efficiencies, is therefore equal to 21%. This value is a relatively good one, but comparing it to the quantum efficiency of the SiNCs we can understand how the main bottleneck is represented by the SiNCs photoluminescence quantum yield. Nevertheless, the 68% of EQE ratio is proving that optical quality of the concentrator is extremely high (near to the theoretical maximum previously described), so we expect that optimizing the synthesis of the SiNCs in order to increase their ϕ_{PL}, this architecture could represent an absolutely interesting alternative to conventional photovoltaics.

2.2.3 Conclusions

IN THIS CHAPTER we explored different routes to extract the energy provided by the light harvesting in SiNCs in order to exploit this material as active material in photovoltaic devices. We deeply investigated the photophysical intermolecular interaction of SiNCs with carbon allotropes observing a quenching of the luminescence of nanocrystals upon the addition of C_{60}, SWCNTs or graphene mainly due to an energy transfer process. Then, we investigated the feasibility of SiNCs implementation as light emitter in un-conventional solar cells. Specifically we made some preliminary study on the implementation of SiNCs as luminescent down-shifting layer in DSSCs obtaining a reproducible increase in the efficiency of the cell, and we prepared some luminescent solar concentrators by embedding SiNCs in an acrylic polymer matrix, obtaining good results in terms of transparency and optical efficiency. We can therefore asses that SiNCs might represent a viable solution as active material for different application in the conversion of the energy provided by sunlight, due to the very rich (even if complex) photophysics.

Anyone who has never made a mistake has never tried anything new.

Albert Einstein

3

Exfoliated Graphene decorated with platinum nanoparticles for electrocatalysis

IN THIS CHAPTER we report the synthesis of monodispersed platinum nanoparticles on high-quality graphene and the evaluation of their performance in the electrocatalytic production of H_2 from water at neutral pH. To the best of our knowledge, this is the first attempt to functionalize exfoliated graphene produced with different exfoliation techniques with Pt nanoparticles exploiting the non-covalent interaction with pyrene derivatives to drive the efficient decoration of the graphene membranes. The electrocatalytic activity of the nanocomposites towards the HER was evaluated and compared to a commercial carbon-supported platinum (Pt/C) catalyst

3.1 Electrocatalysis for Hydrogen production

THE NEVERENDING need for energy sources has increased exponentially during the last two centuries, driving economics, politics and everyday activity of the entire population. At the beginning of the 20th century, despite primary energy sources were still abundant, unrestricted, and inexpensive, several renewable sources were studied as an alternative both for electrical energy conversion and vehicles propulsion.
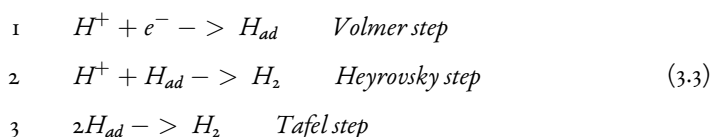
With the oil crisis of the late 70^s and the always higher concern for the environmental pollution due to the fossil fuels combustion, the interest in alternative fuels and alternative energy conversion devices spread all over the industrial and academic world. As regards the energy conversion technology, this had already been invented long time before by Sir William Grove under the name of Fuel cell, able to produce electrical current by exploiting the redox reaction between simple reactants like oxygen and hydrogen, with high efficiency and no pollutant produced (water is the only product). Hydrogen has the largest energy density over any other fuel in the world (about 286 kJ/mol with respect to combustion in oxygen environment) ([107]). In a fuel cell, Hydrogen typically splits into protons and electrons under the assistance of catalyst. Protons move from anode towards cathode through a conductive electrolyte, and electrons go through external circuit and meet with protons and oxygen in cathode. Then the product, water, is produced, as well as electric power. The voltage of this cell can be calculated by the Gibbs free energy, ΔG = -237.1 kJ/mol, which gives the voltage applying the Nernst equation: [108]

$$E = \frac{\Delta G}{nF} = 237.1 \; kJ/mol \, x \, 96485 \; C/mol = \; 1.229 \; V \tag{3.1}$$

There are only two drawbacks of using Hydrogen as energy carrier, first of all no natural sources of pure Hydrogen sources exist on earth, so it must be prepared by chemical reaction; moreover the storage of hydrogen is still challenging due to safety issue and low efficiency. [109] Nowadays there are two ways for us to produce hydrogen. In industry, hydrogen is produced by steam reforming of natural gas (CH_4), which is shown as follows:

$$CH_4(g) + H_2O(g) -> CO(g) + 3H_2(g) \tag{3.2}$$
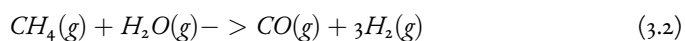
But hydrogen can also be produced from the water splitting, thanks to the reverse of the reaction exploited for the fuel cell, needing an output voltage equal to 1.23 V. This voltage is reversible, which means that 1.23 V is the lowest limit voltage we need to split water into hydrogen and oxygen. However, this potential is calculated thermodynamically, but kinetically higher voltage is needed depending on the catalyst we use. The Hydrogen Evolution Reaction is thought to involve three possible reaction steps, and may occur via the Volmer-Heyrowsky mechanism or the Volmer-Tafel mechanism, thus in both mechanism the the rate of the overall reaction is influenced by the free energy of hydrogen adsorption:

$$
\begin{array}{llll}
1 & H^+ + e^- -> H_{ad} & \textit{Volmer step} & \\
2 & H^+ + H_{ad} -> H_2 & \textit{Heyrovsky step} & (3.3) \\
3 & 2H_{ad} -> H_2 & \textit{Tafel step} &
\end{array}
$$

Where H_{ad} is the hydrogen adsorbed on the surface of the catalyst. Experimentally the rate of the reaction can be tested by applying a potential to the material and evaluating the current generated due to the HER reaction. The potential measured at the electrode (E_i) is subtracted to the Standard Potential (E_o), in order to obtain the overpotential η.

$$
\eta = E_i - E_o \tag{3.4}
$$

It is very important to understand the variation of current produced by the electrochemical reaction as a function of the overpotential. This relation can be fitted by the Butler-Volmer equation as a function of few parameters:

$$
i = i_o \left(\frac{\exp\left(-\alpha_a n F \eta\right)}{RT} \quad \frac{\exp\left(-\alpha_c n F \eta\right)}{RT} \right) \tag{3.5}
$$

Where i_o is the exchange current, α_a is the anodic simmetry coefficient whereas α_c is the cathodic one, n is the number of electrons involved in the reaction, F the Faraday constant and η is again the overpotential. If the overpotential goes to large negative values the anodic

reaction can be neglected and the relationship can be rewritten as the Tafel equation:

$$\eta \; = \; b \, ln(\frac{i}{i_\circ}) \tag{3.6}$$

Where b is the so-called Tafel slope, which together the exchange current $i_\circ$ are the criterions for the evaluation of the catalytic activity of catalysts. Generally, for HER, the catalytic activity increases as the exchange current increases or the Tafel slope decreases.

3.1.1 Platinum nanoparticles

Up to now, platinum is the unbeatable catalyst for HER which has the exchange current density of $4.5 \; 10^{-4} \; A/cm^2$, and the Tafel slope as small as $30 \; mV/dec$.[110] In addition to the extremely good catalytic activity, platinum is also showing extremely high price ad low availability, making the use of this noble metal as a bulk electrode unsuitable to everyday application. Since platinum is a precious metal, most of the recent efforts have focused on decreasing platinum utilization via increasing the catalytic efficiency of Pt-based catalysts. This can be done by tailoring high-performance Pt-based nanostructured materials. The catalytic activity is known to be strongly depending on the number of active sites on the surface of the metal catalyst and the ratio between surface and volume atoms is basically depending on a geometric factor. Therefore, by reducing the size of the material to few tens or hundreds of atoms, the number of surface exposed atoms approaches the total number of atoms of the nanomaterial. The number of active sites is then related on the shape of the particle and the specific activity of each crystallographic surface.

Hence, for a realistic model, one must assume that (a) the shape of the particles are such that their free energy is at a minimum, (b) atoms in excess of that required to form a complete geometric structure are located at the crystal sites which produce a particle as nearly spherical as possible. As a consequence, it is possible to see in figure 3.1 a direct relation between the size of the nanosphere and the number of active sites, considering all the surface sites with coordination number five (the so called B 5 sites).[111] The maximum value is reached at about 2.0 nm, because by further decreasing the size of the particle, the crystal structure starts to lose meaning and the contribution of edge sites increases. The same relationship is remarked by the
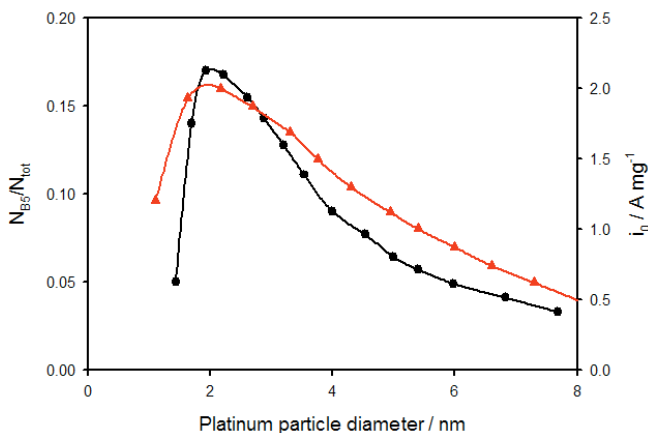
Figure 3.1: Number of active sites (black) and simulated mass current for HER plotted against the size of the Pt nanoparticle. The y-axis on the left corresponds to the black curve, while the y-axis on the right refers to the red plot. Adapted by [111] and. [112]

simulated mass current dependence ($i_\circ$) obtained by Tan et al. [112] for the HER with a maximum value obtained at 2.2 nm of diameter (figure 3.1, red curve). This behaviour basically results from the combination of the increasing surface/volume ratio with smaller size nanocrystals, as explained before, and the decreasing of the specific current ($j_\circ$) due to the increasing number of inactive edge sites.

3.1.2 Graphene as electroactive support material

FURTHER ATTENTION must be taken on the support material for the platinum nanoparticle (PtNPs). While the specific activity of the Pt nanoparticle is decreasing under a certain size, the overall performance can be maximized by supporting the catalyst in high surface area substrate, which plays a key role both on the proper dispersion of the nanoparticles, avoiding the spontaneous aggregation, and on the charge transfer efficiency from the electron source to the nano-catalyst.

Carbon allotropes have been extensively studied as nanostructured materials for electrocatalytic processes, being able to fulfill the major requirements for a catalyst support material as:

- High surface area

- Low electrical resistance

- High stability to electrochemical stress

- Low cost

Different kinds of carbon structures have been studied for this application (figure 3.2) such as amorphous carbon,[113] carbon nanofibers,[114] graphite nanoplatelets,[115] single and multi-walled carbon nanotubes,[116] graphene oxide[117] and, last but not least, exfoliated graphene.[118]
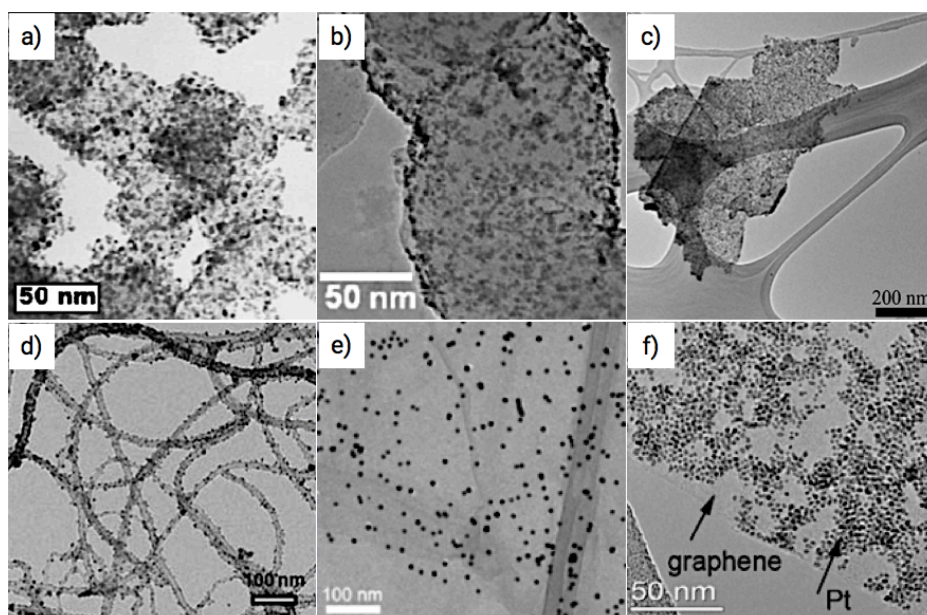
Figure 3.2: Representative TEM micrographs of platinum nanoparticles supported by a) amorphous carbon,[113] b) carbon nanofibers,[114] c) graphite nanoplatelets,[115] d) multi-walled carbon nanotubes,[116] e) graphene oxide[117] and f) exfoliated graphene.[118]

The most recently discovered carbon allotrope, graphene, is a material composed of sp^2-bonded carbon atoms, with monoatomic thickness, that displays outstanding mechanical and electrical properties[119][120]. Combining graphene with catalysts is a worthwhile approach in the

construction of novel materials for photo and electro-catalytic reactions [121],[122] and the development of high-quality graphene sheets, comprised of only a few layers of graphene and with a low frequency of defects, is extremely important for these applications. In contrast, graphene oxide (GO)[123] and the reduced graphene oxide (RGO)[124] are readily available but don't exhibit the typical structural and electrical properties of graphene, since oxidation and reduction steps are not able to completely restore the pristine honeycomb lattice of graphene.[125]

3.2   Exfoliated Graphene

COMPARED WITH RGO, exfoliated graphene has few or no functional groups on the surface of the honeycomb lattice, making any kind of direct covalent functionalization of the material difficult. As a consequence the exfoliation efficiency, as much as the stability in solution, is strongly affected by the surrounding environment. Noncovalent interactions could be an alternative way to tune the surface functionality of the graphene flakes, in order to leverage the liquid phase exfoliation[126] and to decorate graphene with molecules, nanoparticles or other structures.

The exfoliation of graphene flakes starting from bulk graphite can be basically split in three steps:[127]

- dispersion in solvent

- exfoliation

- purification

The key step is the exfoliation and has to be considered as the combination of two mechanism:

- breaking of the $\pi - \pi$ interaction between graphite (0,0,2) crystal planes by applying an external force

- stabilization of the exfoliated graphene layer in order to prevent re-aggregation

Breaking the graphite crystal along the desired axis is possible by ultrasonication of a graphite dispersion in organic solvent and it is mainly affected by the strength of the shear forces and

cavitation applied and indipendent on the solution environment. On the opposite, the second step is completely depending on the interaction with solvent and dissolved species.

Solvent assisted exfoliation

THE MOST COMMONLY used interaction exploited for the liquid-phase exfoliation is obviously the one with the solvent. The first attempt by Brodie to produce single-layer of graphite sheets by exfoliation dates as far back as 1859.[128] Since then, many efforts have been made in that direction but we have to wait until 2008 to see a strong improvement in exfoliation yield and average flake thickness (1-10 layer) thanks to the work performed by Hernandez et al.[129] In this paper they compare the exfoliation efficiency, in terms of concentration, of different solvents which were known to successfully disperse nanotubes as: 1-metil-2-pirrolidinone (NMP), N,N-Dimethylacetamide (DMA), g-butyrolactone (GBL) and 1,3-dimethyl-2-imidazolidinone (DMEU). The winner reveals to be NMP, and from there, it is still the best dispersing solvent for exfoliated graphene. At that time, no exhaustive explanation has been given about the reason why a typically polar solvent was so good at stabilising a theoretically strongly apolar nano-material as graphene.

Less than one year later, the same group has found a relationship between graphene's solubility and Hildebrand solubility parameter δ_T, defined as follows:[130]

$$\delta_T^2 = \delta_D^2 + \delta_P^2 + \delta_H^2 \tag{3.7}$$

Where δ_D^2, δ_P^2, δ_H^2 are respectively the dispersive, the polar and the hydrogen-bonding components, called Hansen parameters. Those components can be related to interaction between solute and solvent, which can be extracted from the Flory-Huggins theory for high molecular size solutes:

$$\chi = \frac{v_0}{kT} \left[(\delta_{D,A} - \delta_{D,B})^2 + (\delta_{P,A} - \delta_{P,B})^2 + (\delta_{H,A} - \delta_{H,B})^2 \right] \tag{3.8}$$

Where v_0 is the solvent molecular volume and χ is the Flory-Huggins parameter. According to eq. 3.8, the lower the value of χ, corresponding to the higher interaction solute/solvent, the

lower the energetic cost of dispersing (and exfoliating) graphene. By measuring the dispersibility of exfoliated graphene, C_G in figure 3.3 a), and plotting this value as a function of χ, the Hansen parameter of graphene are calculated as $\delta_D = 18.0 \ MPa^{1/2}$, $\delta_P = 9.3 \ MPa^{1/2}$, and $\delta_H = 7.7 \ MPa^{1/2}$.
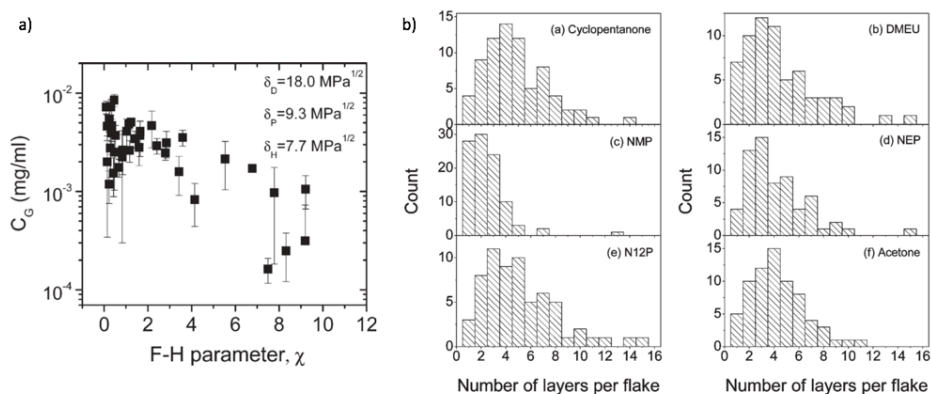
Figure 3.3: a) Measured dispersibility of exfoliated graphene (C_G as a function of the calculated Flory-Huggins parameter χ and b) hystograms reporting the average thickness of graphene flakes in different solvents obtained by HR-TEM analysis (see Appendix B for further details). Reprinted with permission from [130]

These values are very close to the ones observed for two solvents: cyclopentanone and cyclohexanone, so in principle they should be the best dispersing agent for stabilising graphene flakes. Unfortunately, this relation is true in terms of quantity of flakes, but not in terms of exfoliation degree. Indeed, the lowest average number of layers of exfoliated graphene is still obtained with NMP as solvent (figure 3.3 b), despite a slightly higher Flory-Huggins parameter. This means that still no full explanation of the solvent effect on graphene's exfoliation is available.

Nevertheless, the NMP assisted exfoliation is a very efficient process with a good degree of exfoliation and a concentration of graphene's flakes up to ~ 60 mg/mL. [131]

3.2.2   Interaction with aliphatic chains

THE USE of small organic molecules such as dispersion-stabilizing agents, can promote the exfoliation of graphite into graphene, in particular when such a molecule has a high energy of adsorption on the basal plane of graphene, stronger than that of the solvent molecules interacting with graphene. A good starting point can be the use of alkanes which are known to exhibit a high affinity for the surface of graphite/graphene.[132] It has been recently demonstrated that arachidic acid can be successfully exploited to promote the exfoliation of graphene in NMP[133] with an increasing concentration of graphene flakes in solution up to 50%.

A deeper investigation on the effect of linear alkanes exposing a carboxylic acid head group has been performed by us[134] in collaboration with the group lead by Prof. Paolo Samori' at ISIS Strasbourg in 2014. In this study we explore the role of the length of the alkylic chain by focusing the attention of five carboxylic acid derivatives, schematized in figure 3.4 a).
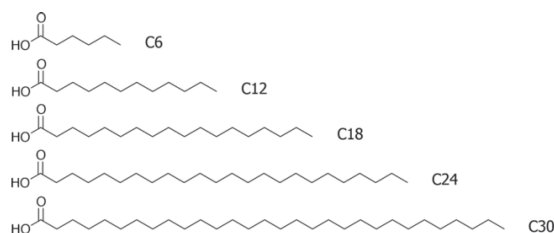
Figure 3.4: Chemical structures of investigated carboxylic acid derivatives.

Moreover, the study is extended to graphene dispersions in four different solvents as N-methyl-2-pyrrolidone (NMP), ortho-dichlorobenzene (o-DCB), 1,2,4-trichlorobenzene (TCB), and N,N-dimethylformamide (DMF). Interestingly, we found that the concentration of graphene prepared in NMP, o-DCB and TCB increases almost linearly with the length of the aliphatic chain (figure 3.5) except for the data points at highest alkane length in o-DCB and TCB, where concentration falls down because of the long fatty acid proneness to form gel-like structures.

The TEM analysis of the samples allowed to obtain a statistical characterisation of the thickness and the lateral size of the graphene flakes produced. While for NMP solutions no strong
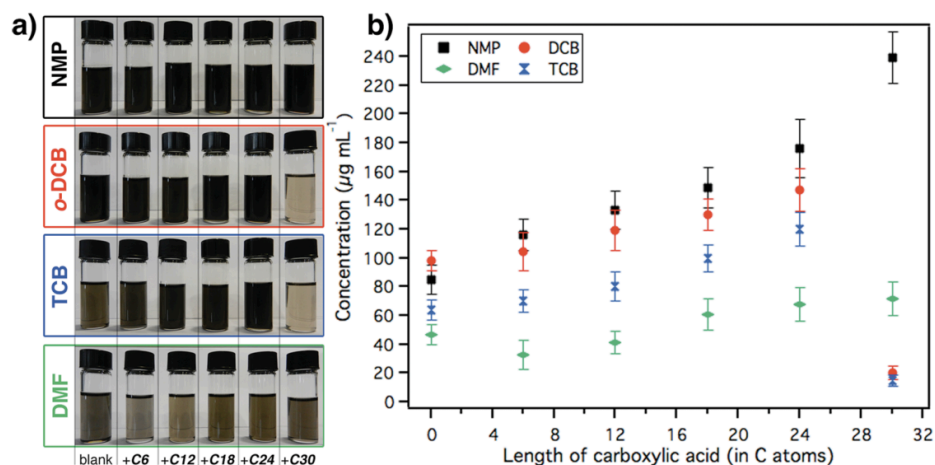
Figure 3.5: Photographs of graphene dispersions prepared by exfoliation of graphite flakes in NMP, o- DCB, TCB, and DMF in presence/absence of carboxylic acid molecules; b) average concentration of graphene dispersions after the filtration process.

variation on the flakes morphology was observed, with relatively poorer solvents as DMF, o-DCB and TCB, the addition of the long fatty acid (C24 results are shown in figure 3.6 for comparison) resulted in a variation of either flakes thickness or size. Even if o-DCB showed an unpredictable increase of both size and thickness, DMF and TCB showed an interesting increase of the percentage of monolayer graphene, respectively of about 15% in the case of C24/TCB, 8% in C24/DMF and 16% in C30/DMF.

The interaction between graphene and alkylic chains can also be exploited to functionalize the surface with more complex functionalities. In a second study in collaboration with the ISIS Strasbourg, we combined a photochromic system, a commercial alkoxy-substituted azobenzene, i.e. 4-(decyloxy)azobenzene, with liquid phase exfoliated graphene.[135] The exfoliation of graphene was performed again in NMP, taking good account of what we observed in the previous paper.

When the exfoliation was performed in the absence of 4-(decyloxy)azobenzene molecules (control experiments), comparable yield were observed when dispersions were kept at 20°C or heated at 40°C (figure 3.7). The irradiation of such dispersions at 365 nm did not affect the yield, neither at 20°C nor at 40°C. By adding 4-(decyloxy)azobenzene in dark, a minor
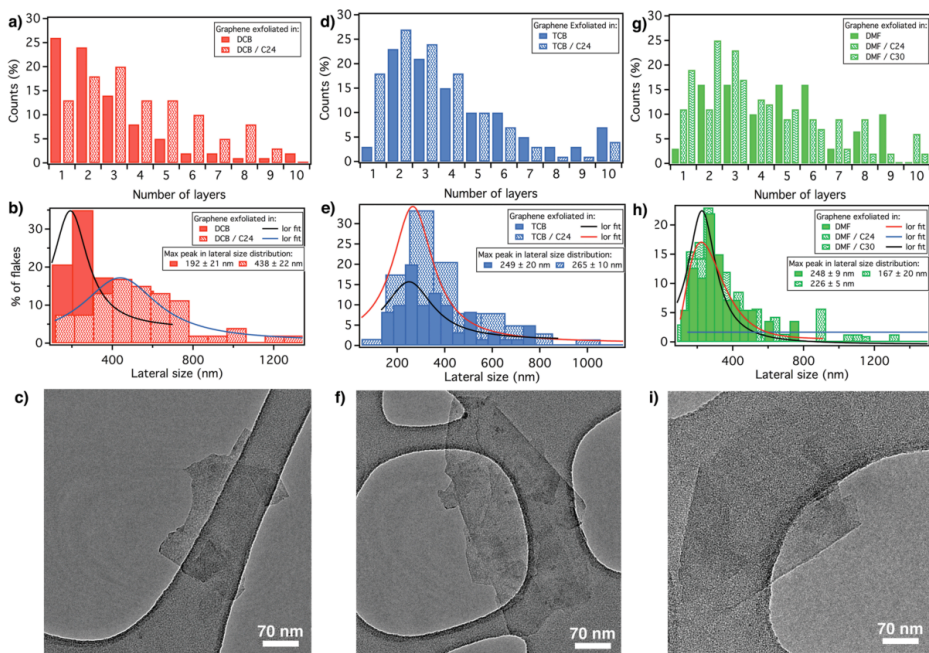
Figure 3.6: a-h) Statistical analysis of the number of layers graphene dispersions in a) o -DCB, d) TCB, and g) DMF, as well as in the presence of C24 (o-DCB, TCB, DMF) and C30 molecules (DMF). Histograms of the lateral flake size distribution of graphene flakes prepared in (b) o-DCB, (e) TCB, and (h) DMF and relative Lorentzian fitting.The fitting of the distribution has been obtained with a Lorentzian distribution. (c, f, i) TEM micrographs of folded monolayer graphene flakes prepared from dispersions in c) o-DCB/ C24 , f) TCB, and i) DMF/ C24.
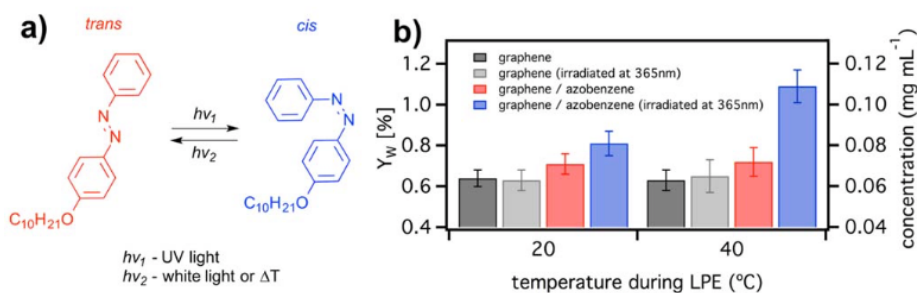
Figure 3.7: a) Chemical structure of 4-(decyloxy)azobenzene and reversible trans-cis photoisomerization under UV and visible light. b) Yield of the exfoliation given by Y_W as well as average concentration of graphene dispersions after the filtration process.

increase in the yield value highlighted the importance played by the alkylic derivative during the exfoliation. In contrast to the experiments performed in dark, irradiation with UV light at 365 nm (promoting the photo-isomerization to cis form) corresponded to 30% increase in the concentration of the exfoliated material at 20°C. Yet, the largest increase in concentration has been obtained by irradiating the dispersions heated at 40°C, which corresponds to a 75% increase.

In order to probe the electrical properties of the graphene-azobenzene hybrid and in particular to explore the potential light-responsive nature of the material, we drop-casted a 100 nm thick graphene-azobenzene film on a $n^{++}Si/SiO_2$ substrates exposing pre-patterned interdigitated gold electrodes. In the azobenzene-graphene film, the molecules are physisorbed on top and in between the graphene sheets. Under UV irradiation, the azobenzene molecules undergo a conformational change from the less bulky trans isomer to the more bulky cis isomer. Such a process is therefore accompanied by an increase in the multilayer graphene inter-sheet distance, thereby hindering the charge transport via hopping between the sheets, resulting in the lower conductivity of the hybrid film observed in figure 3.8 d).

3.2.3 Interaction with aromatic derivatives

PYRENE DERIVATIVES have been used by various groups to stabilize carbon nanotubes[136] and graphene dispersions,[137] exploiting the $\pi - \pi$ interaction between the planar π-conjugated surfaces, by reducing the surface free energy of the dispersion. This approach has the main advantage to allow an interesting tunability of graphene's surface in order to prepare stable solution in polar solvents as, for example, water. Moreover, this is possible without affecting the electrical properties usually compromised by the excess of surfactant or alkylic derivative usually needed to get sufficiently stable solutions.[138] A broad library of pyrenic exfoliating agents has been explored: the first paper was published by An et al. in 2010,[78] who prepared acqueous graphene dispersions using 1-pyrenecaboxylic acid as stabilizer; then amino-pyrene was used for the same target.[139] Green and co-workers[140] investigated the exfoliation yield of pyrene, 1-aminopyrene, 1-aminomethyl pyrene, 1-pyrene- carboxylic acid, 1-pyrenebutyric acid, 1-pyrene- butanol, 1-pyrenesulfonic acid hydrate, 1-pyrenesulfonic acid sodium salt and 1,3,6,8-pyrene-tetrasulfonic tetra acid tetra sodium salt, finding that the most effective molecule is 1-pyrenesulfonic acid sodium salt. A deeper study of the mechanism of surface adsorption of
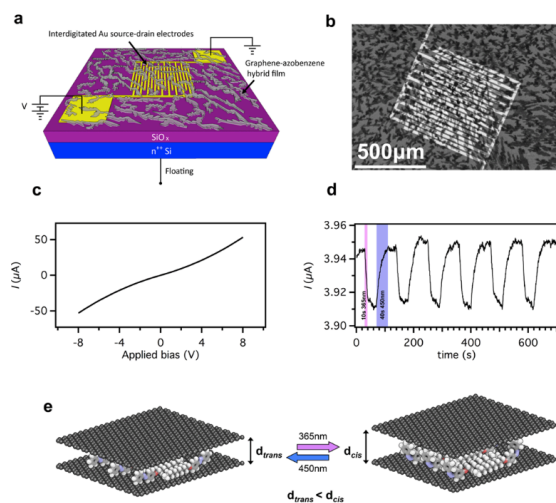
Figure 3.8: Electrical characteristics of graphene-azobenzene hybrid materials. a) Scheme of the G-FET device, b) SEM image of interdigitated Au electrodes covered with a graphene-azobenzene hybrid film. c) I-V characteristics, d) optical modulation of device current response illustrated for a static bias and dynamic alternative UV and visible light irradiation. e) "Ideal mechanism" which occurs in thin graphene-azobenzene hybrid films under UV and visible light irradiation cycles.

organic pyrene dyes on graphene was the aim of the paper published by Palermo et al.,[77] which indicates that the molecular dipole is not important per se, but since it facilitates adsorption on graphene, it promotes lateral displacement of water molecules collocated between the aromatic cores of the organic dye and graphene.

3.3 Decoration of exfoliated graphene with platinum nanoparticles

GRAPHENE/METAL NANOPARTICLES COMPOSITES gained attention in recent years within the field of fuel cells[123][118],[141] biosensing[116],[114] organic photovoltaics[117] and hydrogen production, due to the combination of good electrical properties with high transmittance, allowing for instance the coupling with a photosensitizer[142] to study the photocatalyzed hydrogen evolution reaction. As already mentioned in the first section of this chapter, Pt nanoparticles are typically supported on graphene oxide or reduced graphene oxide, whose surface is characterized by multiple hydroxy, epoxy and carboxylic groups able to drive the interaction with the nanoparticles due to electrostatic interaction.[143] On the other hand, the electrical properties are far from the ones observed for mechanically exfoliated graphene or even exfoliated graphene from pristine graphite. As a consequence we were interested in understanding how to induce the decoration of high-quality exfoliated graphene with Pt nanoparticles without affecting the honeycomb lattice responsible for the interesting properties of this carbon allotrope. The functionalization of exfoliated graphene with platinum nanoparticles may exploit the same forces enhancing the exfoliation and dispersion of graphene flakes in solution. Key points for the efficient decoration of exfoliated graphene are:

- Quality of the produced graphene flakes.
- Solvent compatibility between graphene exfoliation and Platinum nanoparticles synthesis.
- Control on size and aggregation of the synthesised nanoparticles.
- Selective functionalization of graphene's surface exploiting non-covalent interactions.

Our aim was to understand the role of different exfoliation techniques on the Pt nanoparticles decoration, and the consequences on the electrocatalyzed production of hydrogen in mild

condition, i.e. in slightly acid water environment.

3.3.1 Graphene solutions preparation

As DESCRIBED in the previous section, the exfoliation of graphite into graphene nanosheets is strongly depending on the solution environment. Since we were interested in water environment we adapted two literature procedures to prepare water graphene deispersions that could, in a second time, act as support for the synthesis of platinum nanoparticles. The first technique we chose to reproduce was one of the few developed in water environment and it is based on the interaction with 1-pyrenecarboxylic acid (PCA).[78] Indeed, PCA is used as a molecular wedge to cleave natural graphite, and thanks to its $\pi - \pi$ interactions and its polar functional group, it permits the formation of stable aqueous dispersions of graphene, without breaking the sp^2 structure. Moreover, the carboxylic group is known to interact with Pt nanoparticles surface in water solution, therefore enhancing the stability of the hybrid material. The main advantage of the PCA based exfoliation technique lies in the compatibility of the procedure with a single-flow process for platinum nanoparticle synthesis.

The experimental procedure was developed as follows:

6,7 mg of PCA were added to 20 ml of a 2 mg/mL solution of Graphite powder in methanol. The solution was bath sonicated for 45 min at RT, then 80 ml of distilled water were added. The solution was sonicated for 24 h keeping the temperature under 20°C, then it was settled overnight. The surnatant was removed and the solution was topped off with distilled water. The pH of the solution was adjusted to 7 in order to completely deprotonate the PCA and increase the solubility. After 2 h sonication, the solution was centrifuged three times at 10000 RPM and the precipitate was redispersed in distilled water. After the last centrifugation step, the solution was decanted for three days and the surnatant was stored.

The Raman spectrum of the PCA exfoliated graphene material (PCA-G henceforward) is shown in figure 3.9. The D-band at 1350 cm^{-1} reflects the degree of defects and disorder on graphene, while the G-band at 1580 cm^{-1} represents the planar vibration of the sp^2 carbon network. From the intensity ratio of these two peaks (I_D/I_G) we can obtain some information about the density of defects of graphene, and the small I_D/I_G value of 0.073 is a proof of a low defect density on our material after the exfoliation procedure with PCA.
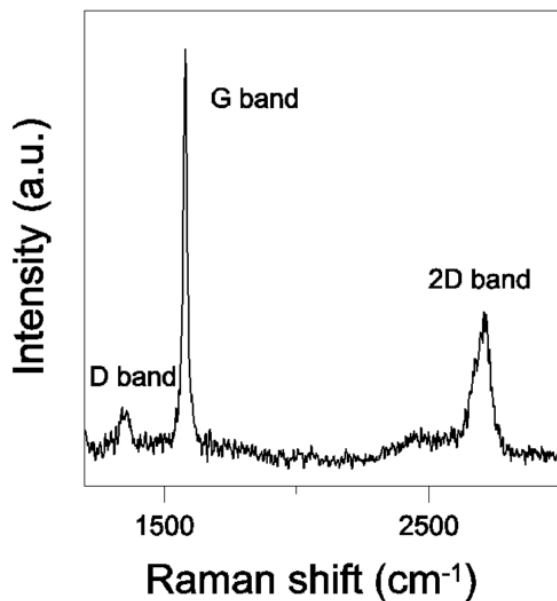
Figure 3.9: Raman spectra of the exfoliated PCA-G material.

For comparison purposes, a further graphene sample was prepared, adapting Coleman's procedure[129] to get highly exfoliated graphene sheets dispersed in 1-methyl-2-pyrrolidone (NMP). In order to compare these graphene dispersions with the acqueous dispersions of PCA-G, we developed a simple solvent exchange procedure to disperse NMP exfoliated graphene nanosheets in water.

The experimental procedure starts from the preparation of a 2mg/ml solution of Graphite powder that was bath sonicated for 12 h keeping the temperature under 20°C, then the solution was centrifuged at 3000 RPM for 20 min. and decanted for three days. The surnatant was stored. 2 ml of the solution were filtered onto a 0,2 mm PTFE membrane, then washed with acetone, isopropyl alcohol and water. The solid cake topped filter was then sonicated inside 10 ml of distilled water to transfer graphene into the solution (NMP-G henceforward).

Figure 3.10 shows the comparison of the typical absorption spectra of PCA-G and NMP-G. The concentration of graphene dissolved was calculated through Lambert-Beer equation, by considering the molar absorption coefficient provided by Hernandez[129] and reported on the
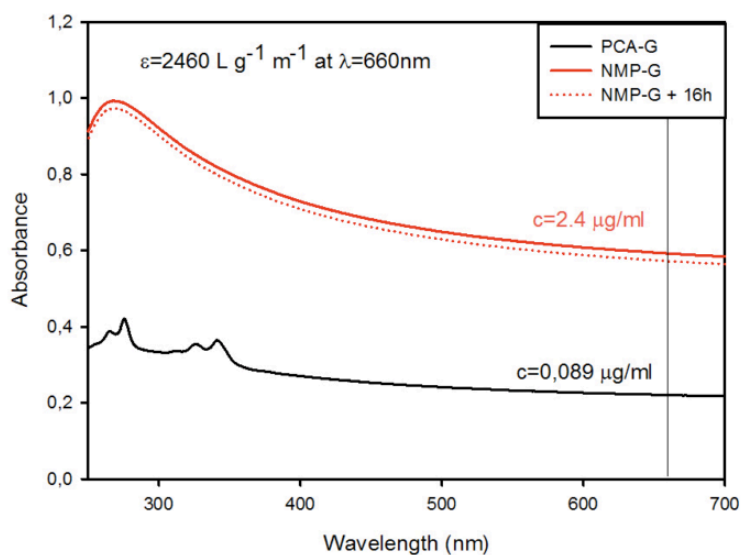
Figure 3.10: Absorption spectra of PCA-G (black) and NMP-G (red). The structured bands centered at 345 and 280 nm fo PCA-G spectrum were due to the presence of PCA, which is impossible to remove due to the synthetic procedure. The dotted line shows the absorption of NMP-G after 16 h, showing a good stability.

graph. Higher concentration of graphene flakes was found for the NMP-G sample (2.4 mg mL^{-1}) compared with the concentration found for the PCA-G sample (0.089 mg mL^{-1}).

Analysis of the final aqueous suspension after transfer from NMP suggests very good stability of the exfoliated graphene after 16h, as previously reported in literature[144].[145] Finally, to the NMP-G solution a certain amount of PCA was added in order to obtain an equivalent concentration of PCA with respect to the residual one in PCA-G solution (2 10^{-5} M).

Figure 3.11 shows the results of the HR-TEM characterization of the products of the two exfoliation techniques. Statistical analysis of the number of layers was made by directly counting the (0,0,2) fringes at the flake folding edges, which correlate directly to the number of layers. As highlighted by the example micrographs shown in figure 3.11, the degree of exfoliation was found to be slightly higher, in particular in term of thickness distribution, for the NMP-G sample.
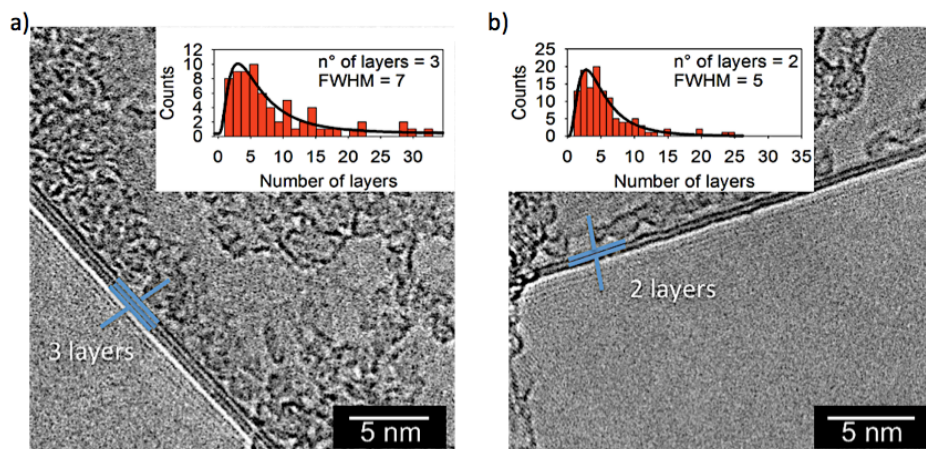
Figure 3.11: High-resolution transmission electron microscopy (HR-TEM) images of graphene sheets exfoliated by using a) the PCA-G method involving 1-pyrene- carboxylic acid (PCA) and b) the NMP-G method involving 1-methyl-2-pyrrolidone (NMP); histograms above show the corresponding distribution.

3.3.2   Platinum nanoparticles decoration: influence of the exfoliation technique

THE SYNTHESIS of the nanoparticles was carried out following a procedure adapted from the literature.[146] The method is based on the chemical reduction of an aqueous solution of a platinum(II) salt (K_2PtCl_4) by sodium borohydride, in the presence of the exfoliated graphene dispersions. Here the complete procedure:

50 μl of K_2PtCl_4 6 $*$ 10^{-3} M water solution was added to 10 ml of an exfoliated graphene dispersion μl of a 6 $*$ 10^{-2} M freshly prepared solution of NaBH$_4$ were added in order to reduce the platinum salt to Pt$_0$. A small excess of NaBH$_4$ was added to balance the small consumption due to the spontaneous production of hydrogen bubbles inside acqueos solution. The synthesis was followed by UV-Vis spectroscopy, and figure 3.12 shows an example of the absorption spectra taken during the synthesis of the Pt nanoparticles inside NMP-G sample.
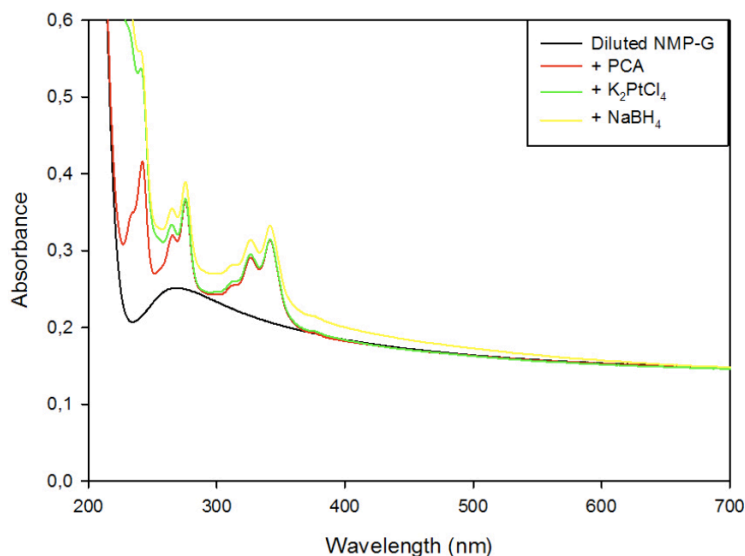
Figure 3.12: Absorption spectra of the NMP-G sample during the synthesis of the Pt nanoparticles. The addition of the PCA (red) is necessary only for NMP-G sample. The addition of the reducing agent (yellow), after the one of the Platinum salt (green), induced the increase of a scattering-like band in the UV zone, typical of small Pt nanoparticles.

Figure 3.13 shows the comparison between the results of the platinum nanoparticle decoration of exfoliated graphene using the PCA-G and NMP-G methods. The STEM and HR-TEM micrographs (figure 3.13 a-d) clearly show the strong selectivity of the decoration, without any particles outside the platelets, with a slightly lower concentration of particles in the NMP-G sample. We attributed this observation to the different concentration of graphene flakes for this sample, resulting in a lower platinum nanoparticle/graphene ratio. Nevertheless, both samples are characterized by a rather negligible aggregation of nanoparticles, proving that the graphene-PCA adduct acts as a scaffold for the arrangement of the particles on graphene, preventing the typical coalescence and precipitation issues. By focusing on the HR-TEM micrographs (figure 3.13 c) and d), it is possible to notice how the shape is more homogeneous and spherical in the NMP-G sample, while the size distribution reveals a lower degree of polydispersion despite the same average size for both samples.

This could be the result of residual NMP on the surface of sample prepared using the NMP-G method and explain the unexpected stability of the graphene dispersion in water. Residual NMP on the surface could also influence the morphology of the particles by confining the growth of the platinum crystal or by decreasing the graphene surface area available for interaction with PCA.

3.3.3 Platinum nanoparticles decoration: the role of 1-pyrene carboxylic acid

IN ORDER TO evaluate the influence and the role of PCA on the selectivity of the decoration and on the morphology of the platinum nanoparticles, we prepared some water dispersions of graphite nanoplatelets, simply sonicating a 2 mg mL^{-1} solution of graphite powder in distilled water for 24 hours. This dispersion was characterised by a very low degree of exfoliation of graphite; however, it allowed us to investigate decoration with platinum nanoparticles in the absence of any secondary variables, such as the influence of an exfoliating agent or a stabiliser. Using these samples, we performed the synthesis of platinum-nanoparticles, following the same method previously reported, with or without the addition of PCA. In both cases, the TEM images demonstrated a strongly preferential decoration of the graphite flakes, as showed in figure 3.14 a and d. The sample prepared without PCA shows very non-homogeneous size and shape distributions for the platinum nanoparticles (figure 3.14 b), whereas the sample prepared with PCA displays spherical and well-dispersed particles on the graphite platelets (fig-
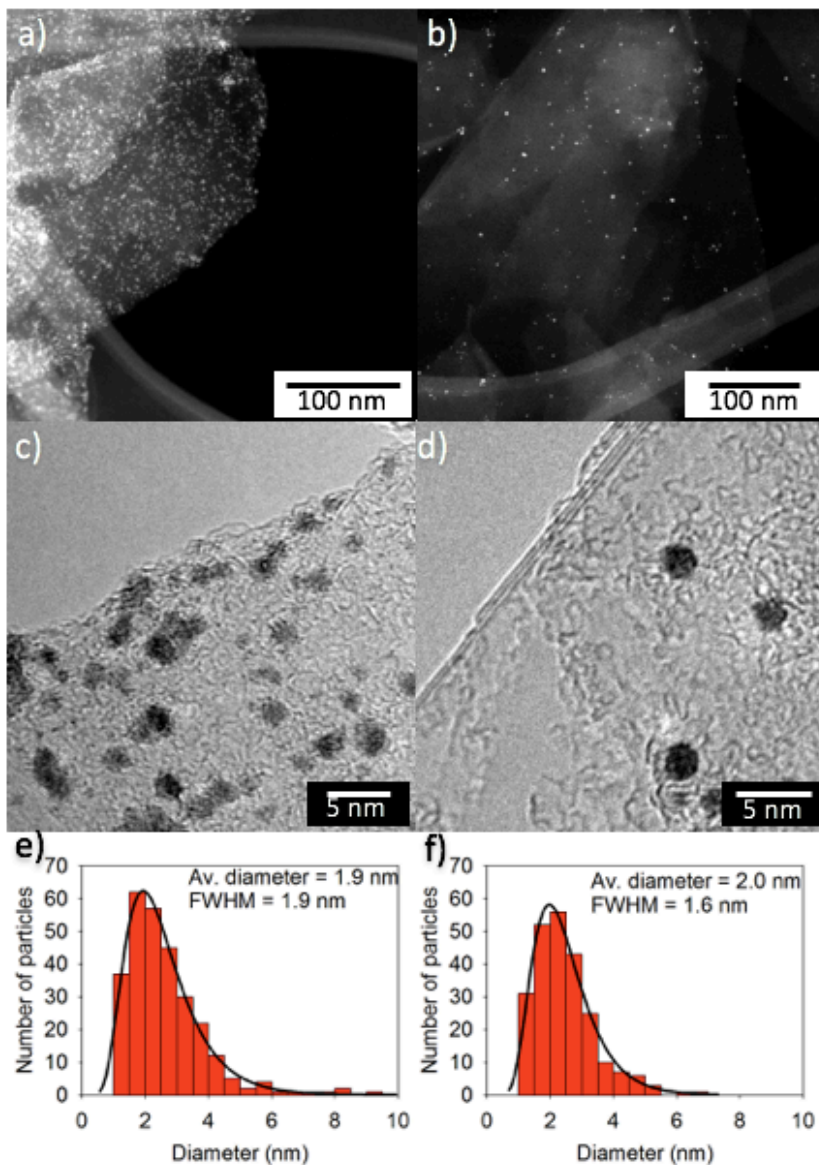
Figure 3.13: Comparison between decoration of exfoliated graphene produced with different techniques: PCA-G using 1-pyrenecarboxylic acid (PCA) (left) and NMP-G using 1-methyl-2-pyrrolidone (NMP) (right). a,b) Low-magnification scanning transmission electron microscope (STEM) micrographs of decorated graphene flakes. c,d) High-resolution transmission electron microscopy (HR-TEM) micrographs of flake edges covered by platinum nanoparticles. e,f) Size distribution histogram of the platinum nanoparticles synthesized on graphene. The distribution was fitted by using the Lorentz function, and the average diameter is reported in the inset.

ure 3.14 e). Magnification of the sporadic platinum nanoparticles outside the graphene surface show in both cases non-homogeneous distributions of size and shape due to aggregation of the particles, emphasising the differences between nanoparticles on and outside the graphene surface for the sample prepared with PCA (figure 3.14 c,f).
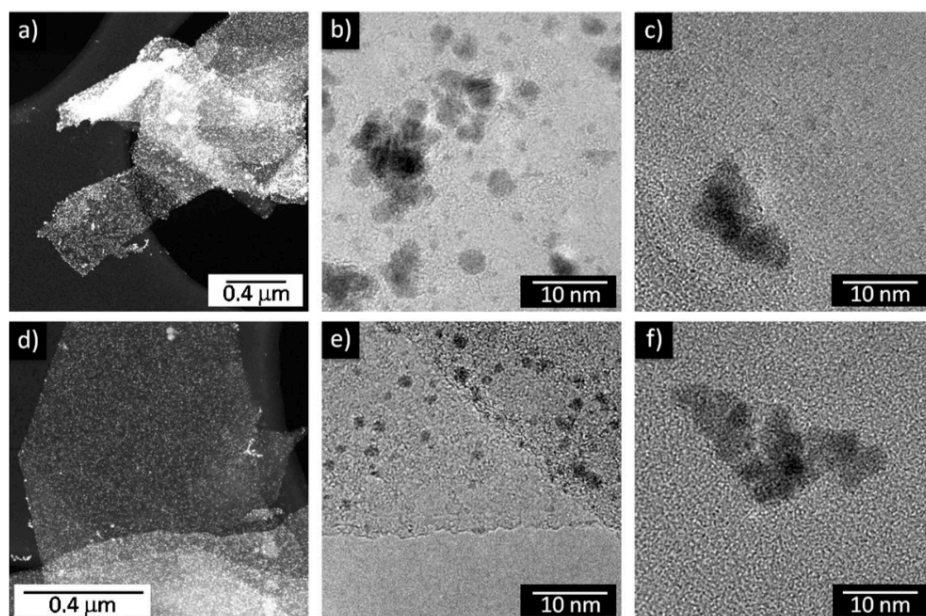
Figure 3.14: Comparison between platinum nanoparticles decoration of graphite platelets in the absence (a,b,c) and in the presence (d,e,f) of 1-pyrenecarboxylic acid (PCA). a,d) Low-magnification scanning transmission electron microscope (STEM) micrographs showing the very selective decoration. b,e) High-resolution transmission electron microscopy (HR-TEM) micrographs of platelets surfaces. c,f) Morphology of the particles outside graphene, which are usually aggregated into clusters.

The results of the latter experiment seem to confirm the hypothesis, formulated by Qian et al.,[118] that there is a direct electronic interaction between platinum atoms and graphene. Using density functional theory (DFT) calculations, Qian and co-workers estimated the binding energy. The obtained value of 1.39 eV is not so strong so as to profoundly modify the electronic structure of graphene; however, it is only slightly weaker than a typical chemical bond and thus sufficiently strong to selectively decorate the graphene sheets. These evidences suggest that the presence of PCA does not have a significant effect on the binding energy between graphene

and colloidal platinum; however, PCA does control the morphology of the nanoparticles and favors their homogeneous dispersion on graphene surface.[147]

Electrocatalytic performance towards hydrogen production

THE ELECTROCHEMISTRY of the two graphene composites prepared with the PCA-G and NMP-G methods was investigated to test the catalytic activity towards the HER and to gain further information on the properties of our materials. To characterize the two samples, we drop-casted 100 mL of the aqueous suspensions on a screen-printed electrode (SPE) that was used as the working electrode and placed at the bottom of an air-tight single-compartment cell, described elsewhere.[148] A silver chloride electrode (Ag/AgCl) (3m) and a platinum spiral were used as a reference and counter electrode, respectively; the potential of the Ag/AgCl electrode was measured before and after every experiment with re- spect to a standard saturated calomel electrode (SCE). Phosphate buffer solution at pH 6.8 was specifically prepared by commercially available salts, saturated with argon before each measurement and kept under argon at atmospheric pressure.
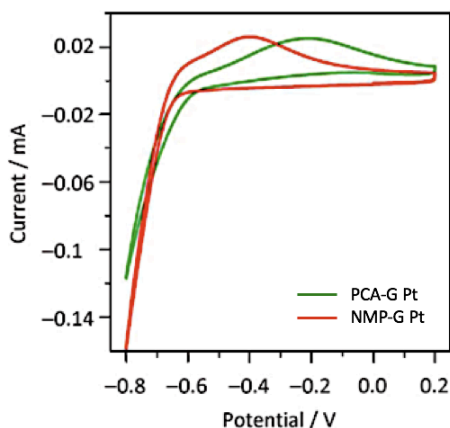
Figure 3.15: Comparison of the cyclic voltammetries (CVs) for the PCA-G Pt (green) and NMP-G Pt (red) samples; potentials are referred versus a standard saturated calomel electrode (SCE). v = 0.05 V s^{-1}, argon-saturated phosphate buffer solution (pH 6.8).

The effect of the exfoliating method on the electrochemistry of the platinum-

functionalized graphene is shown in figure 3.15 and reflects what we observed by HR-TEM micrographs shown in figure 3.11; the higher degree of exfoliation in the sample prepared using the NMP-G method gives rise to a composite material with better electronic properties that result in a less resistive electron-transfer process at the electrode.

The activity towards the HER was evaluated for the best performing material, NMP-G decorated with platinum nanoparticles (NMP-G Pt) and compared with the model system NMP-G (without metal nano- particles). The cyclic voltammetries (CVs) are reported in figure 3.16 a. The catalytic cathodic current of NMP-G Pt clearly shows the high activity of this material for HER, while the parent system NMP-G is inactive up to large overpotentials The stability of the NMP-G Pt material was tested running a chronoamperometry experiment for 30 minutes (figure 3.16 b), during which we applied a constant potential of -0.8V (versus SCE). The cathodic current reaches the stationary state, and we do not observe any appreciable loss of activity during the course of the measure.
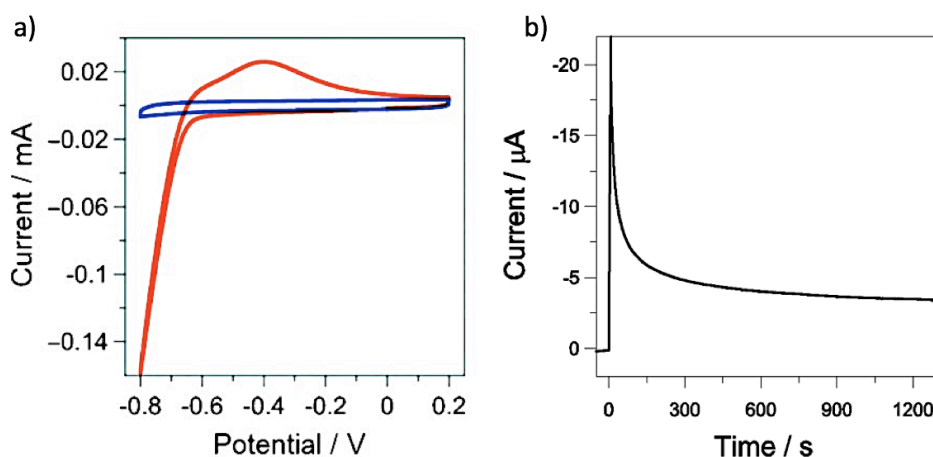
Figure 3.16: a) Cyclic voltammetries (CVs) for the NMP-G Pt (red) against the graphene control sample NMP-G (red) potentials; are referred versus a standard saturated calomel electrode (SCE). v = 0.05 V s^{-1}, argon-saturated phosphate buffer solution (pH 6.8). b) Chronoamperometry experiment (30 min.) on NMP-G Pt sample showing the Cathodic current vs. time for the NMP-G Pt material. Applied potential: -0.8V versus SCE.

Quantification of the catalytic efficiency of the graphene-based catalyst was performed by the combination of chronoamperometric experiments carried out at various negative poten-

tials (0.7, 0.8, 1.0 V versus Ag/AgCl; figure 3.17 a) and cyclic voltammetry. The experiments are useful to extract some parameters essential to the calculation of the so-called turnover number (TON; moles of product per moles of catalyst) and turnover frequencies (TOF; TON per time unit).
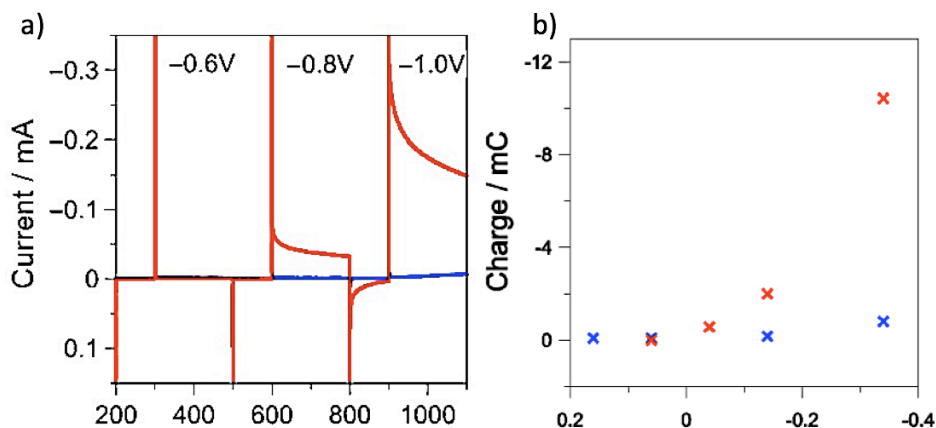
Figure 3.17: a) Chronoamperometries for NMP-G Pt (red) and NMP-G (blue); potentials are referred versus a standard saturated calomel electrode (SCE). b)integrated charges from the CA potential steps for the NMP-G Pt (red line) and NMP-G (blue line) samples. Phosphate Buffer solution at pH=6.8, v = 0.1 V/s, Ar saturated solution.

TON and TOF are defined by 3.9 and 3.10:

$$TON = \frac{Q_{NMP-GPt}}{Q_{NMP-G}} \tag{3.9}$$

$$TOF = \frac{TON}{t} \tag{3.10}$$

Where :

- $Q_{NMP-GPt}$ is the integrated charge etracted from the chronoamperometry experiment and related to the amount of evolved hydrogen ($2H^+ + 2e^- \longrightarrow H_2$) for the sample NMP-G Pt (red crosses in Fig. 3.17 b).

- Q_{NMP-G} is the contribution of the carbon-based substrate NMP-G (blue crosses in Fig. 3.17 b).

- Q_{Pt} is the charge referred to the electroactive platinum present in the composite and t is the duration of the applied potential step.

The Q_{Pt} factor is obtained by measuring the charges of the bi-electronic oxidation process ($Pt + H_2O \longrightarrow PtO + 2e^- + 2H^+$) that occurs at the surface of the platinum nanoparticles upon application of a positive potential. By means of a cyclic voltammetry in acid and oxidizing solution (H_2SO_4), shown in figure 3.18, the amount of electroactive catalyst can be extracted. The integration of the broad peak in the potential region around +1.0 V gives a value of the integrated charge of 5 μC and it is used as the normalizing factor Q_{Pt} in the calculation of the turnover number. Since both HER and Pt oxidation are bi-electronic process, any further corrective factor has not been introduced in equation 3.9.
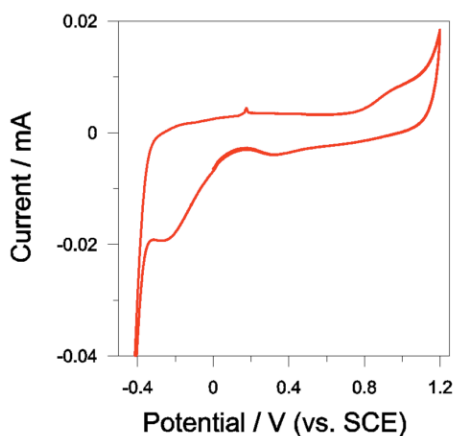
Figure 3.18: CV of the NMP-G Pt in H_2SO_4 0.05M. v = 0.05 V/s. The integration of the CV curve in the potential window 0.7 V - 1.2 V gives a charge of 5μC

In this way, we were able to normalize the efficiencies for the amount of electroactive platinum, having a precise quantification of the TON and TOF values in our experimental condition (0.1m phosphate buffer solution, pH 6.8). The linear relationship between TOF and overpotential (h) (figure 3.19 a) enables the extrapolation of the TOF_0 value, the turnover frequency at zero overpotential, which was proposed by Saveant and co-workers as an optimal

way to describe the intrinsic catalytic activity of different electrocatalysts.[149]

The TOFo value of approximately $4600 h^{-1}$ obtained for NMP-G Pt confirms the efficiency of our system and the usefulness of this approach towards the realization of high-performance carbon-based materials, functionalized with small amounts of active catalyst (e.g., noble metals).

The lower turnover frequencies measured for the commercial Pt/C catalyst ($TOF_0 \sim 1900 h^{-1}$, phosphate buffer solution 0.1 M, pH 6.8) are probably due to a different surface morphology for this material, which results in a relatively poorer accessibility to the catalytic sites as compared with the graphene-platinum nanoparticle composite.
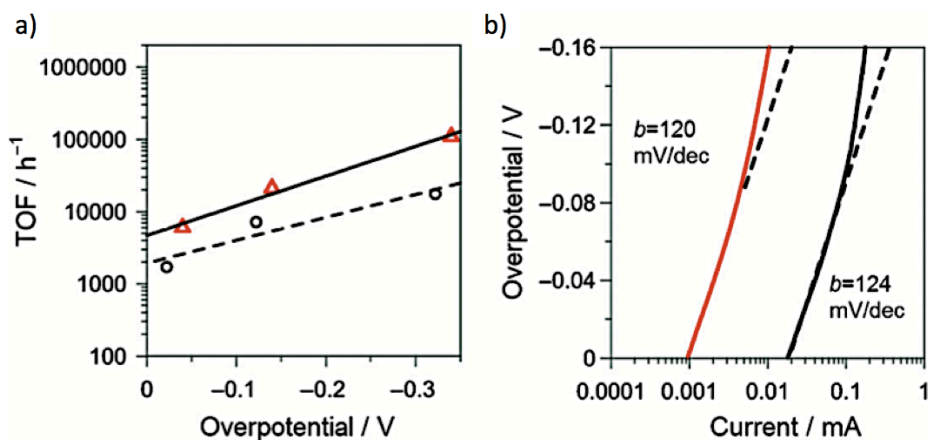
Figure 3.19: a) The linear relationship of turnover frequency (TOF) versus overpotential (η) for NMP-G Pt (red triangles) and Pt/C (black dots); η is calculated as $\eta = E - E_0 - I_s * R$, where $E°$ is the thermodynamic potential for the H^+/H_2 couple (vs SCE): $E°(V) = -0.24 - 0.06 * pH = -0.64 V$ and $I_s * R$ is the correction for the ohmic drop. b) Tafel plot for NMP-G Pt (red) and Pt/C (black), v=$2 mVs^{-1}$

Support of this hypothesis could be found in a Tafel analysis, which should be able to point out some possible differences in the mechanism of the HER due to a different availability of catalytic sites. However, Tafel plots of the low overpotential region for NMP-G Pt and Pt/C give the same slope of 120 mV dec[1] (figure 3.19 b), indicating the same reaction mechanism in both cases. This suggests that the surface morphology does not control the HER mechanism, but at the same time, the NMP-G Pt material is somehow able to maximize the catalysis,

probably due to the coupling of electronic effects between the platinum nanoparticles and the graphene substrate.

3.3.5 Conclusions

In conclusion, we have investigated the role of the exfoliation technique on the electrochemical properties of an hybrid material based on graphene and platinum nanoparticles. We adapted two conventional techniques to exfoliate graphene in order to perform the synthesis of PtNps in aqueous environment and we studied the effect of 1-pyrene carboxylic acid as stabilizing agent. We prepared therefore a graphene composite by means of an easy, low-cost and reproducible procedure that involves an NMP-based exfoliation process, enabling the formation of two-layer graphene flakes (NMP-G) that were selectively functionalized with PtNps (NMP-GPt). The electrochemical characterization of the material revealed that it is a promising electrocatalyst for the HER in light of its high frequencies of turnover; these values were obtained thanks to the optimal dispersion of the platinum nanoparticles onto the graphene substrate that enabled us to load the material with very small amounts of noble metal.

Chapter 3   Exfoliated Graphene decorated with platinum nanoparticles for electrocatalysis

Science never solves a problem without creating ten more.

George Bernard Shaw

4

Photoactive dendrimers for water photoreduction: a scaffold to combine sensitizer and catalyst

Here the synthesis of platinum nanoparticles templated by photoactive dendrimers is reported. The system was characterised by photophysical and TEM analysis to get some information about the morphology and the interaction between chromophores and platinum nanoparticles. Its efficiency towards the production of molecular hydrogen by water photoreduction was evaluated with the use of visible light and a sacrificial reagent. To the best of our knowledge, this system is one of the few reported in literature based on dendrimers for the water photoreduction, and the first one to combine sensitizer and catalyst into a singular dendritic molecular scaffold.

4.1   Water photoreduction: an overview

THE WATER SPLITTING REACTION has been already discussed in chapter 3, together with the thermodynamics of the hydrogen production. As already mentioned in the same chapter, enabling a fuel economy based on hydrogen is a major challenge. In addition to the electro-catalytic path, which requires the use of electricity, a more sustainable approach would be to produce hydrogen from renewable energy sources, such as sunlight, which is beyond a doubt one of the most available and widespread. It has been calculated that covering $\sim$0.16% of the land of the Earth with 10% efficient solar-conversion systems would provide 20 TW of power, nearly twice the world's consumption rate of fossil energy.[74]

As already explained in chapter 3, the thermodynamic requirements for splitting water are modest, being the Gibbs free energy of the endothermic barrier equal to $\sim$237 kJ mol^{-1}, corresponding to 1.23 V of electrochemical potential. In principle, any light source with a wavelength lower than $\sim$1μm is able to promote the water dissociation with no further energy input. Nevertheless, In contrast to what we observed for the electrocatalytic hydrogen production, the photochemical reactions also depends on how efficiently photons are absorbed and driven to the catalyst. Needless to say, water is not absorbing visible light, therefore the reaction needs a photo-catalytic system to take place. This system takes care of three fundamental processes:[150]

1. Solar light absorption by the light harvesting agent.

2. Redox potential generation due to charge separation and electron-hole transport.

3. Efficient enhancement of the Hydrogen evolution reaction and the Oxygen evolution reaction kinetics by proper catalysts.

Therefore the photo-catalytic system efficiency is closely related to several properties of the system components, such as (*i*) the absorption coefficient of the light harvester, (*ii*) the competition between charge separation and charge recombination efficiency, (*iii*) the activity of the catalyst in towards the reaction and (*iv*) the stability under working conditions to achieve long-lived systems.

According to the phase of the light absorbing specie and the catalyst, it is possible to distinguish between a pure heterogenous approach and an homogenous one or a hybrid hetero/homogenous approach.

In the pure heterogenous approach, a semiconductor with proper band alignment is typically used as light absorber and catalyst for both OER and HER. Usually, the semiconductors used for this application are not good catalysts, therefore they can be coupled to a catalyst in a photoelectrochemical cell[151] (Fig. 4.1 a) or in a micro-heterogeneus fashion[152] (Fig. 4.1 b). As already mentioned in Chapter 3, one of the best catalyst material for HER is known to be platinum. Again, the extremely high cost of the material represents the main bottleneck for the use of platinum as bulk electrode in a photoelectrochemical cell and the issue is now addressed by developing hybrid electrocatalytic materials as the graphene/Pt composite discussed in the previous chapter. The absorption of the radiation and the charge separation in the heterogenous system is usually handled by a semiconductor. The key points for these semiconductors are the charge mobility and the levels of the conduction and valence bands which, as shown in figure 4.1 c), has to be respectively more negative than the redox potential of H^+/H_2 (0 V vs. NHE), and more positive than the redox potential of O_2/H_2O (+1.23 V), depending on the product of interest.

This approach usually show very high efficiency and photostability, but the semiconductors used are often suffering from low absorption coefficient and scattering issues, therefore an organic sensitizer is often employed to capture as much sunlight as possible.[153]

A completely different approach is the homogeneous one, in which both the light harvester, called photosensitizer, and the catalyst are organic molecules or metal complexes able to transfer holes or electrons from the excited state. As for the semiconductors, the matching of the electrochemical potential of the sensitizer with the redox potential needed for water photoreduction is fundamental. For instance, a typically employed sensitizer as $[Ru(bpy)_3]^{2+}$ is showing a relatively small oxidation and reduction potential at ground state (about 1.29 V vs SCE for the reaction $[Ru(bpy)_3]^{3+} + e^- \longrightarrow [Ru(bpy)_3]^{2+}$) but it becomes a potent oxidant and reductant at the excited state (about -0.81 V vs SCE for the reaction $[Ru(bpy)_3]^{3+} + e^- \longrightarrow [Ru(bpy)_3]^{2+*}$).[154]

The best homogeneous catalysts are cobalt complexes[155],[156] but also other metal complexes has been investigated, such as Nickel[157] and Molibdenum.[158] This approach is surely intriguing
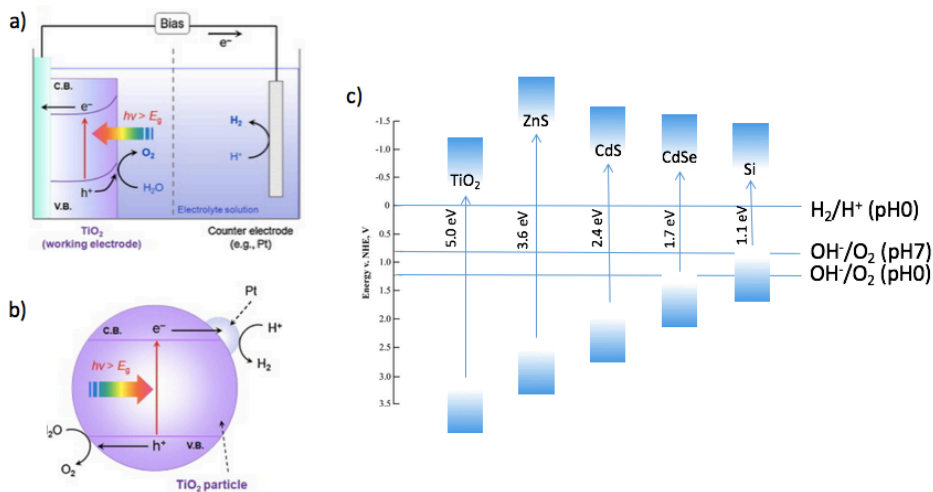
Figure 4.1: a)Photoelectrochemical water splitting cell using a TiO$_2$ photoanode, and b) a short-circuit micro-heterogenous model with the same components. c) Band structure of illustrative semiconductors with respect to redox potential of HER and OER.

because of the possibility to tune the photophysics and the catalytic activity by introducing new alternatives to photosensitizer and catalysts, though the efficiency and stability is not as high as colloidal platinum dispersions.

4.1.1 Microheterogeneous approach

FOR THIS REASON, an alternative approach could be based on exploiting on one side the interesting and well known photophysics of organic and organometallic sensitizers and, on the other side, the impressive catalytic activity of noble metals such as Platinum in a micro-heterogenous approach. Figure 4.2 is showing the typical scheme of a micro-heterogeneous water splitting system. It is possible to notice that the core of the system is the Photosensitizer (PS) that, upon irradiation with a visible light source, moves to an excited state more oxidizing than the ground state. The excited photosensitizer is then able accept an electron from an electron relay molecule (R) which, in turn, transfers an electron to the colloidal catalyts for the OER reaction. Then, the reduced Photosensitizer relaxes to the ground state by reducing a second electron relay molecule and again, by transferring this electron to the HER catalyst we
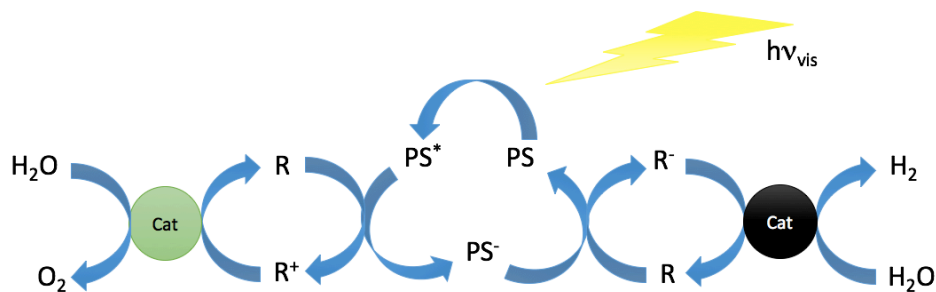
Figure 4.2: a)Photoelectrochemical water splitting cell using a TiO$_2$ photoanode, and b) a short-circuit micro-heterogenous model with the same components. c) Band structure of illustrative semiconductors with respect to redox potential of HER and OER. Energy levels of $[Ru(bpy)_3]^{2+}$ are reported for comparison in red.

complete the catalytic cycle. Actually, the complete catalytic cycle is very tricky and hard to analyze as it is, so often one of the semireaction is studied, as in our case the Hydrogen evolution reaction, by replacing the oxidative path with a sacrificial donor.

The most relevant features influencing the efficiency of the overall catalytic cycle are:

- The reductive trapping must occur faster than radiative or nonradiative relaxation of the sensitizer excited state.

- The sacrificial donor must be inexpensive and readily available.

- A robust catalyst for efficient evolution of hydrogen must be effective in trapping the reduced relay.

- Each of the intermediate charge relays must be stable in both the oxidized and reduced states so that the sensitizing dye can be multiply recycled.

Based on this pattern, several method have been developed and optimized, tuning either the photosensitizer, the catalyst or one of the electron relays. The first efficient example was proposed by Lenh and Sauvage in 1977,[159] using $[Ru(bpy)_3]^{2+}$ as sensitizer, Colloidal Pt as catalyst for the hydrogen production and Methylviologen as electron relay. This system needs also a sacrificial donor like triethanolamine, in order to replace the oxydative path and complete the catalytic cycle. Since then, the system has been optimized in several ways, by studying

different kind of photosensitizers, electron relays and sacrificial donors. The main drawbacks has been pinpointed as the kinetics of the back electron transfer to the photosensitizer and the limited stability of the electron relay, in addition to the low control on the synthesis of the catalyst, i.e. colloidal platinum. Complex structures at the nanoscale could give rise to new approaches to these issues, by providing nano-environments where the kinetics of the catalytic cycle could be strongly altered.

4.1.2   Dendrimers for solar energy conversion

The control of microenvironments as a function of the size, the nature and the disposition of the organic functionalities can be achieved thanks to a particular kind of structure called dendrimer. Dendrimers are molecular architecture possessing controlled dendritic branching with radial symmetry, resembling a tree-like structure.[160] The development of these complex structures has its roots in the idea of a "cascade" approach to synthesize branched oligomers reported by Vögtle et al. in 1978,[161] exploiting multi-functional unities to obtain a precise control on the size and the topology. The two most widely studied dendrimer families are the Fréchet-type[162] polyether based structures and the Tomalia-type[163] Polyamidoamine dendrimers (called PAMAM or Starbust), but several different architectures have been proposed based on transition metal complexes,[164] glycopeptides,[165] phenylene[166] or organosilicon[167] building blocks. Dendrimer's unique structure is based on three features:

1. A core, provided with three or more functionalities.

2. Interior layers of repeating units, again with more than two functionalities each, called generations (G).

3. An exterior surface functionality providing most of the chemical reactivity and solubility to the dendrimer itself.

This particular architecture inspired an extremely wide variety of applications based on dendrimers,[168] among which the solar energy conversion plays undoubtedly an important role. Indeed the tuning of the dendrimers functionalities represents an elegant way to arrange several photoactive molecules in a narrow space with a good degree of control, mimicking the wonderful example of solar energy conversion provided us by the natural photosynthesis. In

particular, the hierarchical shape of dendrimer's architecture resembles the one of the photo-synthetic system, where the solar radiation is absorbed by a series of peripheral antennae complexes and transferred to the reaction center through multiple energy transfer processes.[169] The first example of light-harvesting dendrimers based on Ru^{II} and Os^{II} polypyridine complexes as building blocks was reported by Balzani and co-workers in the early '90s;[164] after that, a discrete number of similar systems,[170] has been designed in order to optimize the kinetics of electronic processes from the core to the periphery of the dendrimer and vice versa.[171]

The addition of a catalyst for the hydrogen production within the dendrimer architecture opened the way to the photochemical production of hydrogen in such systems. The first example has been proposed by Mihara et al.[172] by combining 20 photosensitizer units (Zn^I-mesoprophyrins) with natural hydrogenase in a single peptide denrimer-like structure in an homogenous fashion. A microheterogeneous approach has been also investigated by encapsulating either Pt nanoparticles[173] or $2Fe_2S$ clusters[174] in, respectively, PAMAM and Fréchet type dendrimers and studying the kinetics of HER in a photosensitizer solution.

4.2 Pt nanoparticles templated by $[Ru(bpy)_3]^{2+}$ based Dendrimers

IN THIS FRAMEWORK, there is no example of systems directly encompassing both photosensitizer and heterogeneous catalyst into a single dendritic structure, in order to address several issues that are affecting the efficiency of the micro-heterogeneous water photoreduction. In particular Polyamidoamine (PAMAM or Starbust) dendrimers are known to spontaneously complex Pt^{2+} ions in solution, and by reducing the platinum ions inside the dendrimer it is possible to produce nanoparticles with an average size between 1 and 2 nm[175],[176] This results in the maximization of the catalytic efficiency, as already discussed in Chapter 3, and it allows to reduce the overall amount of platinum for equal efficiency. Moreover, by coupling the dendrimers surface functionalities with the $[Ru(bpy)_3]^{2+}$ complex (already mentioned as photosensitizer in the previous chapter) the diffusive encounter of photosensitizer and electron relay is no more necessary, because the dendrimer is already ensuring the intimate contact between PS and catalyst. In addition to this, the light harvesting efficiency of the system is also increased by the possibility of having multiple PS for each dendrimer, in our case up to 32.

Syntesis of Platinum nanoparticles and optical properties
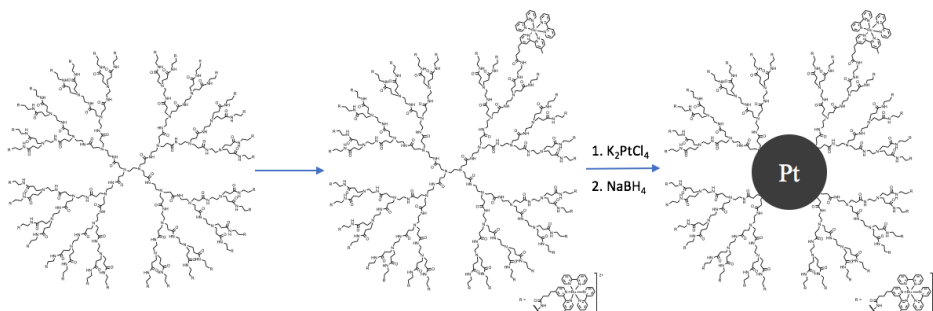
Figure 4.3: Scheme describing the synthetic paths

THE OUTLINE of the synthetic procedure is reported in Figure 4.3. The system is constituted by a fourth-generation polyamidoamine (PAPAM) dendrimer with 32 $[Ru(bpy)_3]^{2+} \cdot 2Cl^-$ metal complexes at the periphery (hereafter referred to as RuPAMAM). The dendrimer was kindly provided to us by Prof. Abruna, following the previosly reported procedure to couple PAMAM dendrimers with polypyridyl complexes[177].[178]

The photophysics of RuPAMAM were analyzed using UV-vis absorption and fluorescence spectroscopy in water environment (Fig. 4.4). The absorption spectrum of the dendrimer shows the typical band centered at 288 nm corresponding to the ligand centered transition (LC) and a band at 455 nm corresponding to the metal-to-ligand charge-transfer (MLCT) transition. The emission band is identical in position and shape (λ_{max} = 620 nm) to that of the free $[Ru(bpy)_3]^{2+} \cdot 2Cl^-$ complex in H_2O, but the emission quantum yield is half (0.014). This quenching of the fluorescence QY is probably due to electron transfer from the the amine moieties present in the skeleton of the dendrimer to the photoactive units.

The synthesis of the Platinum nanoparticles is following the same procedure described in Chapter 3. PAMAM dendrimers are particularly interesting as a template for metal nanoparticles, due to the spontaneous complexation of Pt^{2+} ions with the amine groups of the inner skeleton. The complexation is generally followed by absorption spectra, due to the lack of luminescent species, but in the case of RuPAMAM the luminescence of the Ru complex is strongly influenced by the amine groups, therefore the complexation might have some effects
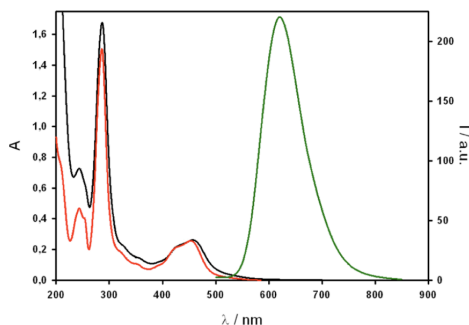
Figure 4.4: Absorption (black) and emission (green) of RuPAMAM in H_2O solution. For comparison, the absorption spectrum of free $[Ru(bpy)_3]^{2+} \cdot 2Cl^-$ in the same solvent has been reported (red).

on this property. Indeed, by titrating a RuPAMAM solution in H_2O with K_2PtCl_4 small variations of the absorption spectrum were observed (Fig 4.5 a), consisting in a small decrease of the MLCT band at 455 nm and the rising of a broad band increasing in the UV-region (at wavelengths below 400 nm). More pronounced changes were observed in the emission spectra upon excitation at an isosbestic point ($\lambda_{exc} = 375$ nm) shown in figure 4.5 b): the emission intensity at 620 nm, related to the Ru complex, gradually decreases up to 80% upon adding the Platinum salt. The increasing quenching could be ascribed to a new non-radiative process, namely an energy or electron-transfer, between the ^{3}MLCT band of the Ru complex and the freshly formed Pt-amine complex. The titration reaches a plateau after ~20 eq. of K_2PtCl_4 with respect to RuPAMAM concentration. Therefore, for the first time, the stoichiometry of the Pt^{2+} complexation with the dendritic ligand was relatively easily followed through emission spectra.

After following the complexation, the synthesis of the platinum nanoparticles has been performed by chemical reduction of the Pt^{2+} with sodium borohydride ($NaBH_4$). One equivalent (with respect to Pt^{2+}) of $NaBH_4$ in water was added to a solution of RuPAPAM with 20 equivaltens of Pt^{2+} per dendrimer, in order to minimize the quantity of platinum ions outside the dendrimers. A slight excess of $NaBH_4$ was actually necessary due to the spontaneous reaction of $NaBH_4$ with water, which is decreasing the efficiency of the reducing agent. The solution was left under agitation for 24h and no sign of precipitation was observed. By observing the absorption spectra shown in figure 4.6 a) before and after the reduction step, it
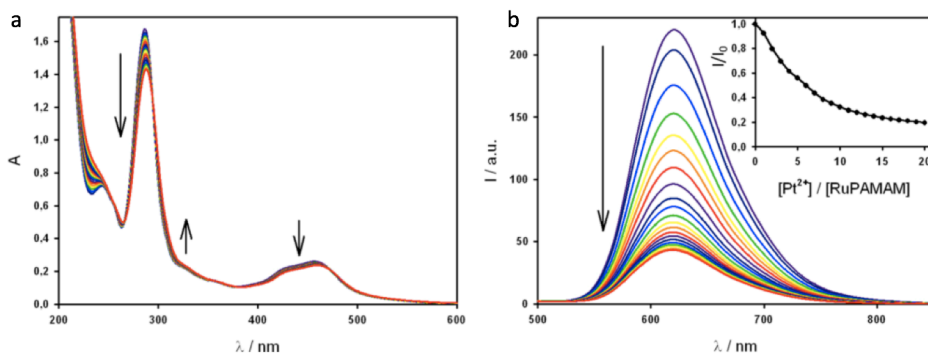
Figure 4.5: a) Absorption spectra and b) emission spectra of a $1.47 \cdot 10^{-6}$ M solution of RuPAPAM in H$_2$O upon titration with K$_2$PtCl$_4$. The inset shows the normalized emission intensity changes at 620 nm (λ_{exc} = 375 nm).

is possible to notice no variation of the typical features of the $[Ru(bpy)_3]^{2+}$ complex, meaning that the photoactive unit is not affected by the addition of the reducing agent. At the same time, a slight increase of the baseline is recorded, sensibly higher in the near-UV region, corresponding to the scattering effect induced by the formation of the stabilized nanoparticles.[179]
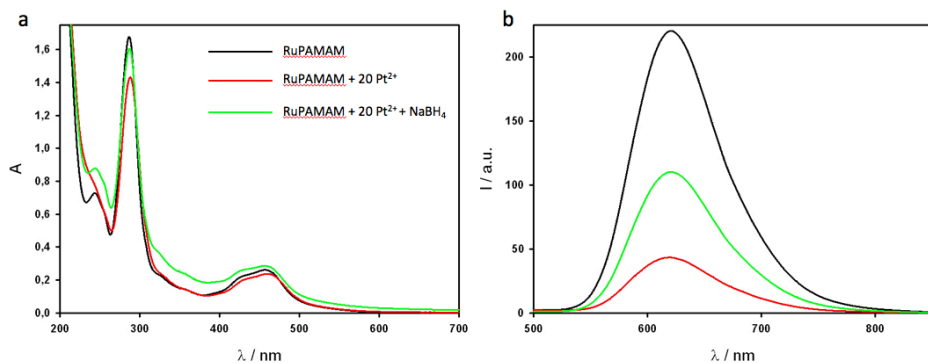
Figure 4.6: a) Absorption and b) emission spectra of RuPAMAM $1.47 \cdot 10^{-6}$ M in H2O (black), after addition of 20 eq of K$_2$PtCl$_4$ (red) and after reduction with NaBH$_4$ (green).

As observed for the complexation, the emission spectra are much more influenced by the reduction process. As shown by figure 4.6 b), upon adding NaBH$_4$ to the RuPAMAM so-

lution, the emission intensity is increasing partially restoring the initial emission intensity observed before the addition of the Pt^{2+} complex. While the Pt^{2+} coordination to the amine functionalities of the dendrimers was previously observed to quench the emission of the surface $[Ru(bpy)_3]^{2+}$ complexes, the same is known not to be happening after the reduction of platinum ions to nanoparticles. Therefore, by comparing the emission intensity of the Ru-PAMAM after the reduction of Pt^{2+} with the one observed before the addition of the same platinum ions, it is possible to estimate the number of amine coordinated Pt^{2+} ions reduced by Sodium Borohydride, which was found to be $\sim$40%. Hereafter, to indicate the system Ru-PAMAM containing the platinum nanoparticles, the acronym RuPAMAM/PtNps will be used.

4.2.2   Morphological and compositional characterization

THE DIMENSIONAL, morphological and compositional analysis of the produced nanoparticles was performed by TEM and STEM-EDS. Details on the technique and the instrumentation are reported in Appendix B. Figure 4.7 a) displays a STEM-HAADF micrograph in which, being the contrast typically proportional to the atomic number, the Platinum nanoparticles pop out very clearly as bright white dots. From STEM images the diameter distribution of the platinum nanoparticles was extracted and the average value was found to be equal to 1.3 $\pm$ 0.3 nm, as reported in figure 4.7 b). It has to be noticed that the average value and the polydispersity is lower compared to the one observed in Chapter 3, due to the templating effect exerted by PAMAM dendrimers. From the size distribution, an estimation of the number of atoms per nanoparticles was performed, that is essential for the evaluation of the catalytic activity of the nanoparticles towards water photoreduction. The average radius obtained from the HRTEM analysis is 0.65 nm, and assuming the nanoparticle as a sphere the volume is 1.15 x 10^{-21} cm³. Considering a density of the platinum of 21.45 g/cm³, a mass of 2.47 x 10^{-20} g can be obtained, and the number of moles equal to n = 1.26 x 10^{-22} mol. Multiplying the moles by the Avogadro's number, the average number of platinum atoms per nanoparticles results in 76 Pt/Np. This value is definitely higher than the number of Pt atoms involved in the dendrimer complexation and the reduction process, which was calculated to be $\sim$20. This result suggests that the particle formation involves at least the cooperation of three different dendrimers, not much for the dimension but for average number of platinum per nanoparticle.
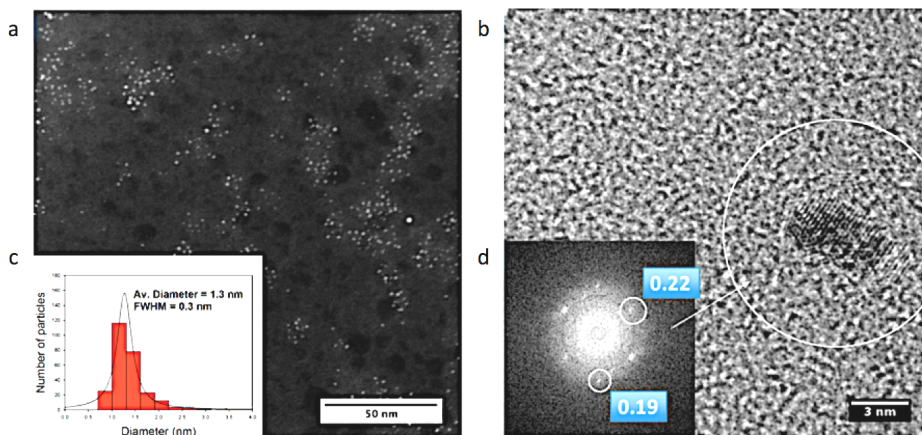
Figure 4.7: a) STEM image of RuPAMAMPtNps on holey carbon film copper grid. c) Histograms showing the PtNps size distribution. b) HR-TEM image and fast Fourier transform d) of a single nanoparticle.

TEM micrographs like the one displayed in figure 4.7 c), are showing quasi-spherical nanoparticles that exhibit diffraction fringes confirming the composition of the nanoparticle as pure platinum. Indeed the interplanar distances observed through the Fast Fourier Transform of the TEM image (reported in figure 4.7 d) correspond to the one of metallic Pt crystal lattice in the (1,0,1) direction. A more straightforward compositional analysis was performed by coupling the STEM imaging techinque with EDS spectrum. Thanks to the higher magnification of the STEM micrograph in figure 4.8 a), it is possible to notice both the presence of the bright spots, corresponding to the Pt nanoparticles, and a lighter halo surrounding the nanoparticles. From the low contrast of the halo, we can only say that the atomic number must be lower than the one of platinum. By performing an EDS profile along the orange line displayed on the same micrograph we obtained the graph reported in figure 4.8 b), where the amount of Platinum and Ruthenium is increasing by moving along the material, compared to the signal obtained on the substrate for the same two elements. This means that the signal of Ruthenium is effectively located around the nanoparticles, confirming the embedding of PtNps by RuPAMAM dendrimers. Furthermore, the halo surrounding the nanoparticles is clearly much bigger than the expected diameter of a single dendrimer, confirming the cooperative stabilization of multiple dendrimers for each
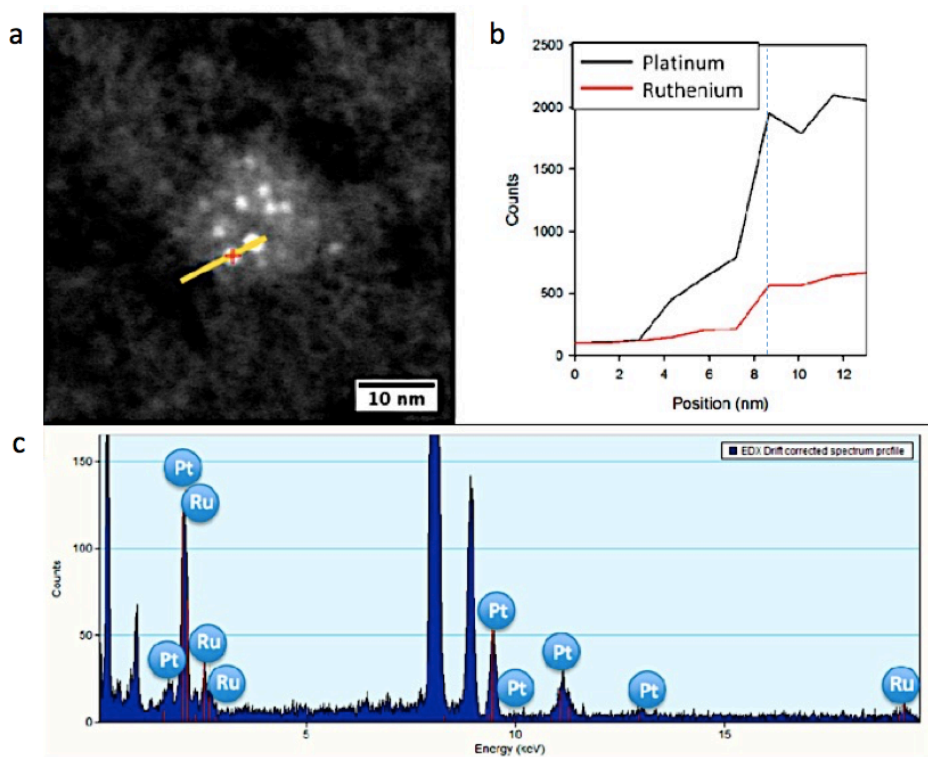
Figure 4.8: a) STEM micrograph of a dendrimer aggregate including several platinum nanoparticles. b) EDX profile taken along the yellow line reported in panel a. c) EDX spectrum relative to the platinum nanoparticle highlighted with the red cross in panel a), corresponding to the point of the profile highlighted by the blue dashed line in panel b).

nanoparticle.

4.2.3 Water photoreduction efficiency evaluation of RuPAMAM/PtNps

IN ORDER TO EVALUATE the photocatalytic performance of the system towards water photoreduction, the use of a sacrificial electron donor is mandatory. Ascorbic acid has been previously used to this aim with success by Balzani et al.[180] and it is suitable to experiments in slightly acid environment (pH 5). We performed the experiment at this specific pH value because of several reasons, such as:

1. pH values lower than 5 may protonate the amine functionalities of PAMAM dendrimers, thus determining the release of Pt nanoparticles and residual Pt^{2+} ions from the core.

2. Being the thermodynamics of the HER strongly influenced by the pH value, too basic pH increases the energy barrier for the reaction.

3. pH 5 is high enough for almost complete deprotonation of ascorbic acid (pKa = 4.17 at 298 K) to favor reductive quenching of the ruthenium(II) sensitizer.

The hydrogen evolution was studied upon continuous irradiation with visible light of an argon-purged 1.6 μM aqueous solutions of RuPAMAM/PtNps at pH 5 in the presence of 0.1 M ascorbic acid and monitoring the gas phase of the reactor by GC. Details on the setup are reported in Appendix C. A control experiment was performed in which the sensitizer was added externally as $[Ru(bpy)_3]^{2+}Cl_2 \cdot H_2O$ to a solution of Pt nanoparticles encapsulated in non-functionalized PAMAM dendrimers. To do so, the same aforementioned synthetic path to produce platinum nanoparticles was followed in presence of commercially available PAMAM-OH dendrimers in water environment. After checking that the morphology of the nanoparticles was consistent of the one of RuPAMAM/PtNps by TEM analysis, the water photoreduction experiment was performed in a 2.1μM water solution of PAMAM/PtNPs in presence of 0.1M ascorbic acid at pH 5.

The performance of the two systems is reported in figure 4.9. It is evident how the efficiency of the RuPAMAM/PtNps system is strongly higher than the one observed for the

system with decoupled catalyst and sensitizer. While for the last one the photocataytic activity is almost zero in the whole time window, the RuPAMAM/PtNps show a steep increase in the first 2 hours of experiment, and slowly reaches a plateau after 4 to 5 h of irradiation, achieving up to 95 nmol of hydrogen. According to the calculation previously reported, 5 ml of a 1.6 μM RuPAMAM/PtNps solution corresponds to an overall average value of 1.51 nmol of Pt nanoparticles. By simply dividing the amount of hydrogen produced for the concentration of Pt nanoparticles, it is possible to estimate the turnover number of the photocatalytic process equal to 63. The maximum rate of hydrogen production, calculated in the linear part of the kinetic, is 67.2 nmol h^{-1}, corresponding to a turnover frequency (TOF) of 44.5 h^{-1} per Pt nanoparticle.

Although different experimental conditions were used, comparison of the hydrogen evolving activity with supramolecular systems involving a ruthenium(II) polypyridine dye and a molecular catalyst shows that the present system displays TONs in line with those reported for Ru/Pd (TON = 56 after 29 h of irradiation),[181] Ru/Rh (up to 60),[182] and Ru/Co (TON = 105 after 15 h)[183] dyads and considerably higher with respect to that for a related Ru/Pt one (TON = 4.8 after 10 h).[184]
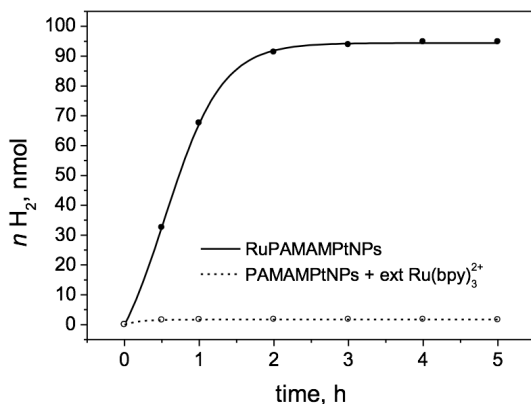
Figure 4.9: Photocatalytic hydrogen evolution obtained upon continuous visible irradiation of a pH 5 water solution containing 1.6 μM RuPAMAM/PtNps and 0.1 M ascorbic acid (solid circles, solid line) and 34 μM $[Ru(bpy)_3]^{2+} Cl_2 \cdot H_2O$, 2.1 μM PAMAM/PtNps, and 0.1 M ascorbic acid (open circles, dashed line).

This evidence seems to suggest that an intimate contact between the sensitizer and the cata-

lyst is required for efficient hydrogen generation. In particular, the dendrimer scaffold seems to act as a shield for the Pt nanoparticles, likely preventing or at least limiting bimolecular electron transfer to occur. Therefore, only when the ruthenium-(II) sensitizer is directly connected to the catalytic site in the dendrimer supramolecule, electron transfer from the photo-generated reduced sensitizer can take place as an intramolecular process, thus contributing to hydrogen production.

Anyway, the mechanism behind the efficient photocatalytic cycle is not indipendent on the nature of the sacrificial donor. Indeed the Pt nanoparticles confined in the PAMAM dendrimers are not capable of quenching the ^{3}MLCT excited state of $[Ru(bpy)_3]^{2+} \cdot 2Cl^-$, as observed by the recovery of the ruthenium-based emission after the reduction of the platinum precursor with $NaBH_4$, as previously discussed. On the basis of previously reported homogeneous systems for hydrogen generation involving a ruthenium(II) trisbipyridine sensitizer and ascorbic acid sacrificial donor,[185] hydrogen production is likely to take place by first bimolecular reductive quenching of the sensitizer moieties by the ascorbic acid donor, with a bimolecular rate constant of about 107 $M^{-1} s^{-1}$.[186] This step may be then followed by intramolecular electron transfer to the Pt nanoparticle catalyst for the HER reaction.
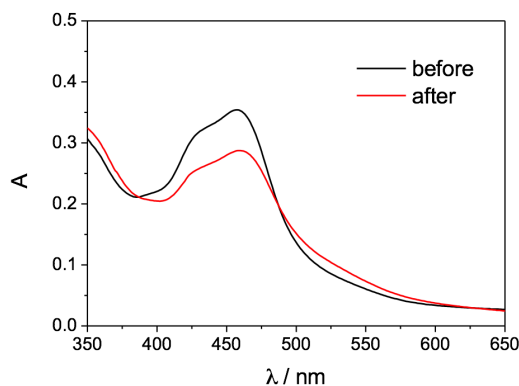
Figure 4.10: Comparison of absorption spectra before and after (5 h) irradiation of a pH 5 water solution containing 1.6 μM RuPAMAM/PtNps and 0.1 M ascorbic acid.

The saturation of the photocatalytic activity after a relatively short time can be explained by observing the absoprtion spectrum of the sensitizer after the irradiation. The comparison of the spectra before/after photolysis (Figure 4.10) suggests that partial decomposition of the

sensitizer occurs. This may be related to unproductive routes involving the photogenerated reduced form of the sensitizer and competing with electron transfer to the Pt nanoparticles.[185]

4.2.4 Conclusions

IN CONCLUSION, we have synthesized very small and monodisperse platinum nanoparticles embedded in PAMAM dendrimers decorated by $[Ru(bpy)_3]^{2+}$ chromophores. The use of a photosensitizer covalently coupled to the terminal functionalities of the dednrimer allowed us to thoroughly follow the complexation and the reduction of Pt^{II} ions. The ruthenium complex acts therefore as phosphorescent signaling units to estimate the number of platinum ions hosted and photosensitizers in the light-induced water reduction process in the presence of a sacrificial electron donor. The advantage of using photoactive dendrimers is the possibility to easily replace the catalyst hosted in the supramolecular structure,[174] and, because of the versatility of the dendrimer chemistry, also the photo-and redox properties can be tailored by coupling different sensitizers. Up to our knowledge, this is the first example of a system in which both photosensitizer and catalyst are anchored to a unique dendritic structure. We hope that this study will provide a innovative approach in the development of artificial photosynthesis based on intra-molecular processes by using photoactive dendrimers.

5

Conclusion

The *trait d'union* of this thesis has been to catch and take advantage of the peculiar properties of a wide class of cutting-edge nano-materials in different energy conversion applications. The interesting properties of these materials, such as graphene, silicon nanocrystals and platinum nanoparticles, have been proved to provide a substantial contribution to different applications, from photovoltaics to hydrogen production.

In the first part of the thesis, the light harvesting in pyrene functionalized silicon nanocrystals has been discussed, suggesting an original approach to successfully increase the absorption properties of these nanocrystals. Moreover, the interaction of these nanocrystals with carbon allotropes has been studied, in order to give a deeper insight on the charge and energy extraction, preparing the way to implement SiNCs as active material in optoelectronic devices and photovoltaic cells. Finally, the luminescence of SiNCs has been exploited to increase the efficiency of conventional photovoltaic cells by means of two innovative architectures. Specifically, SiNCs has been used as luminescent downshifting layer in dye sensitized solar cells, observing an increase of the efficiency of the cell upon the addition of a nanocrystal layer. In

addition to this, SiNCs have shown to be very promising as light emitters in luminescent solar concentrators thanks to the good quantum yield, the photophysical tunability and the high Stokes-shift that allows to minimize the re-absoprtion issue that is affecting most of the commonly used fluorophores.

The second part of the thesis focused on the production of hydrogen by platinum nanoparticles coupled to either electro-active or photo-active materials. Within this context, the electrocatalytic activity of platinum nanoparticles supported on exfoliated graphene has been studied, preparing an high-efficiency catalyst and disclosing the role of the exfoliation technique towards the catalytic activity. Furthermore, platinum nanoparticles have been synthesized within photoactive dendrimers, providing the first proof of concept of a dendrimer-based photocatalytic system for the hydrogen production where both sensitizer and catalyst are anchored to a single scaffold.

With the work carried out and discussed in this thesis, we hope to provide a significant contribution to the investigation of the properties of innovative nano-materials for energy conversion. We believe that the reported systems will play an important role in the development of new techniques for a more efficient and widespread exploitation of renewable energies.

A

Photophysical characterization

All solution phase experiments were performed at room temperature in 1 cm optical path quartz cuvettes; high purity Uvasol® solvents were used. Experiments in de-oxygenated atmosphere were performed in a modified quartz cuvette provided with vacuum manifold compatible stopcock and PTFE valve. Freeze-pump-thaw cycle is performed reaching an internal pressure lower than $1x10^{-7}$ mbar thanks to a diffusive pump.

A.1 Electronic absorption spectra

Electronic absorption spectra have been registered by UV/Vis double beam spectrophotometer Perkin Elmer® Lambda 650, using a quartz cuvette filled with pure solvent as reference. The instrumental setup is schematized in figure A.1 a). This kind of measure indentifies electronic transition of molecules from their fundamental state, called S_0 to excited states; moreover, it is possible to measure the molar absorption coefficient ($\varepsilon [M^{-1}cm^{-1}]$ through the Lambert-Beer equation:

$$A = \varepsilon bc \tag{A.1}$$

Where A is the absorbance (adimensional); b is the optical path length (in cm) and c is the molar concentration of the sample.
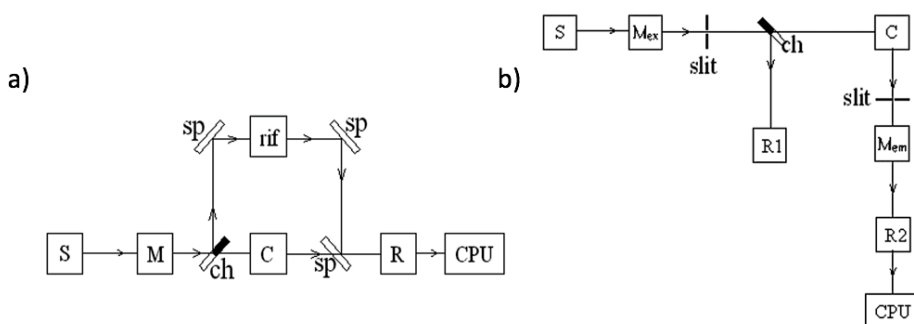
Figure A.1: a) Spectrophotometer scheme where S=light source (a tungsten lamp operates between 900 and 320 nm, while an Hydrogen one works between 320 and 190 nm); M=monochromator (diffraction grating); C= Sample; rif= reference; R= detector (photo-multiplier tube) ch=chopper; Sp= mirrors; CPU= computer. b) Spectrofluorimeter scheme. S=light source (Xe 2μs pulsed lamp); M=monochromators (diffraction grating); C= Sample; R1= reference detector to correct lamp emission; R2 = detector (photo-multiplier tube) ch=chopper; CPU= computer

A.2   Emission and excitation spectra

Emission and excitation spectra in the UV-Vis region have been registered by Perkin Elmer® LS55 spectrofluorimeter, which optical scheme is represented in figure A.1 b). This instrument is able to detect radiative transitions between an excited state (usually lowest energy one) to the ground state. Moreover, tuning the delay time and between lamp pulse and detection and the gate interval, fluorescence and phosphorescence may be splitted and recognized.

Emission spectra are characterized by a fixed excitation wavelength, while emission monochromator scans emission wavelenghts; excitation spectra, on the opposite, are taken fixing an emission wavelength but tuning excitation ones. Furthermore, a correct excitation spectra must be registered on the so-called linearity interval, that means the sample solution must have to show Absorbance under 0.1 in the whole absorption spectrum, be-cause only for little values of absorbance the dependence of the emission intensity can be approximated as linear.

Emission spectra in the NIR region were also registered on a Edimburgh F900 spectrofluorimeter by means of a high sensitivity Ge detector equipped with a liquid nitrogen cooling system. The signal acquisition is performed by a lock-in amplifier connected to a chopper in order to maximize the signal to noise ratio.

A.2.1 Fluorescence correction on the absorption

The fluorescence intensity registered with a spectrofluorimeter is intrinsically a relative value, because no reference signal is available. Exploiting the relation between Absorbance and Transmittance, it is possible to define the emission intensity I_{em} as a function of the incident light I_0 and the absorbance of the sample:

$$I_{em} = I_0 (1 - 10^{-A}) \tag{A.2}$$

If the emission intensity of a sample containing an absorbing quenching specie has to be compared with the emission intensity of the same sample in absence of that specie, its value has to be normalized on the amount of light absorbed by the emitting specie, because part of the incident light is subtracted by the quenching specie. This correction can be made by applying of the following relation:

$$I_{corr} = \frac{I_{mix}}{I_0} \frac{A_{mix}}{A_0} \frac{1 - 10^{-A_0}}{1 - 10^{-A_{mix}}} \tag{A.3}$$

Where *mix* stands for the mixture of emitting specie and quencher while 0 stands for the emitting specie in absence of the quencher.

A.3 Photoluminescence quantum yield evaluation

The photoluminescence quantum yield is defined as the ratio between the number of emitted photons and the number of absorbed photons $\phi = \dfrac{I_{em}}{I_{abs}}$. This value can be measured either with an absolute method or a relative method, using species with a known ϕ as reference. Here the two methods are briefly described:

A.3.1   Absolute Quantum yield

The Absolute Quantum yield is measured in a conventional spectrofluorimeter provided with an integrating sphere (Spectraflect® $BaSO_4$ internal layer, 96-98% reflectance between 300-2400 nm, 4" diameter) by means of the De Mello method.[187] This method consists in registering 5 spectra of the sample in different conditions:

- A_1 - Emission spectrum at the excitation wavelength of the blank (no sample).

- B_1 - Emission spectrum at the excitation wavelength of the sample away from the exciting beam.

- B_2 - Emission spectrum of the sample away from the exciting beam.

- C_1 - Emission spectrum at the excitation wavelength of the sample hit by the exciting beam.

- C_2 - Emission spectrum of the sample hit by the exciting beam.

The quantum yield, or external quantum efficiency (EQE) is then calculated by comparing the emission intensities with the following formula, after taking into account the correction for the detector response and for the transmittance of the cutoff used during the measurement:

$$\eta = \frac{C_2 - (1 - A)B_2}{A_1 A} \tag{A.4}$$

Where A is equal to $(1 - \frac{C_1}{B_1})$. The η of samples emitting in the NIR region was calculated by normalizing the different response of the Visible and NIR detector by means of a standard emitting in the spectral region between 700-900 nm (e.g. HITCI as showed in the next paragraph).

A.3.2   Relative Quantum yield

The relative quantum yield of a luminescent specie can be measured by preparing a solution of the sample and a solution of the reference with similar absorbance at the chosen excitation wavelength. The ϕ value can be exctracted by the following equation:[188]

$$\phi = \phi_{ref} \frac{I}{I_o} \frac{A_o}{A} \frac{n^2}{n_o^2} \tag{A.5}$$

Where I is the integrated emission intensity of the sample over a chosen spectrum interval, I_o is the integrated emission intensity of the luminescent standard over the same spectrum interval, A is the absorbance of the sample at the excitation wavelength, A_o is the absorbance of the standard at the same excitation wavelength, n and n_o the refractive index of respectively the sample and the standard solvents. The choice of the reference is related to the excitation wavelength, the emission interval and the expected value of quantum yield.[189] In Chapter 1 and 2, the ϕ of SiNCs was calculated using two different standards, depending on the size of the nanocrystal:

- for the 3 nm size nanocrystals, $Ru(bpy)_3^{2+} \cdot 2Cl^-$ in air-equilibrated water was used as reference (ϕ=0.040[190]).

- for the 3 nm size nanocrystals, 1,1',3,3,3',3'-hexamethylindotricarbocyanine iodide (HITCI) in air-equilibrated ethanol was used as standard (ϕ=0.30[191]).

A.4   Ecited state lifetime measurement

A.4.1   Nanosecond range

The nanosecond range lifetimes have been measured with the Single photon counting technique on a Edimburgh Instruments F900 Single photon counting spectrofluorimeter. The instrument setup is reported in figure A.2. For a typical measurement, each pulse emitted by the light source starts a time cycle whose duration is selected a priori and always lies within two consecutive pulses. The stop detector, usually a high gain photomultiplier or a microchannel plate, displays an electric signal when hit by the first (unique) photon; this pulse stops the time cycle initiated by the start signal; then the detector quits until a subsequent start signal begins a new excitation-emission cycle. The final electronic system incorporates two Constant Fraction Discriminators (CFD), a Time-to-Amplitude Converter (TAC), and a Multi-Channel Analyzer (MCA). The two CFD, one for start and one for stop signal, do not allow the cycle to be considered when one of the two signals (mainly the stop) do not reach a treshold value, in order to reduce dark current effects. The TAC is the heart of the instrumentation and it works like a stopwatch: the TAC measures, within a single excitation-emission cycle, the time difference between the stop and the start signals, i.e. the delay between the exciting photons
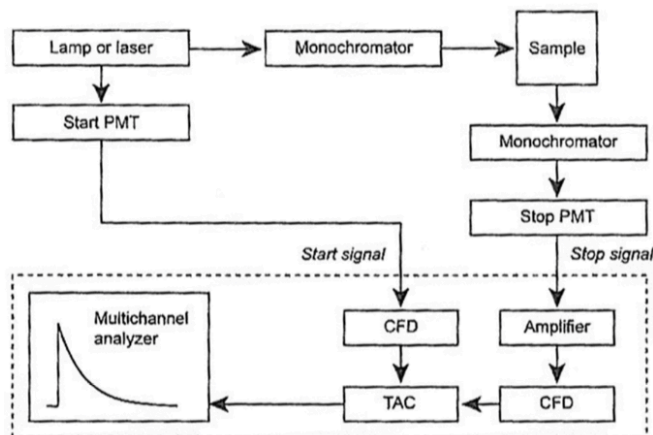
Figure A.2: Single Photon counting spectrofluorimeter scheme.

(start signal) and the single photon causing the stop signal. Finally MCA receives the time delay from TAC and organizes them in a plot showing the number of times that a single photon is seen by the detector at a given interval of Δt. The emission slits have to be tuned in order to ensure a stop/start signals ratio is equal to 0.02, in order to provide each photon with the same probability to be seen independently of the emission moment.

A.4.2 Microsecond range

The microsecond range lifetimes have been registered with the gated sampling method on a conventional spectrofluorimeter. This method is based on measuring the emission intensity of the sample at an increasing delay with respect to the excitation. The temporal resolution of the technique is depending on the delay time and the gate of each intensity acquisition. For a conventional SiNCs sample, the delay is set to 10 μs and the gate time is 40 μs in order to increase the signal intensity.

B

Structural and morphological characterization

B.1   Scanning electron microscope

The SEM images displayed in Chapter 1 were recorded by a Zeiss Leo Gemini 1530 equipped a Schottky emitter and a high efficiency in-lens electron detector. The instrument is operated at an accelerating voltage of 5 kV in order to maximize the morphological contrast of thin nanomaterials. The samples are supported on a conventional SEM stub and sticked with carbon tape to ensure a good electrical contact.

B.2   Transmission electron microscope

HR-TEM and STEM-HAADF micrographs were recorded on a FEI Tecnai F20T TEM equipped with a Schottky emitter and operated at 120kV to minimize beam induced damage in low atomic weight materials. The TEM is provided with a Gatan MSC794 CCD camera,

Fischione High Angle Annular Dark Field STEM detector and double tilt specimen holder. Compositional analysis of the samples is possible thanks to an attached EDAX EDS X-ray spectrometer PV9761 with Super Ultra thin window. The information limit provided by this instrumental setup is equal to 0.14 nm, while the point resolution in TEM mode (Scherzer defocus) is equal to 0.24 nm and the one in STEM mode is 0.19 nm. Figure B.1 displays the
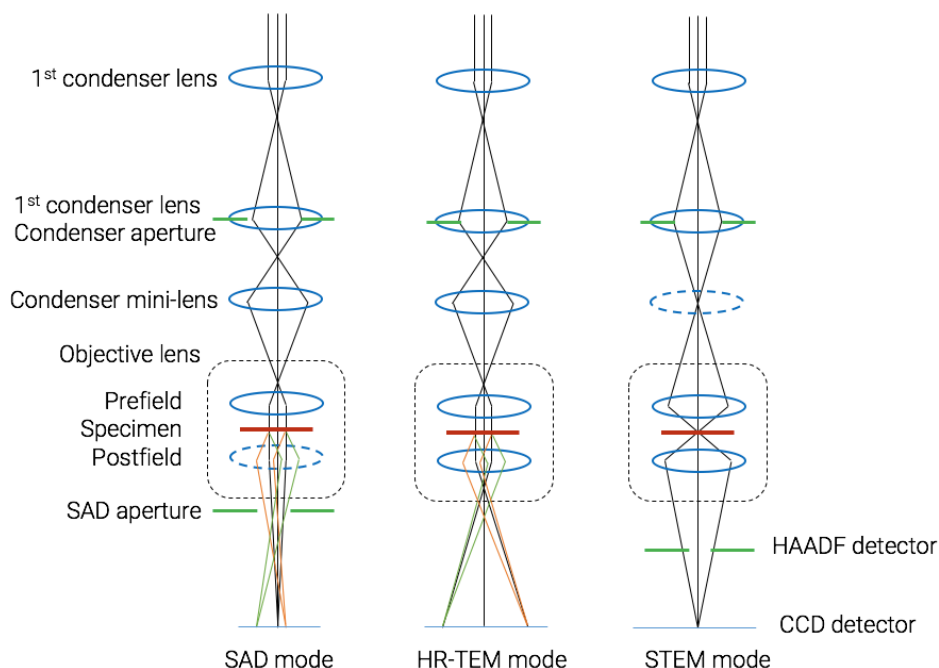
Figure B.1: Schematic representation of a TEM column in different working modes.

different optical setups employed to obtain a) selected area diffraction (SAD or SAED), b) high resolution micrographs (HR-TEM or HREM) and scanning transmission micrographs (STEM). Further details on the theory of the TEM working modes can be found in.[192] The samples are usually prepared by drop casting of few drops of the sample solution on carbon coated copper TEM grids. The shape of the carbon film is chosen depending on the expected size and shape factor of the material of interest. The solvent is then removed by vacuum pumping the grid or, when the material is not heat sensitive, by rapid heating over the solvent boiling point.

B.3   AFM and KPFM

The AFM and KPM measurements were performed using an AFM Enviroscope system from Veeco Instruments (now Bruker), equipped with Pt-coated tips (ANSCM-PT , Applied Nanostructures), with a tip radius at the apex below 20 nm. KPM was implemented using a PLLproII controller from RHK Technology. We used a double modulation scheme, mechanically oscillating the cantilever at its first (fundamental) resonance (around 55 kHz, tip-dependent) for topography imaging, while the second resonance ($\sim$410 kHz) was used for electrostatic modulation, as previously described.[193] Both topography and surface potential (CPD) were measured simultaneously, in a single pass. We did not use a double-pass technique, since preliminary experiments showed worsening of the lateral resolution when using lift mode. The amplitude of the AC modulation was 0.5 V. Both the nulling bias and the AC modulation were applied to the sample, and therefore the tip-sample contact potential difference CPD equals the nulling bias.

C

Supplementary techniques and characterization

C.1 H-NMR and ESI-MS characterization of pyrene derivatives

1H-NMR and 13C-NMR spectra were recorded on Varian INOVA 400 (400 MHz) spectrometers. Chemical shifts are reported in ppm using tetramethylsilane as the internal reference standard. Data are reported as follows: chemical shift, multiplicity (s = singlet, d = doublet, t = triplet, q = quartet, br = broad, m = multiplet), coupling constants (Hz).LC-electrospray ionization mass spectra were obtained with an Agilent Technologies MSD1100 single-quadrupole mass spectrometer.

C.1.1 1-(allyloxymethyl)pyrene characterization

^{1}H-NMR (400 MHz, CDCl$_3$) δ:8.38 (d, J = 9.2 Hz, 1H); 8.23-8.20 (m, 2H); 8.17-8.13 (m, 2H); 8.08-8.03 (m, 4H); 6.21-6.14 (m, 1H); 5.51 (dd, J1 = 1.6 Hz, J2 = 1.6 Hz, 1H); 5.39 (dd, J1 =

1.6 Hz, J_2 = 1.6 Hz, 1H); 5.24 (s, 2H); 4.25-4.23 (m, 2H).

^{13}C-NMR (100 MHz, CDCl$_3$) δ:134.9, 131.4; 131.3; 131.2; 130.8; 129.2; 127.6; 127.4; 127.3; 126.8; 125.8; 125.2; 125.1; 124.9; 124.7; 124.5; 123.3; 117.3; 71.2, 70.6.

ESI-MS : 232 $[M\text{-}Cl_3Hl_5]^+$

C.1.2   1-((undec-10-enyloxy)methyl)pyrene characterization

^{11}H-NMR (400 MHz, CDCl$_3$) δ: 8.41 (d, J = 9.2 Hz, 1H); 8.24-8.20 (m, 2H); 8.19-8.14 (m, 2H); 8.10-8.04 (m, 4H); 6.02-6.04 (m, 1H); 5.23 (s, 2H); 5.08 (d, J = 17.2 Hz, 1H); 5.03 (d, J = 10.4, 1H); 3.64 (t, J = 6.4 Hz, 2H); 2.13-2.07 (m, 2H); 1.75- 1.69 (m, 2H); 1.42-1.40 (m, 4H); 1.53-1.30 (m, 8H).

^{13}C-NMR (100 MHz, CDCl$_3$) δ: 139.0, 131.7; 131.1; 131.0; 130.6; 129.1; 127.3; 127.2; 127.0; 126.6; 125.6; 124.9; 124.7; 124.6; 124.2; 123.3; 114.0; 71.2; 70.3; 33.7; 29.7; 29.4; 29.3; 29.0; 28.2; 26.1.

ESI-MS : 407 $[M + Na]$; 215 $[M\text{-} Cl_{11}Hl_{21}O\,]^+$

C.2   ATR FT-IR characterization of SiNCs

The ATR FT-IR spectra (400-4000 cm^{-1}) were recorded using a Bruker Alpha FT-IR spectrometer with an ATR (attenuated total reflectance) attachment. Samples were prepared by drop casting from CHCl$_3$ dispersions, followed by vacuum drying.

C.3   XPS characterization of SiNCs

X-ray Photoelectron Spectroscopy was performed on a Kratos XPS spectrometer equipped with a charge neutralizer and 180° hemispherical electron energy analyzer. XPS samples were prepared by dropcasting Si nanocrystals onto ITO coated glass substrates and degassed at 10^{-7} Torr for 1 day prior to analysis. XPS data were internally standardized with respect to the O$_{1s}$ peak position (530 eV).

C.4 XRD characterization of SiNCs

X-ray Diffractogram were recorded using a Bruker-Nonius D8 Advance diffractometer. Passivated SiNCs samples were prepared by depositing 5 mg of dried sample on a quartz substrate. XRD spectra of freshly etched Si nanocrystals were registered by rapidly depositing the nanocrystals collected by centrifuagation from the etching solution to minimize the oxidation of the nanocrystals prior to the measurement.

C.5 Electrical characterization of solar cells

The current-potential curves for the photovoltaic cells reported in Chapter 2 were registered by irradiating the cell with an ABET2000 solar simulator at AM 1.5G (100 mW cm^{-2}) coupled to a Keithley® 2400 Source Meter. The current density (J) is obtained by dividing the current produced by the measured active area of the cell. The short circuit current J_{sc} is defined as the current density at V=0, while the open circuit voltage V_{oc} is corresponding to the maximum potential reached by the cell (at J=0). The PCE is calculated by applying the following relation:

$$\eta = \frac{P_{max}}{P_{in}} \tag{C.1}$$

Where η is the Photon to Current Efficiency (PCE), P_{max} is the maximum power generated by the cell, defined as the highest value reached for the product $P_{max} = J$ x V, and P_{in} is the incident power related to the light source.

C.6 Hydrogen Evolution experiments

The hydrogen evolution experiments described in Chapter 4 were carried out upon continuous visible light irradiation with a 175 W xenon CERMAX arc-lamp (cut-off filter at 400 nm) of a reactor (a 10 mm path length pyrex glass cuvette with head space obtained from a round-bottom flask) containing the solution. The measuring cell is sealed during the photoreaction: the head to which cell is attached has indeed four ports, closed with Swagelok connections, two of them are part of a closed loop involving GC gas inlet and sample vent in order to analyze head space content without an appreciable gas consumption, and the other two are for

the degassing procedure (input and output).

The gas phase of the reaction vessel was analyzed on an Agilent Technologies 490 microGC equipped with a 5 molecular sieve column (10 m), a thermal conductivity detector, and using Ar as carrier gas. 5 mL from the headspace of the reactor are sampled by the internal GC pump and 200 nL are injected in the column maintained at 60°C for separation and detection of gases. The unused gas sample is then reintroduced in the reactor in order to minimize its consumption along the whole photolysis. The amount of hydrogen was quantified through the external calibration method.

This procedure was performed, prior to analysis, through a galvanostatic (typically 1 mA) electrolysis of a 0.1 M H_2SO_4 solution in an analogous cell (same volume) equipped with two Pt wires sealed in the glass at the bottom of the cell. A 100% faradaic efficiency was assumed leading to a linear correlation between the amount of H_2 evolved at the cathode and the electrolysis time. Hydrogen Evolution Experiments. In a typical experiment, samples of 5 mL were prepared in 20 mL scintillation vials by mixing the RuPAMAM/PtNps solution with ascorbic acid. The pH was then regulated at the desired value upon addition of few droplets of a 5 M NaOH solution. The solution was then put in the reactor, degassed by bubbling Ar for 30 min, and thermostated at 15°C. The cell was then irradiated under continuous vigorous stirring of the solution. The gas phase of the reaction was analyzed through GC and the amount of hydrogen quantified.

Bibliography

[1] REN21 - Renewable Energy Policy Network for the 21st Century, Renewables 2014 Global Status Report. 2014; http://www.ren21.net/resources/publications/.

[2] Ellabban, O.; Abu-Rub, H.; Blaabjerg, F. Renewable energy resources: Current status, future prospects and their enabling technology. *Renewable and Sustainable Energy Reviews* 2014, *39*, 748–764.

[3] Califano, M.; Zunger, A.; Franceschetti, A. Radiative decay of " bright " and " dark " excitons in CdSe nanocrystal quantum dots : the role of surface hole traps. *Nano Letters* 2005, *5*, 2360.

[4] Alivisatos, A. P. Semiconductor Clusters, Nanocrystals, and Quantum Dots. *Science* 1996, *271*, 933–937.

[5] Geim, A. K.; Novoselov, K. S. The rise of graphene. *Nature Materials* 2007, *6*, 183–191.

[6] Wang, Q. H.; Kalantar-Zadeh, K.; Kis, A.; Coleman, J. N.; Strano, M. S. Electronics and optoelectronics of two-dimensional transition metal dichalcogenides. *Nature nanotechnology* 2012, *7*, 699–712.

[7] Burda, C.; Chen, X.; Narayanan, R.; El-Sayed, M. A. Chemistry and Properties of Nanocrystals of Different Shapes. *Chemical Reviews* 2005, *105*, 1025–1102.

[8] Brus, L. E. A simple model for the ionization potential, electron affinity, and aqueous redox potentials of small semiconductor crystallites. *The Journal of Chemical Physics* 1983, *79*, 5566.

[9] Kamat, P. V. Boosting the efficiency of quantum dot sensitized solar cells through modulation of interfacial charge transfer. *Accounts of Chemical Research* 2012, *45*, 1906–1915.

[10] Kamat, P. V. Quantum Dot Solar Cells. Semiconductor Nanocrystals as Light Harvesters. *The Journal of Physical Chemistry C* 2008, *112*, 18737–18753.

[11] Anikeeva, P. O.; Halpert, J. E.; Bawendi, M. G.; Bulović, V. Quantum dot light-emitting devices with electroluminescence tunable over the entire visible spectrum. *Nano Letters* 2009, *9*, 2532–2536.

[12] Shen, H.; Bai, X.; Wang, A.; Wang, H.; Qian, L.; Yang, Y.; Titov, A.; Hyvonen, J.; Zheng, Y.; Li, L. S. High-Efficient Deep-Blue Light-Emitting Diodes by Using High Quality Zn-CdS/ZnS Core/Shell Quantum Dots. *Advanced Functional Materials* 2014, *24*, 2367–2373.

[13] Chan, W. C. W.; Maxwell, D. J.; Gao, X.; Bailey, R. E.; Han, M.; Nie, S. Luminescent quantum dots for multiplexed biological detection and imaging. *Current Opinion in Biotechnology* 2002, *13*, 40–46.

[14] Zhou, J.; Yang, Y.; Zhang, C.-y. Toward Biocompatible Semiconductor Quantum Dots: From Biosynthesis and Bioconjugation to Biomedical Application. *Chemical Reviews* 2015, *115*, 11669–11717.

[15] Liu, Y.; Gibbs, M.; Puthussery, J.; Gaik, S.; Ihly, R.; Hillhouse, H. W.; Law, M. Dependence of carrier mobility on nanocrystal size and ligand length in pbse nanocrystal solids. *Nano Letters* 2010, *10*, 1960–1969.

[16] Derfus, A. M.; Chan, W. C. W.; Bhatia, S. N. Probing the Cytotoxicity of Semiconductor Quantum Dots. *Nano Letters* 2004, *4*, 11–18.

[17] Cullis, A. G.; Canham, L. T. Visible light emission due to quantum size effects in highly porous crystalline silicon. *Nature* 1991, *353*, 335–338.

[18] Buriak, J. M. Organometallic chemistry on silicon and germanium surfaces. *Chemical Reviews* 2002, *102*, 1271–308.

[19] McVey, B. F. P.; Tilley, R. D. Solution synthesis, optical properties, and bioimaging applications of silicon nanocrystals. *Accounts of chemical research* 2014, *47*, 3045–51.

[20] Hessel, C. M.; Reid, D.; Panthani, M. G.; Rasch, M. R.; Goodfellow, B. W.; Wei, J.; Fujii, H.; Akhavan, V.; Korgel, B. a. Synthesis of Ligand-Stabilized Silicon Nanocrystals with Size-Dependent Photoluminescence Spanning Visible to Near-Infrared Wavelengths. *Chemistry of Materials* 2012, *24*, 393–401.

[21] Pavesi, L.; Turan, R. *Silicon Nanocrystals*; Wiley-VCH Verlag GmbH & Co. KGaA, 2010.

[22] Mastronardi, M. L.; Maier-Flaig, F.; Faulkner, D.; Henderson, E. J.; Kubel, C.; Lemmer, U.; Ozin, G. A. Size-dependent absolute quantum yields for size-separated colloidally-stable silicon nanocrystals. *Nano Letters* 2012, *12*, 337–342.

[23] Sangghaleh, F.; Sychugov, I.; Yang, Z.; Veinot, J. G. C.; Linnros, J. Near-Unity Internal Quantum Efficiency of Luminescent Silicon Nanocrystals with Ligand Passivation. *ACS Nano* 2015, *9*, 7097–7104.

[24] Pevere, F.; Sychugov, I.; Sangghaleh, F.; Fucikova, A.; Linnros, J. Biexciton Emission as a Probe of Auger Recombination in Individual Silicon Nanocrystals. *Journal of Physical Chemistry C* 2015, *119*, 7499–7505.

[25] Sevik, C.; Bulutay, C. Auger recombination and carrier multiplication in embedded silicon and germanium nanocrystals. *Physical Review B - Condensed Matter and Materials Physics* 2008, *77*, 3–6.

[26] Miura, S.; Nakamura, T.; Fujii, M.; Inui, M.; Hayashi, S. Size dependence of photoluminescence quantum efficiency of Si nanocrystals. *Physical Review B* 2006, *73*, 1–5.

[27] Dasog, M.; Yang, Z.; Regli, S.; Atkins, T. M.; Faramus, A.; Singh, M. P.; Muthuswamy, E.; Kauzlarich, S. M.; Tilley, R. D.; Veinot, J. G. C. Chemical insight into the origin of red and blue photoluminescence arising from freestanding silicon nanocrystals. *ACS Nano* 2013, *7*, 2676–2685.

[28] Shiohara, A.; Hanada, S.; Prabakar, S.; Fujioka, K.; Lim, T. H.; Yamamoto, K.; Northcote, P. T.; Tilley, R. D. Chemical Reactions on Surface Molecules Attached to Silicon Quantum Dots. *Journal of the American Chemical Society* 2010, *132*, 248–253.

[29] Dohnalová, K.; Gregorkiewicz, T.; Kůsová, K. Silicon quantum dots: surface matters. *Journal of Physics: Condensed Matter* 2014, *26*, 173201.

[30] Mangolini, L.; Kortshagen, U. Plasma-assisted synthesis of silicon nanocrystal inks. *Advanced Materials* 2007, *19*, 2513–2519.

[31] Lau, H. W.; Tan, O. K.; Ooi, B. C.; Liu, Y.; Chen, T. P.; Lu, D. Characteristics of mechanically milled silicon nanocrystals embedded in {TEOS} thin films. *Journal of Crystal Growth* 2006, *288*, 92–95.

[32] Kang, Z.; Tsang, C. H. a.; Zhang, Z.; Zhang, M.; Wong, N.-b.; Zapien, J. A.; Shan, Y.; Lee, S.-T. A polyoxometalate-assisted electrochemical method for silicon nanostructures preparation: from quantum dots to nanowires. *Journal of the American Chemical Society* 2007, *129*, 5326–7.

[33] Lacour, F.; Guillois, O.; Portier, X.; Perez, H.; Herlin, N.; Reynaud, C. Laser pyrolysis synthesis and characterization of luminescent silicon nanocrystals. *Physica E: Low-dimensional Systems and Nanostructures* 2007, *38*, 11–15.

[34] Warner, J. H.; Hoshino, A.; Yamamoto, K.; Tilley, R. D. Water-soluble photoluminescent silicon quantum dots. *Angewandte Chemie* 2005, *44*, 4550–4.

[35] Holmes, J. D.; Ziegler, K. J.; Doty, R. C.; Pell, L. E.; Johnston, K. P.; Korgel, B. A. Highly Luminescent Silicon Nanocrystals with Discrete Optical Transitions. *Journal of the American Chemical Society* 2001, *123*, 3743–3748.

[36] Veprek, S. *Organosilicon Chemistry II*; Wiley-VCH Verlag GmbH, 2008; pp 821–835.

[37] Choi, J.; Wang, N. S.; Reipa, V. Electrochemical reduction synthesis of photoluminescent silicon nanocrystals. *Langmuir* 2009, *25*, 7097–102.

[38] Hessel, C. M.; Henderson, E. J.; Veinot, J. G. C. Hydrogen silsesquioxane: A molecular precursor for nanocrystalline Si-SiO2 composites and freestanding hydride-surface-terminated silicon nanoparticles. *Chemistry of Materials* 2006, *18*, 6139–6146.

[39] Kelly, J. A.; Henderson, E. J.; Veinot, J. G. C. Sol–gel precursors for group 14 nanocrystals. *Chemical Communications* 2010, *46*, 8704.

[40] Kovalev, D.; Fujii, M. Silicon nanocrystals: Photosensitizers for oxygen molecules. *Advanced Materials* 2005, *17*, 2531–2544.

[41] Takeoka, S.; Fujii, M.; Hayashi, S. Size-dependent photoluminescence from surface-oxidized Si nanocrystals in a weak confinement regime. *Physical Review B - Condensed Matter and Materials Physics* 2000, *62*, 16820–16825.

[42] Hapala, P.; Kůsová, K.; Pelant, I.; Jelínek, P. Theoretical analysis of electronic band structure of 2- to 3-nm Si nanocrystals. *Physical Review B* 2013, *87*, 195420.

[43] Weeks, S. L.; MacCo, B.; Van De Sanden, M. C. M.; Agarwal, S. Gas-phase hydrosilylation of plasma-synthesized silicon nanocrystals with short- and long-chain alkynes. *Langmuir* 2012, *28*, 17295–17301.

[44] Yang, Z.; Iqbal, M.; Dobbie, A. R.; Veinot, J. G. C. Surface-induced alkene oligomerization: Does thermal hydrosilylation really lead to monolayer protected silicon nanocrystals? *Journal of the American Chemical Society* 2013, *135*, 17595–17601.

[45] Kelly, J. a.; Veinot, J. G. C. An investigation into near-UV hydrosilylation of freestanding silicon nanocrystals. *ACS Nano* 2010, *4*, 4645–4656.

[46] Wang, X.; Ruther, R. E.; Streifer, J. a.; Hamers, R. J. UV-Induced grafting of alkenes to silicon surfaces: Photoemission versus excitons. *Journal of the American Chemical Society* 2010, *132*, 4048–4049.

[47] Purkait, T. K.; Iqbal, M.; Wahl, M. H.; Gottschling, K.; Gonzalez, C. M.; Islam, M. A.; Veinot, J. G. C. Borane-Catalyzed Room-Temperature Hydrosilylation of Alkenes/Alkynes on Silicon Nanocrystal Surfaces. *Journal of the American Chemical Society* 2014, *136*, 17914–17917.

[48] Biesta, W.; van Lagen, B.; Gevaert, V. S.; Marcelis, A. T. M.; Paulusse, J. M. J.; Nielen, M. W. F.; Zuilhof, H. Preparation, Characterization, and Surface Modification of Trifluoroethyl Ester-Terminated Silicon Nanoparticles. *Chemistry of Materials* 2012, *24*, 4311–4318.

[49] Höhlein, I. M. D.; Kehrle, J.; Helbich, T.; Yang, Z.; Veinot, J. G. C.; Rieger, B. Diazonium Salts as Grafting Agents and Efficient Radical-Hydrosilylation Initiators for Freestanding Photoluminescent Silicon Nanocrystals. *Chemistry - A European Journal* 2014, *20*, 4212–4216.

[50] Höhlein, I. M. D.; Kehrle, J.; Purkait, T. K.; Veinot, J. G. C.; Rieger, B. Photoluminescent silicon nanocrystals with chlorosilane surfaces - synthesis and reactivity. *Nanoscale* 2014, *7*, 914–8.

[51] Höhlein, I. M. D.; Angı, A.; Sinelnikov, R.; Veinot, J. G. C.; Rieger, B. Functionalization of Hydride-Terminated Photoluminescent Silicon Nanocrystals with Organolithium Reagents. *Chemistry - A European Journal* 2015, *21*, 2755–2758.

[52] Dasog, M.; Bader, K.; Veinot, J. G. C. Influence of Halides on the Optical Properties of Silicon Quantum Dots. *Chemistry of Materials* 2015, *27*, 1153–1156.

[53] Dasog, M.; Veinot, J. G. C. Size independent blue luminescence in nitrogen passivated silicon nanocrystals. *Physica Status Solidi A: Applications and Materials Science* 2012, *209*, 1844–1846.

[54] Bell, J. P.; Cloud, J. E.; Cheng, J.; Ngo, C.; Kodambaka, S.; Sellinger, A.; Ratanathanawongs Williams, S. K.; Yang, Y. N-Bromosuccinimide-based bromination and subsequent functionalization of hydrogen-terminated silicon quantum dots. *RSC Advances* 2014, *4*, 51105–51110.

[55] Clark, R. J.; Dang, M. K. M.; Veinot, J. G. C. Exploration of organic acid chain length on water-soluble silicon quantum dot surfaces. *Langmuir* 2010, *26*, 15657–15664.

[56] Yu, Y.; Hessel, C. M.; Bogart, T. D.; Panthani, M. G.; Rasch, M. R.; Korgel, B. a. Room Temperature Hydrosilylation of Silicon Nanocrystals with Bifunctional Terminal Alkenes. *Langmuir* 2013, *29*, 1533–1540.

[57] Rosso-Vasic, M.; Spruijt, E.; Popović, Z.; Overgaag, K.; van Lagen, B.; Grandidier, B.; Vanmaekelbergh, D.; Domínguez-Gutiérrez, D.; De Cola, L.; Zuilhof, H. Amine-terminated silicon nanoparticles: synthesis, optical properties and their use in bioimaging. *Journal of Materials Chemistry* 2009, *19*, 5926.

[58] Cheng, X.; Lowe, S. B.; Reece, P. J.; Gooding, J. J. Colloidal silicon quantum dots: from preparation to the modification of self-assembled monolayers (SAMs) for bio-applications. *Chemical Society Reviews* 2014, *43*, 2680.

[59] Erogbogbo, F.; Yong, K.-t. T.; Roy, I.; Xu, G. X.; Prasad, P. N.; Swihart, M. T. Biocompatible Luminescent Silicon Quantum Dots for Imaging of Cancer Cells. *ACS nano* 2008, *2*, 873–878.

[60] Xu, Z.; Li, Y.; Zhang, B.; Purkait, T.; Alb, A.; Mitchell, B. S.; Grayson, S. M.; Fink, M. J. Water-soluble PEGylated silicon nanoparticles and their assembly into swellable nanoparticle aggregates. *Journal of Nanoparticle Research* 2015, *17*, 1–16.

[61] Ruizendaal, L.; Pujari, S. P.; Gevaerts, V.; Paulusse, J. M. J.; Zuilhof, H. Biofunctional silicon nanoparticles by means of thiol-ene click chemistry. *Chemistry - An Asian Journal* 2011, *6*, 2776–86.

[62] Yu, D.; Liptak, R. W.; Aggarwal, G.; Cheng, a. J.; Campbell, S. a. Tunneling conduction in dense silicon quantum dot/poly (methyl methacrylate) composites. *Thin Solid Films* 2013, *527*, 261–266.

[63] Liu, C.-Y.; Holman, Z.; Kortshagen, U. Hybrid Solar Cells from P3HT and Silicon Nanocrystals. *Nano Lett.* 2009, *9*, 449–452.

[64] Dung, M. X.; Tung, D. D.; Jeong, S.; Jeong, H.-D. Tuning Optical Properties of Si Quantum Dots by π-Conjugated Capping Molecules. *Chemistry - An Asian Journal* 2013, *8*, 653–664.

[65] Zhou, T.; Anderson, R. T.; Li, H.; Bell, J.; Yang, Y.; Gorman, B. P.; Pylypenko, S.; Lusk, M. T.; Sellinger, A. Bandgap tuning of silicon quantum dots by surface functionalization with conjugated organic groups. *Nano Letters* 2015, *15*, 3657–3663.

[66] Chatgilialoglu, C. Structural and Chemical Properties of Silyl Radicals. *Chemical Reviews* 1995, *95*, 1229–1251.

[67] Cicero, R. L.; Linford, M. R.; Chidsey, C. E. D. Photoreactivity of Unsaturated Compounds with Hydrogen-Terminated Silicon(III). *Langmuir* 2000, *16*, 5688–5695.

[68] Buriak, J. M. Illuminating silicon surface hydrosilylation: An unexpected plurality of mechanisms. *Chemistry of Materials* 2014, *26*, 763–772.

[69] Stewart, M. P.; Buriak, J. M. Exciton-mediated hydrosilylation on photoluminescent nanocrystalline silicon. *Journal of the American Chemical Society* 2001, *123*, 7821–7830.

[70] Khung, Y. L.; Ngalim, S. H.; Scaccabarozi, A.; Narducci, D. Thermal and UV Hydrosilylation of Alcohol-Based Bifunctional Alkynes on Si (III) surfaces: How surface radicals influence surface bond formation. *Scientific Reports* 2015, *5*, 11299.

[71] Downs, R. T.; Hall-Wallace, M. The American Mineralogist crystal structure database. *American Mineralogist* 2003, *88*, 247–250.

[72] Yang, Z.; De los Reyes, G. B.; Titova, L. V.; Sychugov, I.; Dasog, M.; Linnros, J.; Hegmann, F. a.; Veinot, J. G. C. Evolution of the Ultrafast Photoluminescence of Colloidal Silicon Nanocrystals with Changing Surface Chemistry. *ACS Photonics* 2015, *2*, 595–605.

[73] Balzani, V.; Ceroni, P.; Juris, A. *Photochemistry and Photophysics: Concepts, Research, Applications*; Wiley-VCH Verlag GmbH & Co. KGaA, 2014; p 504.

[74] Armaroli, N.; Balzani, V. *Energy for a Sustainable World*; Wiley-VCH Verlag GmbH & Co. KGaA: Weinheim, Germany, 2010.

[75] Shockley, W.; Queisser, H. J. Detailed Balance Limit of Efficiency of p-n Junction Solar Cells. *Journal of Applied Physics* 1961, *32*, 510.

[76] Dalven, R. *Introduction to Applied Solid State Physics Topics in the Applications of Semiconductors, Superconductors, Ferromagnetism, and the Nonlinear Optical Properties of Solids*; Springer, 1990.

[77] Schlierf, A.; Yang, H.; Gebremedhn, E.; Treossi, E.; Ortolani, L.; Chen, L.; Minoia, A.; Morandi, V.; Samorì, P.; Casiraghi, C.; Beljonne, D.; Palermo, V. Nanoscale insight into the exfoliation mechanism of graphene with organic dyes: effect of charge, dipole and molecular structure. *Nanoscale* 2013, *5*, 4205–16.

[78] An, X.; Simmons, T.; Shah, R.; Wolfe, C.; Lewis, K. M.; Washington, M.; Nayak, S. K.; Talapatra, S.; Kar, S. Stable aqueous dispersions of noncovalently functionalized graphene from graphite and their multifunctional high-performance applications. *Nano Letters* 2010, *10*, 4295–301.

[79] Hwang, Y. L.; Hwang, K. C. Nonlinear Stern-Volmer Fluorescence Quenching of Pyrene by C 60/70. *Fullerene Science and Technology* 1999, *7*, 437–454.

[80] Nojiri, T.; Watanabe, A.; Ito, O. Photoinduced Electron Transfer between C 60 /C 70 and Zinc Tetraphenylporphyrin in Polar Solvents. *The Journal of Physical Chemistry A* 1998, *102*, 5215–5219.

[81] Sension, R. J.; Phillips, C. M.; Szarka, A. Z.; Romanow, W. J.; McGhie, A. R.; McCauley, J. P.; Smith, A. B.; Hochstrasser, R. M. Transient absorption studies of carbon (C60) in solution. *The Journal of Physical Chemistry* 1991, *95*, 6075–6078.

[82] Guldi, D. M.; Prato, M. Excited-State Properties of C60 Fullerene Derivatives. *Accounts of Chemical Research* 2000, *33*, 695–703.

[83] Rio, Y.; Accorsi, G.; Nierengarten, H.; Bourgogne, C.; Strub, J.-M.; Dorsselaer, A. V.; Armaroli, N.; Nierengarten, J.-F. A fullerene core to probe dendritic shielding effects. *Tetrahedron* 2003, *59*, 3833–3844.

[84] Chen, R. J.; Zhang, Y.; Wang, D.; Dai, H. Noncovalent Sidewall Functionalization of Single-Walled Carbon Nanotubes for Protein Immobilization. *Journal of the American Chemical Society* 2001, *123*, 3838–3839.

[85] Ortolani, L.; Cadelano, E.; Veronese, G. P.; Degli Esposti Boschi, C.; Snoeck, E.; Colombo, L.; Morandi, V. Folded graphene membranes: Mapping curvature at the nanoscale. *Nano Letters* 2012, *12*, 5207–5212.

[86] Panthani, M. M. G.; Hessel, C. M. C.; Reid, D.; Casillas, G.; José-Yacamán, M.; Korgel, B. A. Graphene-Supported High-Resolution TEM and STEM Imaging of Silicon Nanocrystals and their Capping Ligands. *The Journal of Physical Chemistry C* 2012, *116*, 22463–22468.

[87] Grancini, G.; Biasiucci, M.; Mastria, R.; Scotognella, F.; Tassone, F.; Polli, D.; Gigli, G.; Lanzani, G. Dynamic Microscopy Study of Ultrafast Charge Transfer in a Hybrid P3HT/Hyperbranched CdSe Nanoparticle Blend for Photovoltaics. *The Journal of Physical Chemistry Letters* 2012, *3*, 517–523.

[88] Gupta, S.; Varandani, D.; Sharma, A.; Satsangi, V.; Mehta, B. Nanoscale interface mapping of a CdS−CZTS single nanorod heterojunction using Kelvin probe force microscopy. *Applied Surface Science* 2015, *331*, 327–332.

[89] Böhmisch, M.; Burmeister, F.; Rettenberger, A.; Zimmermann, J.; Boneberg, J.; Leiderer, P. Atomic Force Microscope Based Kelvin Probe Measurements: Application to an Electrochemical Reaction. *The Journal of Physical Chemistry B* 1997, *101*, 10162–10165.

[90] O'Regan, B.; Gratzel, M. A low-cost, high-efficiency solar cell based on dye-sensitized colloidal TiO2 films. *Nature* 1991, *353*, 737–740.

[91] Bella, F.; Griffini, G.; Gerosa, M.; Turri, S.; Bongiovanni, R. Performance and stability improvements for dye-sensitized solar cells in the presence of luminescent coatings. *Journal of Power Sources* 2015, *283*, 195–203.

[92] Liu, J.; Yao, Q.; Li, Y. Effects of downconversion luminescent film in dye-sensitized solar cells. *Applied Physics Letters* 2006, *88*, 173119.

[93] Hosseini, Z.; Huang, W.-K.; Tsai, C.-M.; Chen, T.-M.; Taghavinia, N.; Diau, E. W.-G. Enhanced Light Harvesting with a Reflective Luminescent Down-Shifting Layer for Dye-Sensitized Solar Cells. *ACS Applied Materials & Interfaces* 2013, *5*, 5397–5402.

[94] Rothemund, R.; Kreuzer, S.; Umundum, T.; Meinhardt, G.; Fromherz, T.; Jantsch, W. External quantum efficiency analysis of Si solar cells with II-VI nanocrystal luminescent down-shifting layers. *Energy Procedia* 2011, *10*, 83–87.

[95] Kalytchuk, S.; Gupta, S.; Zhovtiuk, O.; Vaneski, A.; Kershaw, S. V.; Fu, H.; Fan, Z.; Kwok, E. C. H.; Wang, C.-f.; Teoh, W. Y.; Rogach, A. L. Semiconductor Nanocrystals as Luminescent Down-Shifting Layers To Enhance the Efficiency of Thin-Film CdTe/CdS and Crystalline Si Solar Cells. *The Journal of Physical Chemistry C* 2014, *118*, 16393–16400.

[96] Dembele, K. T.; Selopal, G. S.; Milan, R.; Trudeau, C.; Benetti, D.; Soudi, A.; Natile, M. M.; Sberveglieri, G.; Cloutier, S.; Concina, I.; Rosei, F.; Vomiero, A. Graphene below the percolation threshold in TiO2 for dye-sensitized solar cells. *Journal of Materials Chemistry A* 2015, *3*, 2580–2588.

[97] Choi, S. C.; Lee, H. S.; Sohn, S. H. Effects of light scattering TiO2 surface-modified by dual oxide coating in dye-sensitized solar cells. *Advanced Powder Technology* 2012, *23*, 866–871.

[98] Ryu, J.; Yun, J.; Lee, J.; Lee, K.; Jang, J. Hierarchical mesoporous silica nanoparticles as superb light scattering materials. *Chemical Communications* 2016, *52*, 2165–2168.

[99] Batchelder, J. S.; Zewail, a. H.; Cole, T. Luminescent solar concentrators. 1: Theory of operation and techniques for performance evaluation. *Applied Optics* 1979, *18*, 3090–3110.

[100] Debije, M. G.; Verbunt, P. P. C. Thirty years of luminescent solar concentrator research: Solar energy for the built environment. *Advanced Energy Materials* 2012, *2*, 12–35.

[101] Debije, M. Renewable energy: Better luminescent solar panels in prospect. *Nature* 2015, *519*, 298.

[102] Bradshaw, L. R.; Knowles, K. E.; McDowall, S.; Gamelin, D. R. Nanocrystals for Luminescent Solar Concentrators. *Nano Letters* 2015, *15*, 1315–1323.

[103] Meinardi, F.; Colombo, A.; Velizhanin, K. A.; Simonutti, R.; Lorenzon, M.; Beverina, L.; Viswanatha, R.; Klimov, V. I.; Brovelli, S. Large-area luminescent solar concentrators based on 'Stokes-shift-engineered' nanocrystals in a mass-polymerized PMMA matrix. *Nature Photonics* 2014, *8*, 392–399.

[104] Shcherbatyuk, G. V.; Inman, R. H.; Wang, C.; Winston, R.; Ghosh, S. Viability of using near infrared PbS quantum dots as active materials in luminescent solar concentrators. *Applied Physics Letters* 2010, *96*, 191901.

[105] Meinardi, F.; McDaniel, H.; Carulli, F.; Colombo, A.; Velizhanin, K. A.; Makarov, N. S.; Simonutti, R.; Klimov, V. I.; Brovelli, S. Highly efficient large-area colourless luminescent solar concentrators using heavy-metal-free colloidal quantum dots. *Nature Nanotechnology* 2015, *10*, 878–885.

[106] Coropceanu, I.; Bawendi, M. G. Core/Shell Quantum Dot Based Luminescent Solar Concentrators with Reduced Reabsorption and Enhanced Efficiency. *Nano Letters* 2014, *14*, 4097–4101.

[107] Carrette, L.; Friedrich, K.; Stimming, U. Fuel cells: principles, types, fuels, and applications. *Chemphyschem : a European journal of chemical physics and physical chemistry* 2000, *1*, 162–93.

[108] Bard, A. J.; Faulkner, L. R. *Electrochemical Methods: Fundamentals and Applications*; Wiley, 2000.

[109] Satyapal, S.; Petrovic, J.; Read, C.; Thomas, G.; Ordaz, G. The U.S. Department of Energy's National Hydrogen Storage Project: Progress towards meeting hydrogen-powered vehicle requirements. *Catalysis Today* 2007, *120*, 246–256.

[110] Conway, B. E.; Tilak, B. V. Interfacial processes involving electrocatalytic evolution and oxidation of H2, and the role of chemisorbed H. *Electrochimica Acta* 2002, *47*, 3571–3594.

[111] Mukerjee, S. Particle size and structural effects in platinum electrocatalysis. *Journal of Applied Electrochemistry* 1990, *20*, 537–548.

[112] Tan, T. L.; Wang, L.-L.; Zhang, J.; Johnson, D. D.; Bai, K. Platinum Nanoparticle During Electrochemical Hydrogen Evolution: Adsorbate Distribution, Active Reaction Species, and Size Effect. *ACS Catalysis* 2015, *5*, 2376–2383.

[113] Antolini, E. Carbon supports for low-temperature fuel cell catalysts. *Applied Catalysis B: Environmental* 2009, *88*, 1–24.

[114] Lu, J.; Do, I.; Drzal, L. T.; Worden, R. M.; Lee, I. Nanometal-decorated exfoliated graphite nanoplatelet based glucose biosensors with high sensitivity and fast response. *ACS Nano* 2008, *2*, 1825–32.

[115] Li, H.; Cooper-White, J. J. Hyperbranched polymer mediated fabrication of water soluble carbon nanotube-metal nanoparticle hybrids. *Nanoscale* 2013, *5*, 2915–20.

[116] Yang, L.; Wang, G.; Liu, Y. An acetylcholinesterase biosensor based on platinum nanoparticles-carboxylic graphene-nafion modified electrode for detection of pesticides. *Analytical Biochemistry* 2013, *437*, 144–149.

[117] Kim, Y.-G.; Akbar, Z. A.; Kim, D. Y.; Jo, S. M.; Jang, S.-Y. Aqueous Dispersible Graphene/Pt Nanohybrids by Green Chemistry: Application as Cathodes for Dye-Sensitized Solar Cells. *ACS Applied Materials & Interfaces* 2013, *5*, 2053–2061.

[118] Qian, W.; Hao, R.; Zhou, J.; Eastman, M.; Manhat, B. a.; Sun, Q.; Goforth, A. M.; Jiao, J. Exfoliated graphene-supported Pt and Pt-based alloys as electrocatalysts for direct methanol fuel cells. *Carbon* 2013, *52*, 595–604.

[119] Tung, V. C.; Chen, L.-M.; Allen, M. J.; Wassei, J. K.; Nelson, K.; Kaner, R. B.; Yang, Y. Low-Temperature Solution Processing of Graphene−Carbon Nanotube Hybrid Materials for High-Performance Transparent Conductors. *Nano Letters* 2009, *9*, 1949–1955.

[120] Gengler, R. Y. N.; Spyrou, K.; Rudolf, P. A roadmap to high quality chemically prepared graphene. *Journal of Physics D: Applied Physics* 2010, *43*, 374015.

[121] Quintana, M.; López, A. M.; Rapino, S.; Toma, F. M.; Iurlo, M.; Carraro, M.; Sartorel, A.; MacCato, C.; Ke, X.; Bittencourt, C.; Da Ros, T.; Van Tendeloo, G.; Marcaccio, M.; Paolucci, F.; Prato, M.; Bonchio, M. Knitting the catalytic pattern of artificial photosynthesis to a hybrid graphene nanotexture. *ACS Nano* 2013, *7*, 811–817.

[122] Yan, Y.; Xia, B.; Qi, X.; Wang, H.; Xu, R.; Wang, J.-Y.; Zhang, H.; Wang, X. Nanotungsten carbide decorated graphene as co-catalysts for enhanced hydrogen evolution on molybdenum disulfide. *Chemical Communications* 2013, *49*, 4884.

[123] Seger, B.; Kamat, P. V. Electrocatalytically Active Graphene-Platinum Nanocomposites. Role of 2-D Carbon Support in PEM Fuel Cells. *The Journal of Physical Chemistry C* 2009, *113*, 7990–7995.

[124] Li, Y.; Gao, W.; Ci, L.; Wang, C.; Ajayan, P. M. Catalytic performance of Pt nanoparticles on reduced graphene oxide for methanol electro-oxidation. *Carbon* 2010, *48*, 1124–1130.

[125] Pénicaud, A.; Drummond, C. Deconstructing graphite: Graphenide solutions. *Accounts of Chemical Research* 2013, *46*, 129–137.

[126] Ciesielski, A.; Samorì, P. Graphene via sonication assisted liquid-phase exfoliation. *Chemical Society Reviews* 2014, *43*, 381–98.

[127] Georgakilas, V.; Otyepka, M.; Bourlinos, A. B.; Chandra, V.; Kim, N.; Kemp, K. C.; Hobza, P.; Zboril, R.; Kim, K. S. Functionalization of Graphene: Covalent and Non-Covalent Approaches, Derivatives and Applications. *Chemical Reviews* 2012, *112*, 6156–6214.

[128] Brodie, B. C. On the Atomic Weight of Graphite. *Philosophical Transactions of the Royal Society of London* 1859, *149*, 249–259.

[129] Hernandez, Y.; Nicolosi, V.; Lotya, M.; Blighe, F. M.; Sun, Z.; De, S.; McGovern, I. T.; Holland, B.; Byrne, M.; Gun'Ko, Y. K.; Boland, J. J.; Niraj, P.; Duesberg, G.; Krishnamurthy, S.; Goodhue, R.; Hutchison, J.; Scardaci, V.; Ferrari, A. C.; Coleman, J. N. High-yield production of graphene by liquid-phase exfoliation of graphite. *Nature Nanotechnology* 2008, *3*, 563–568.

[130] Hernandez, Y.; Lotya, M.; Rickard, D.; Bergin, S. D.; Jonathan, N.; Nano, J. N. A. C. S.; Coleman, J. N. Measurement of Multicomponent Solubility Parameters for Graphene Facilitates Solvent Discovery. *Langmuir* 2010, *26*, 3208–3213.

[131] Khan, U.; Porwal, H.; O'Neill, A.; Nawaz, K.; May, P.; Coleman, J. N. Solvent-Exfoliated Graphene at Extremely High Concentration. *Langmuir* 2011, *27*, 9077–9082.

[132] Rabe, J. P.; Buchholz, S. Commensurability and Mobility in Two-Dimensional Molecular Patterns on Graphite. *Science* 1991, *253*, 424–427.

[133] Ciesielski, A.; Haar, S.; El Gemayel, M.; Yang, H.; Clough, J.; Melinte, G.; Gobbi, M.; Orgiu, E.; Nardi, M. V.; Ligorio, G.; Palermo, V.; Koch, N.; Ersen, O.; Casiraghi, C.; Samorì, P. Harnessing the Liquid-Phase Exfoliation of Graphene Using Aliphatic Compounds: A Supramolecular Approach. *Angewandte Chemie International Edition* 2014, *53*, 10355–10361.

[134] Haar, S.; Ciesielski, A.; Clough, J.; Yang, H.; Mazzaro, R.; Richard, F.; Conti, S.; Merstorf, N.; Cecchini, M.; Morandi, V.; Casiraghi, C.; Samorì, P. A Supramolecular Strategy to Leverage the Liquid-Phase Exfoliation of Graphene in the Presence of Surfactants: Unraveling the Role of the Length of Fatty Acids. *Small* 2015, *11*, 1691–1702.

[135] Döbbelin, M.; Ciesielski, A.; Haar, S.; Osella, S.; Bruna, M.; Minoia, A.; Grisanti, L.; Mosciatti, T.; Richards, F.; Adi, E. P.; Cola, L. D.; Palermo, V.; Mazzaro, R.; Morandi, V.; Lazzaroni, R.; Ferrari, A. C.; Beljonne, D.; Samorì, P. Light-enhanced liquid-phase exfoliation and photoswitching current in graphene-azobenzene composites. *Nature communications* 2016, in press.

[136] Qu, L.; Martin, R. B.; Huang, W.; Fu, K.; Zweifel, D.; Lin, Y.; Sun, Y.-P.; Bunker, C. E.; Harruff, B. A.; Gord, J. R.; Allard, L. F. Interactions of functionalized carbon nanotubes with tethered pyrenes in solution. *The Journal of Chemical Physics* 2002, *117*.

[137] Lee, D.-W.; Kim, T.; Lee, M. An amphiphilic pyrene sheet for selective functionalization of graphene. *Chemical Communications* 2011, *47*, 8259–61.

[138] Ghosh, S.; An, X.; Shah, R.; Rawat, D.; Dave, B.; Kar, S.; Talapatra, S. Effect of 1-Pyrene Carboxylic-Acid Functionalization of Graphene on Its Capacitive Energy Storage. *The Journal of Physical Chemistry C* 2012, *116*, 20688–20693.

[139] Zhang, M.; Parajuli, R. R.; Mastrogiovanni, D.; Dai, B.; Lo, P.; Cheung, W.; Brukh, R.; Chiu, P. L.; Zhou, T.; Liu, Z.; Garfunkel, E.; He, H. Production of Graphene Sheets by Direct Dispersion with Aromatic Healing Agents. *Small* 2010, *6*, 1100–1107.

[140] Parviz, D.; Das, S.; Ahmed, H. S. T.; Irin, F.; Bhattacharia, S.; Green, M. J. Dispersions of non-covalently functionalized graphene with minimal stabilizer. *ACS Nano* 2012, *6*, 8857–8867.

[141] Xu, C.; Wang, X.; Zhu, J. Graphene−Metal Particle Nanocomposites. *The Journal of Physical Chemistry C* 2008, *112*, 19841–19845.

[142] Li, Z.; Chen, Y.; Du, Y.; Wang, X.; Yang, P.; Zheng, J. Triphenylamine-functionalized graphene decorated with Pt nanoparticles and its application in photocatalytic hydrogen production. *International Journal of Hydrogen Energy* 2012, *37*, 4880–4888.

[143] Zhuo, Q.; Ma, Y.; Gao, J.; Zhang, P.; Xia, Y.; Tian, Y.; Sun, X.; Zhong, J.; Sun, X. Facile synthesis of graphene/metal nanoparticle composites via self-catalysis reduction at room temperature. *Inorganic Chemistry* 2013, *52*, 3141–7.

[144] Khan, U.; O'Neill, A.; Lotya, M.; De, S.; Coleman, J. N. High-Concentration Solvent Exfoliation of Graphene. *Small* 2010, *6*, 864–871.

[145] Yi, M.; Shen, Z.; Liang, S.; Liu, L.; Zhang, X.; Ma, S. Water can stably disperse liquid-exfoliated graphene. *Chemical communications* 2013, *49*, 11059–61.

[146] Chen, A.; Holt-Hindle, P. Platinum-based nanostructured materials: synthesis, properties, and applications. *Chemical Reviews* 2010, *110*, 3767–804.

[147] Xia, G.; Huang, C.; Wang, Y. Highly uniform platinum nanoparticles supported on graphite nanoplatelets as a catalyst for proton exchange membrane fuel cells. *International Journal of Hydrogen Energy* 2013, *38*, 13754–13761.

[148] Zamolo, V. A.; Valenti, G.; Venturelli, E.; Chaloin, O.; Marcaccio, M.; Boscolo, S.; Castagnola, V.; Sosa, S.; Berti, F.; Fontanive, G.; Poli, M.; Tubaro, A.; Bianco, A.; Paolucci, F.; Prato, M. Highly Sensitive Electrochemiluminescent Nanobiosensor for the Detection of Palytoxin. *ACS Nano* 2012, *6*, 7989–7997.

[149] Costentin, C.; Drouet, S.; Robert, M.; Savéant, J. M. Turnover numbers, turnover frequencies, and overpotential in molecular catalysis of electrochemical reactions. Cyclic voltammetry and preparative-scale electrolysis. *Journal of the American Chemical Society* 2012, *134*, 11235–11242.

[150] Tran, P. D.; Wong, L. H.; Barber, J.; Loo, J. S. C. Recent advances in hybrid photocatalysts for solar fuel production. *Energy & Environmental Science* 2012, *5*, 5902.

[151] Fujishima, a.; Honda, K. Electrochemical photolysis of water at a semiconductor electrode. *Nature* 1972, *238*, 37–38.

[152] Maeda, K. Photocatalytic water splitting using semiconductor particles: History and recent developments. *Journal of Photochemistry and Photobiology C: Photochemistry Reviews* 2011, *12*, 237–268.

[153] Balzani, V.; Bergamini, G.; Ceroni, P. Light: A Very Peculiar Reactant and Product. *Angewandte Chemie International Edition* 2015, *54*, 11320–11337.

[154] Creutz, C.; Sutin, N. Electron-transfer reactions of excited states. Reductive quenching of the tris(2,2'-bipyridine)ruthenium(II) luminescence. *Inorganic Chemistry* 1976, *15*, 496–499.

[155] Brown, G. M.; Brunschwig, B. S.; Creutz, C.; Endicott, J. F.; Sutin, N. Homogeneous catalysis of the photoreduction of water by visible light. Mediation by a tris(2,2'-bipyridine)ruthenium(II)-cobalt(II) macrocycle system. *Journal of the American Chemical Society* 1979, *101*, 1298–1300.

[156] Tong, L.; Kopecky, A.; Zong, R.; Gagnon, K. J.; Ahlquist, M. S. G.; Thummel, R. P. Light-Driven Proton Reduction in Aqueous Medium Catalyzed by a Family of Cobalt Complexes with Tetradentate Polypyridine-Type Ligands. *Inorganic Chemistry* 2015, *54*, 7873–7884.

[157] Chen, L.; Chen, G.; Leung, C.-F.; Yiu, S.-M.; Ko, C.-C.; Anxolabéhère-Mallart, E.; Robert, M.; Lau, T.-C. Dual Homogeneous and Heterogeneous Pathways in Photo- and Electrocatalytic Hydrogen Evolution with Nickel(II) Catalysts Bearing Tetradentate Macrocyclic Ligands. *ACS Catalysis* 2015, *5*, 356–364.

[158] Eckenhoff, W. T.; Brennessel, W. W.; Eisenberg, R. Light-Driven Hydrogen Production from Aqueous Protons using Molybdenum Catalysts. *Inorganic Chemistry* 2014, *53*, 9860–9869.

[159] Lehn, J. M.; Sauvage, J. . P. Chemical storage of light energy, catalytic generation of hydrogen from of neutral acqueous solutions. *Nouveau Journal de Chimie* 1977, 449–451.

[160] Tomalia, D.; Baker, J. R.; Dewald, J.; Hall, M.; Kallos, G.; Martin, S.; Roeck, J.; Ryder, J.; Smith, P. Dendritic Macromolecules: Synthesis of Starburst Dendrimers. *Macromolecules* 1986, *19*, 2466–2468.

[161] Buhleier, E.; Wehner, W.; Vogtle, F. "Cascade"- and "Nonskid-Chain-like" Syntheses of Molecular Cavity Topologies. *Synthesis* 1978, *1978*, 155–158.

[162] Hecht, S.; Fréchet, J. M. J. Dendritic Encapsulation of Function: Applying Nature's Site Isolation Principle from Biomimetics to Materials Science. *Angewandte Chemie International Edition* 2001, *40*, 74–91.

[163] Tomalia, D. A. The dendritic state. *Materials Today* 2005, *8*, 34–46.

[164] Balzani, V.; Campagna, S.; Denti, G.; Juris, A.; Serroni, S.; Venturi, M. Designing Dendrimers Based on Transition-Metal Complexes. Light-Harvesting Properties and Predetermined Redox Patterns. *Accounts of Chemical Research* 1998, *31*, 26–34.

[165] Niederhafner, P.; Šebestík, J.; Ježek, J. Glycopeptide dendrimers. Part I. *Journal of Peptide Science* 2008, *14*, 2–43.

[166] Köhn, F.; Hofkens, J.; Gronheid, R.; Cotlet, M.; Müllen, K.; der Auweraer, M.; De Schryver, F. C. Excitation Energy Transfer in Dendritic Host–Guest Donor–Acceptor Systems. *ChemPhysChem* 2002, *3*, 1005–1013.

[167] Cuadrado, I.; Morán, M.; Casado, C. M.; Alonso, B.; Losada, J. Organometallic dendrimers with transition metals. *Coordination Chemistry Reviews* 1999, *193-195*, 395–445.

[168] Astruc, D.; Boisselier, E.; Ornelas, C. Dendrimers Designed for Functions: From Physical, Photophysical, and Supramolecular Properties to Applications in Sensing, Catalysis, Molecular Electronics, Photonics, and Nanomedicine. *Chemical Reviews* 2010, *110*, 1857–1959.

[169] Scholes, G. D.; Fleming, G. R.; Olaya-Castro, A.; van Grondelle, R. Lessons from nature about solar light harvesting. *Nat Chem* 2011, *3*, 763–774.

[170] Zhang, X.; Zeng, Y.; Yu, T.; Chen, J.; Yang, G.; Li, Y. Advances in photofunctional dendrimers for solar energy conversion. *Journal of Physical Chemistry Letters* 2014, *5*, 2340–2350.

[171] Xu, Z.; Moore, J. S. Rapid Construction of Large-size Phenylacetylene Dendrimers up to 12.5 Nanometers in Molecular Diameter. *Angewandte Chemie International Edition in English* 1993, *32*, 1354–1357.

[172] Sakamoto, M.; Kamachi, T.; Okura, I.; Ueno, A.; Mihara, H. Photoinduced hydrogen evolution with peptide dendrimer–multi-Zn(II)–porphyrin, viologen, and hydrogenase. *Biopolymers* 2001, *59*, 103–109.

[173] Yu, T.; Wang, W.; Chen, J.; Zeng, Y.; Li, Y.; Yang, G.; Li, Y. Dendrimer-Encapsulated Pt Nanoparticles: An Artificial Enzyme for Hydrogen Production. *The Journal of Physical Chemistry C* 2012, *116*, 10516–10521.

[174] Yu, T.; Zeng, Y.; Chen, J.; Li, Y.-Y.; Yang, G.; Li, Y. Exceptional Dendrimer-Based Mimics of Diiron Hydrogenase for the Photochemical Production of Hydrogen. *Angewandte Chemie International Edition* 2013, *52*, 5631–5635.

[175] Bronstein, L. M.; Shifrina, Z. B. Dendrimers as Encapsulating, Stabilizing, or Directing Agents for Inorganic Nanoparticles. *Chemical Reviews* 2011, *111*, 5301–5344.

[176] Yamamoto, D.; Watanabe, S.; Miyahara, M. T. Coordination and Reduction Processes in the Synthesis of Dendrimer-Encapsulated Pt Nanoparticles. *Langmuir* 2010, *26*, 2339–2345.

[177] Storrier, G. D.; Takada, K.; Abruña, H. D. Synthesis, Characterization, Electrochemistry, and EQCM Studies of Polyamidoamine Dendrimers Surface-Functionalized with Polypyridyl Metal Complexes. *Langmuir* 1999, *15*, 872–884.

[178] Glazier, S.; Barron, J. A.; Houston, P. L.; Abruña, H. D. Photophysics of PAMAM-Based Dendrimers of Polypyridyl Complexes of Ruthenium. *The Journal of Physical Chemistry B* 2002, *106*, 9993–10003.

[179] Crooks, R. M.; Zhao, M.; Sun, L.; Chechik, V.; Yeung, L. K. Dendrimer-Encapsulated Metal Nanoparticles: Synthesis, Characterization, and Applications to Catalysis. *Accounts of Chemical Research* 2001, *34*, 181–190.

[180] Balzani, V.; Ceroni, P.; Gestermann, S.; Gorka, M.; Kauffmann, C.; Vögtle, F. Fluorescent guests hosted in fluorescent dendrimers. *Tetrahedron* 2002, *58*, 629–637.

[181] Rau, S.; Schäfer, B.; Gleich, D.; Anders, E.; Rudolph, M.; Friedrich, M.; Görls, H.; Henry, W.; Vos, J. G. A Supramolecular Photocatalyst for the Production of Hydrogen and the Selective Hydrogenation of Tolane. *Angewandte Chemie International Edition* 2006, *45*, 6215–6218.

[182] Elvington, M.; Brown, J.; Arachchige, S. M.; Brewer, K. J. Photocatalytic Hydrogen Production from Water Employing A Ru, Rh, Ru Molecular Device for Photoinitiated Electron Collection. *Journal of the American Chemical Society* 2007, *129*, 10644–10645.

[183] Fihri, A.; Artero, V.; Razavet, M.; Baffert, C.; Leibl, W.; Fontecave, M. Cobaloxime-Based Photocatalytic Devices for Hydrogen Production. *Angewandte Chemie International Edition* 2008, *47*, 564–567.

[184] Ozawa, H.; Haga, M.-a.; Sakai, K. A Photo-Hydrogen-Evolving Molecular Device Driving Visible-Light-Induced EDTA-Reduction of Water into Molecular Hydrogen. *Journal of the American Chemical Society* 2006, *128*, 4926–4927.

[185] McNamara, W. R.; Han, Z.; Yin, C.-J. M.; Brennessel, W. W.; Holland, P. L.; Eisenberg, R. Cobalt-dithiolene complexes for the photocatalytic and electrocatalytic reduction of protons in aqueous solutions. *Proceedings of the National Academy of Sciences* 2012, *109*, 15594–15599.

[186] Shan, B.; Baine, T.; Ma, X. A. N.; Zhao, X.; Schmehl, R. H. Mechanistic Details for Cobalt Catalyzed Photochemical Hydrogen Production in Aqueous Solution: Efficiencies of the Photochemical and Non-Photochemical Steps. *Inorganic Chemistry* 2013, *52*, 4853–4859.

[187] Liu, C.; Li, F.; Ma, L.-P.; Cheng, H.-M. Advanced Materials for Energy Storage. *Advanced Materials* 2010, *22*, E28–E62.

[188] Crosby, G. A.; Demas, J. N. Measurement of photoluminescence quantum yields. Review. *The Journal of Physical Chemistry* 1971, *75*, 991–1024.

[189] Moggi, L.; Juris, A.; Gandolfi, T. *Manuale del fotochimico. Tecniche e metodologie*; Quaderni della fotochimica; Bononia University Press, 2006.

[190] Suzuki, K.; Kobayashi, A.; Kaneko, S.; Takehira, K.; Yoshihara, T.; Ishida, H.; Shiina, Y.; Oishi, S.; Tobita, S. Reevaluation of absolute luminescence quantum yields of standard solutions using a spectrometer with an integrating sphere and a back-thinned CCD detector. *Phys. Chem. Chem. Phys.* 2009, *11*, 9850–9860.

[191] Würth, C.; Grabolle, M.; Pauli, J.; Spieles, M.; Resch-genger, U. Relative and absolute determination of fluorescence quantum yields of transparent samples. *Nature protocols* 2013, *8*, 1535–50.

[192] Williams, D. B.; Carter, C. B. *Transmission Electron Microscopy*; Springer.

[193] Zerweck, U.; Loppacher, C.; Otto, T.; Grafström, S.; Eng, L. M. Accuracy and resolution limits of Kelvin probe force microscopy. *Physical Review B - Condensed Matter and Materials Physics* 2005, *71*, 1–9.

,

List of Publications

[1] Lincheneau, C.; Amelia, M.; Oszajca, M.; Boccia, A.; D'Orazi, F.; Madrigale, M.; Zanoni, R.; Mazzaro, R.; Ortolani, L.; Morandi, V.; Silvi, S.; Szaciłowski, K.; Credi, A. Synthesis and properties of ZnTe and ZnTe/ZnS core/shell semiconductor nanocrystals. *Journal of Materials Chemistry C* 2014, *2*, 2877.

[2] Bansal, a. K.; Antolini, F.; Sajjad, M. T.; Stroea, L.; Mazzaro, R.; Ramkumar, S. G.; Kass, K.-J.; Allard, S.; Scherf, U.; Samuel, I. D. W. Photophysical and structural characterisation of in situ formed quantum dots. *Physical Chemistry Chemical Physics* 2014, *16*, 9556.

[3] Ravotto, L.; Mazzaro, R.; Natali, M.; Ortolani, L.; Morandi, V.; Ceroni, P.; Bergamini, G. Photoactive dendrimer for water photoreduction: a scaffold to combine sensitizers and catalysts. *The Journal of Physical Chemistry Letters* 2014, *5*, 798–803.

[4] Haar, S.; Ciesielski, A.; Clough, J.; Yang, H.; Mazzaro, R.; Richard, F.; Conti, S.; Merstorf, N.; Cecchini, M.; Morandi, V.; Casiraghi, C.; Samorì, P. A Supramolecular Strategy to Leverage the Liquid-Phase Exfoliation of Graphene in the Presence of Surfactants: Unraveling the Role of the Length of Fatty Acids. *Small* 2015, *11*, 1691–1702.

[5] Mazzaro, R.; Boni, A.; Valenti, G.; Marcaccio, M.; Paolucci, F.; Ortolani, L.; Morandi, V.; Ceroni, P.; Bergamini, G. Uniform Functionalization of High-Quality Graphene with Platinum Nanoparticles for Electrocatalytic Water Reduction. *ChemistryOpen* 2015, *4*, 268–273.

[6] Mazzaro, R.; Locritani, M.; Molloy, J. K.; Montalti, M.; Yu, Y.; Korgel, B. a.; Bergamini, G.; Morandi, V.; Ceroni, P. Photoinduced Processes between Pyrene-Functionalized Silicon Nanocrystals and Carbon Allotropes. *Chemistry of Materials* 2015, *27*, 4390–4397.

[7] Döbbelin, M.; Ciesielski, A.; Haar, S.; Osella, S.; Bruna, M.; Minoia, A.; Grisanti, L.; Mosciatti, T.; Richards, F.; Adi, E. P.; Cola, L. D.; Palermo, V.; Mazzaro, R.; Morandi, V.; Lazzaroni, R.; Ferrari, A. C.; Beljonne, D.; Samorì, P. Light-enhanced

liquid-phase exfoliation and photoswitching current in graphene-azobenzene composites. *Nature communications* 2016, in press.

[8] Guidetti, G.; Cantelli, A.; Mazzaro, R.; Ortolani, L.; Morandi, V.; Montalti, M. Tracking graphene by fluorescence imaging: a tool for detecting multiple populations of graphene in solution. *Nanoscale* 2016, in press.